UNIVERSITY OF TRENTO

DOCTORAL THESIS

Chemogenetic modulation of fMRI connectivity

Federico Rocchi

Advisor: Alessandro Gozzi

A thesis submitted in fulfillment of the requirements

for the degree of Doctor of Philosophy in the:

Doctoral School in Cognitive and Brain Sciences, University of Trento

Center for Neuroscience and Cognitive Systems,

Istituto Italiano di Tecnologia

01 April 2022

Abstract and declaration

Declaration

This dissertation is the result of my own work unless specifically indicated in the text as the outcome of a collaboration, or cited and acknowledged as material from another source. It has not been previously submitted, in part or whole, to any university or institution for any degree, diploma, or other qualification.

Signed:_____

Date:_____

University of Trento, Doctoral School in Cognitive and Brain Sciences

Istituto Italiano di Tecnologia, Center for Neuroscience and Cognitive Systems

Doctor of Philosophy

Chemogenetic modulation of fMRI connectivity

Federico Rocchi

Abstract

Resting-state fMRI (rsfMRI) has been widely used to map intrinsic brain network organization of the human brain both in health and in pathological conditions. However, the neural underpinnings and dynamic rules governing brain-wide rsfMRI coupling remain unclear. Filling this knowledge gap is of crucial importance, given our current inability to decode and reverse-engineer clinical signatures of aberrant connectivity into interpretable neurophysiological events that can help understand or diagnose brain disorders.

Toward this goal, here we combined chemogenetics, rsfMRI, and *in vivo* electrophysiology in the mouse to investigate how regional manipulations of brain activity (i.e. neural inhibition, or excitation) causally contribute to whole-brain fMRI network organization. In a first set of proof of concept investigations, we empirically probed the widely held notion that neural inhibition of a cortical node would result in reduced fMRI coupling of the silenced area and its long-range terminals. Surprisingly, we found that chronic inhibition of the mouse medial prefrontal cortex (PFC) via viral overexpression of a potassium channel paradoxically increased fMRI connectivity between the inhibited area and its direct thalamo-cortical targets. Notably, acute chemogenetic inhibition of the PFC reproduced analogous patterns of fMRI overconnectivity. Using *in vivo* electrophysiology, we found that chemogenetic inhibition of the PFC enhances low frequency (0.1 - 4 Hz) oscillatory power via suppression of neural firing not phase-locked to slow rhythms, resulting in increased slow and δ band coherence between areas that exhibit fMRI overconnectivity. These results provide causal evidence that cortical inactivation can counterintuitively increase fMRI connectivity via enhanced, less-localized slow oscillatory processes, with important implications for neural modeling and interpretation of fMRI overconnectivity in brain disorders.

Importantly, our observation that neural inhibition of the PFC results in fMRI overconnectivity allowed us to predict that neural activation of the same area might produce opposite results, i.e. fMRI underconnectivity and neural desynchronization. To test this hypothesis, we used chemogenetics to increase local excitatory-inhibitory (E/I) balance in the PFC. As predicted, chemogenetic stimulation of CamkII-expressing neurons, or inhibition of fast-spiking parvalbumin-expressing neurons, produced similar rsfMRI signatures of rsfMRI underconnectivity. Both manipulations produced analogous electrophysiological signatures characterized by increased firing activity and a robust LFP power shift towards higher (i.e. γ) frequencies, effectively reversing the corresponding neural signature observed in DREADD inhibition studies. Importantly, the same E/I affecting perturbations were also associated with socio-communicative deficits in behaving mice hence underscoring the behavioral relevance of the employed manipulations. These results show that excitatory/inhibitory balance critically biases brain-wide fMRI coupling, pointing at a possible unifying mechanistic link between E/I imbalance and rsfMRI connectivity disruption in developmental disorders. More broadly, these investigations reveal a set of fundamental rules linking regional brain activity to macroscale functional connectivity, offering opportunities to physiologically interpret rsfMRI signatures of functional dysconnectivity in human brain disorders.

Acknowledgments

When I started the Ph.D., I had very high expectations. My dream was to become the best scientist around and solve all the big neuroscience questions. The reality was quite different. I ended up cleaning mouse litter, working in a dirty and old prefab, and, in the meanwhile, doing great science. What surprised me the most were the people. I didn't expect to meet so many amazing friends that completely changed my life.

First, I would like to thank Alessandro. You highlighted my flaws and taught me how to overcome them. You helped me become the man and the scientist I wanted to be. Your attitude and unique mix of eagerness, enthusiasm, and pragmatism make you the man we all love. I will always be proud to have been a member of your lab. Thank you for giving me the possibility to leave these four incredible years.

To the Functional Neuroimaging Lab: The first time I met Alessandro, he told me that his lab was, first of all, a team. "We sink or swim together" were the precise words, and he was right. It has been a privilege to work alongside such talented and fabulous people. Thanks to Alessia, Adam, Caterina, Chiara, Neha, Ilena, Elizabeth, Andrew, and Silvia.

Thanks to Leah, Rossella, and Paola for making all the paperwork a (mostly) smooth ride. A special thanks to Paola for all the times I (metaphorically) kidnapped his husband for late-night meetings or last-minute deadlines.

To my oversight committee, Paola and Stefano: thank you for your critical input. The whole experience has been a lesson in humility. I will never repeat the word "noise" in my entire life.

To Carola: you endured all my megalomania/Mc-Giver moments, blocking me every time I was going to make a silly choice. Thanks for your support, the fun, and all the crazy (and sometimes illegal) things we did. It was really fun!

To Alberto: you are my big brother in science. You taught me a lot, personally and scientifically. Who said that doing experiments cannot be funny?! Thanks for all the discussions, the help, and the singing. I will never forget our traditional celebrative breakfasts.

To David: It's a pity that sometimes you don't believe in yourself. You are one of the smarter people I have ever met. I hope that someday you will see yourself the way I do. Thanks for being there in the bad and good times. Your presence really made the difference.

To Staufi: we shared the highest and lowest moments of my Ph.D. Thanks for having made the failures sweeter and the success unforgettable. Without you, I would have enjoyed only half journey. You are amazing!

To Alexandria: You have the superpower to lighten people's lives with your enthusiasm and happiness. Thank you for using your superpower with me. It's worth every "can you spell it for me?!" in the world.

To Shahry: Your cynic and mathematical way to see life always kept me down-to-earth. Thanks for all the philosophical discussion and your love. You opened my mind as much you did with my heart.

To Lorenzo: We shared a lot: from the office to casa Irma. Every time you manage to make each experience unforgettable. Good spices make dishes tasty and unique. You are the good spice of my life.

To Dani: I always envy your energy and how you see life. Your presence makes me feel I can do everything. Thanks for being the yerba mate of my life (and, of course, for your music suggestions and beautiful proverbs).

To Ludo: You are my Ph.D. brother. I cannot imagine this experience without you. We push each other to explore new frontiers and get out of our comfort zones. Thanks for all the hours spent talking, the music, and the good memories. Like Bruce Willis in "Armageddon": I would sacrifice myself to save you.

To Giuggi: The chameleon of my life: colleague, animal guide, friend, noisy flatmate, and many more. Thanks for being you, a unique melting pot of good things.

Alessio and Baxi: you are my favorite weirdo from Trentino. Thanks for your company during this journey. You made this experience very funny.

To the "Due Lune": Thanks to you, I could meet my brothers-in-wind and write some of the most incredible chapters of the "Manuale". I hope you will survive Armageddon.

To my family: In the city center there is a proverb written on a wall: "Per quanto un albero possa diventare alto, le sue foglie, cadendo, ritorneranno sempre alle radici". Every time I read that, I think of you. There aren't enough words to explain how much I love you. You are the first, the last, my everything. Thanks for being you!

Luca: you are my oldest and closest friend. You are my polar star. Every time I lost my way, you helped me find it back. Thanks for these fantastic 15 years together.

Vale: Even if you live hundreds of kilometers away, you always manage to be present. Thanks for all the hours spent on discord talking and laughing. You really helped in blowing off some steam.

Squi: In electrophysiology, to acquire good signals, you need a ground to remove the noise, and a reference, to put everything under the proper perspective. You are the ground and reference of my life. There are not enough theses in the world to explain all the good things you did for me. Thanks for making me a better person. Before you, I was only the shadow of the man I'm now.

A hypothetical Indian: thanks for not accepting this job. Your absence made these four years the most incredible of my life.

Publications

- **Rocchi, F*.,** Canella, C.*, Noei, S.*, Gutierrez-Barragan, D., Coletta, L., Galbusera, A., ... & Gozzi, A. (2022). Paradoxical fMRI overconnectivity upon chemogenetic silencing of the prefrontal cortex. *Accepted for publication in Nature Communications*

  Contribution: Designed fMRI and electrophysiological experiments. Acquisition and analysis of fMRI data. Acquisition of electrophysiological experiments (LFP) and contribution to data analysis. Contributed to data conceptualization. Helped write the original draft.

- Gutierrez-Barragan*, D., Singh, N. A*., Alvino, F., Coletta, L., **Rocchi, F.,** De Guzman, E. A., ... & Gozzi, A. (2022). Unique spatiotemporal fMRI dynamics in the awake mouse brain. *Current Biology*

  Contribution: Design of anesthetized fMRI experiments, data acquisition and analysis. Helped in the collection and analysis of corticosterone measurements. Helped write the original draft

- Trakoshis, S.*, Martínez-Cañada, P.*, **Rocchi, F**., Canella, C., … & Gozzi, A., Lai, M., Panzeri, S., Lombardo, M.V. (2020). Intrinsic excitation-inhibition imbalance affects medial prefrontal cortex differently in autistic men versus women. *Elife*, 9, e55684

  Contribution: Design of fMRI experiments, data acquisition and analysis. Helped write the original draft.

*shared first authorship

Contents

List of Figures

Nomenclature and Acronyms

5HT3aR - ionotropic serotonin receptor 5HT3a

AAV – Adeno Associated Virus

ASD – Autism Spectrum Disorder

BOLD – Blood-Oxygen-Level-Dependent

CamkII – Calmodulin-dependent protein kinase II

Cg – Cingulate Cortex

CNO – Clozapine-N-Oxide

DMN – Default-Mode Network

DREADD – Designer Receptor Activated Exclusively by Designer Drug

E/I – Excitatory/Inhibitory

FC – Functional Connectivity

FDR – False-discovery Rate

fMRI – functional MRI

FS – fast-spiking

FWE – Family-wise error

GABA – Gamma-aminobuyiric acid

GAD-67 - Glutamate decarboxylase 67

GFP – Green Fluorescent Protein

HCP - Hippocampus

hM4Di – modified form of the human M4 muscarinic (hM4) receptor.

hM3Dq - modified form of the human M3 muscarinic (hM3) receptor.

hSyn – human Synapsin

IC – independent components

IN - interneurons

LCN – Latero-cortical Network

LFP – Local Field Potentials

mRNA - messenger ribonucleic acid

M1 – Primary Motor area

M2 – Secondary Motor area

MRI – Magnetic Resonance Imaging

MUA – Multi-Unit Activity

PC – Principal cells

PFC – Prefrontal cortex

PolyTh – Polymodal Thalamus

PV - parvalbumin

Rs – Retrosplenial cortex

rsfMRI – Resting State fMRI

RSN – Resting State Network

SEM – Standard Error of the Mean

S1 – Primary Somato-sensory cortex

S2 – Secondary Somato-sensory cortex

SST – Somatostatin

STR - Striatum

Th – Thalamus

UniTh – Unimodal Thalamus

V1 – Visual cortex

VPM – Ventral posteromedial nucleus

Chapter 1: Introduction

1.1 Mapping the functional organization of the brain with resting-state fMRI

Neuroimaging techniques, such as functional magnetic resonance imaging (fMRI), are becoming increasingly popular for investigating functional synchronization in the resting human brain (e.g. in the absence of an active task or stimulus). The computation of statistical correlations between spontaneous fluctuations in Blood Oxygenated Level Dependent (BOLD) signal across brain regions is often used as a measure of inter-regional communication or "Functional Connectivity" (FC, Figure 1.1)(Biswal et al., 1995; Fox & Raichle, 2007; Friston, 2011; Van Den Heuvel et al., 2010). A large body of experimental work has demonstrated that spontaneous low-frequency fluctuations in fMRI signals are temporally synchronous across multiple functional systewhilems, delineating a set of reproducible topographies known as resting-state networks (RSNs), which can be reliably identified in humans (Van Den Heuvel et al., 2010) as well in several animal species including primates (Milham et al., 2020) and rodents (Gozzi & Schwarz, 2016; Hutchison et al., 2010; Lu et al., 2012; Schwarz et al., 2012, 2013).

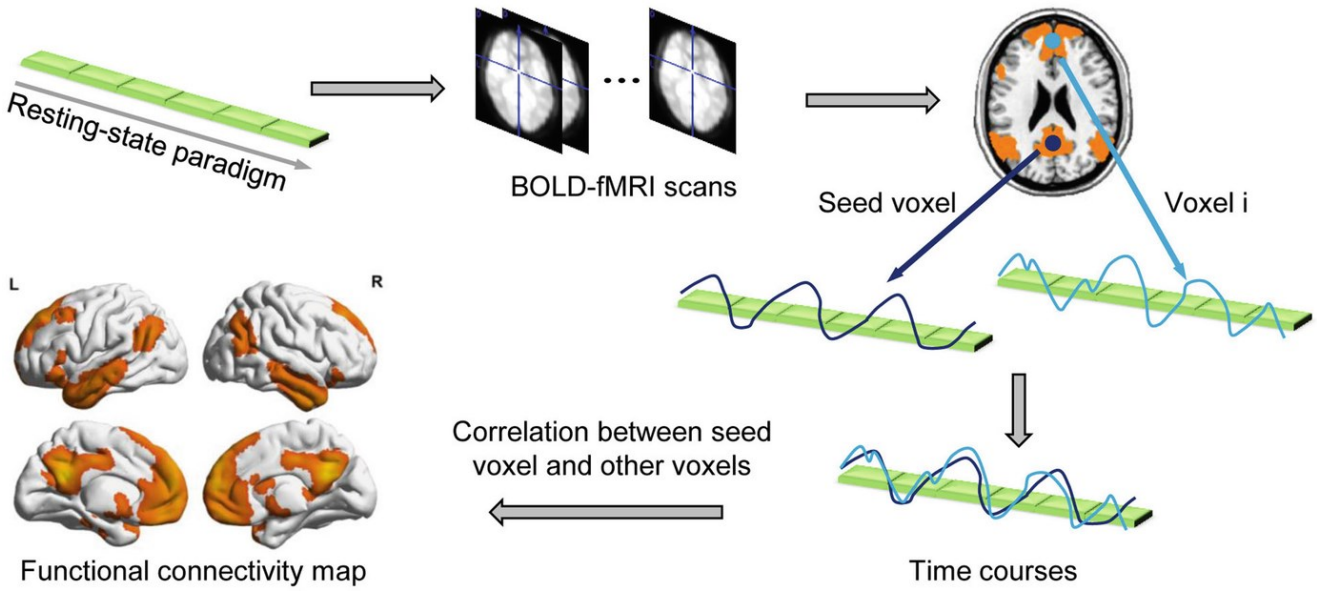

Figure 1.1 Resting-state fMRI (rsfMRI) measures functional connectivity (FC) by correlating spontaneous fluctuations in BOLD activity. *FC is typically quantified with respect to a seed region (i.e. PCC – posterior cingulate cortex). Temporal correlation between spontaneous fMRI BOLD fluctuations in the seed voxel is mapped with voxel-resolution to define areas that are functionally connected (i.e. exhibit synchronous fluctuations) to the probed areas. The highlighted areas define so-called resting-state functional connectivity networks (RSN) (from Hu & Zeng, 2019).*

Well-characterized human RSNs include anatomically and functionally related regions involved in sensory and cognitive function (visual, somatomotor, auditory, frontoparietal, attentional, and limbic, among others, (Yeo et al., 2011)) as well as more widely distributed associative areas, such as an insular-prefrontal "salience network", and a set of corticolimbic areas termed "Default Mode Network" (DMN), owing to their high synchronization at rest. This latter network is of particular interest, given that its highly debated and still mysterious cognitive and processing functions, its disproportionately high metabolic requirement in resting conditions (Buckner et al., 2008), and its strong vulnerability to disruption in multiple brain disorders (Buckner et al., 2008; Gusnard & Raichle, 2001; Raichle, 2015; Raichle et al., 2001; Uddin et al., 2009; Yeo et al., 2011; Zhao et al., 2013).

1.2 Evolutionarily-relevant rsfMRI networks in the rodent brain

Previous studies in awake and anesthetized primates (Rilling et al., 2007; Vincent et al., 2007) as well as rodents (Gutierrez-Barragan et al., 2022; Hutchison et al., 2010; Lu et al., 2012; Schwarz et al., 2012, 2013) have revealed the presence of multiple cortical and subcortical RSNs broadly recapitulating functional network systems observed in the human brain (Fig 1.2). These include motor and sensory cortical networks (Grandjean et al., 2020; Sforazzini et al., 2014; Liang Wang et al., 2012) dorsal and posterior hippocampal systems, a thalamo cortical network (Liang et al., 2015), and multiple basal forebrain arousal-related RSNs (Gutierrez-Barragan et al., 2022). Notwithstanding some expected differences in the organization of higher-order cortical RSN across species (Corbetta & Shulman, 2002), these observations are of great importance, as they suggest that brain-wide RSN organization is to a large extent evolutionarily conserved in mammalians species. Importantly, these correspondences also offer the opportunity to leverage advanced perturbational and recording approaches in physiologically accessible species for the investigation of the neural underpinning of rsfMRI connectivity (Gozzi & Schwarz, 2016). As part of this line of investigation, the implementation of rsfMRI in the laboratory mouse is of special interest, owing to the large availability of transgenic models and neural manipulations currently available to experimental neuroscientists.

Recent advances in preclinical functional neuroimaging have paved the way for the implementation of robust rsfMRI connectivity mapping in the mouse. Pioneering work from Sforazzini and colleagues (Sforazzini et al., 2014) revealed the presence of robust, homotopic rsfMRI connectivity networks in this species, including distributed network systems previously identified in primates and humans. These include a mouse precursor of the human DMN, and a salience network. The observation of these RSNs in a lower mammalian species is consistent with the large involvement

of evolutionarily ancient limbic cortices in these networks (Gozzi & Schwarz, 2016; Whitesell et al., 2021). Subsequent high-resolution voxel-scale network analysis of rsfMRI connectivity corroborated these findings, revealing the presence of six distinct functional modules related to known large-scale functional partitions observed in the human brain (Liska et al., 2015). These initial investigations have been independently confirmed and expanded by subsequent studies from an increasing number of labs in the world (Grandjean et al., 2017, 2020; Lee et al., 2021) which together have established a novel field of translational research aimed to study the foundational principles of large-scale network organization and its disruption in brain disorders.

Importantly, initial rsfMRI mapping in primates and rodents has been promptly followed by a stream of subsequent studies aimed to relate the spatial structure of RSN to underlying neuronal anatomy as part of the nascent field of brain connectomics (Bargmann & Marder, 2013). Specifically, the use of high-resolution connectomes based on tracer injections in animals has allowed to relate rsfMRI network architecture with quantitative and directional measures of connectivity at the mesoscale (Knox et al., 2018; Oh et al., 2014), hence transcending the limitations of coarse-scale human anatomical connectome mapping via diffusion-based MRI. These investigations, recently reviewed by Suárez et al. (2020), have revealed conserved rules of cortical connectivity across species (Goulas et al., 2019), including cell-class-specific projection patterns (Harris & Shepherd, 2015) but more importantly have shown that the topographic organization of rsfMRI networks is critically shaped and constrained by the underlying connectome structure (Coletta et al., 2020; Grandjean et al., 2017; Stafford et al., 2014). These investigations have been recently extended to the investigations of the layer and cell-type-specific organization of specific rsfMRI networks (i.e. the DMN, (Whitesell et al., 2021)). Collectively, this research has revealed a tight relationship between the structural and functional organization of brain activity at the macroscale, providing robust empirical support to so-called “structurally based” models of rsfMRI connectivity (Alstott et al., 2009; Suárez et al., 2020), according to which rsfMRI network organization and the ensuing functional connectivity are a direct expression of the anatomical organization of axonal connectome (Deco et al., 2013, 2017). This prevalent notion is of relevance to this thesis, as some of the assumptions of these widely-held models are challenged by some of the results we report and extensively discuss in chapter 4.

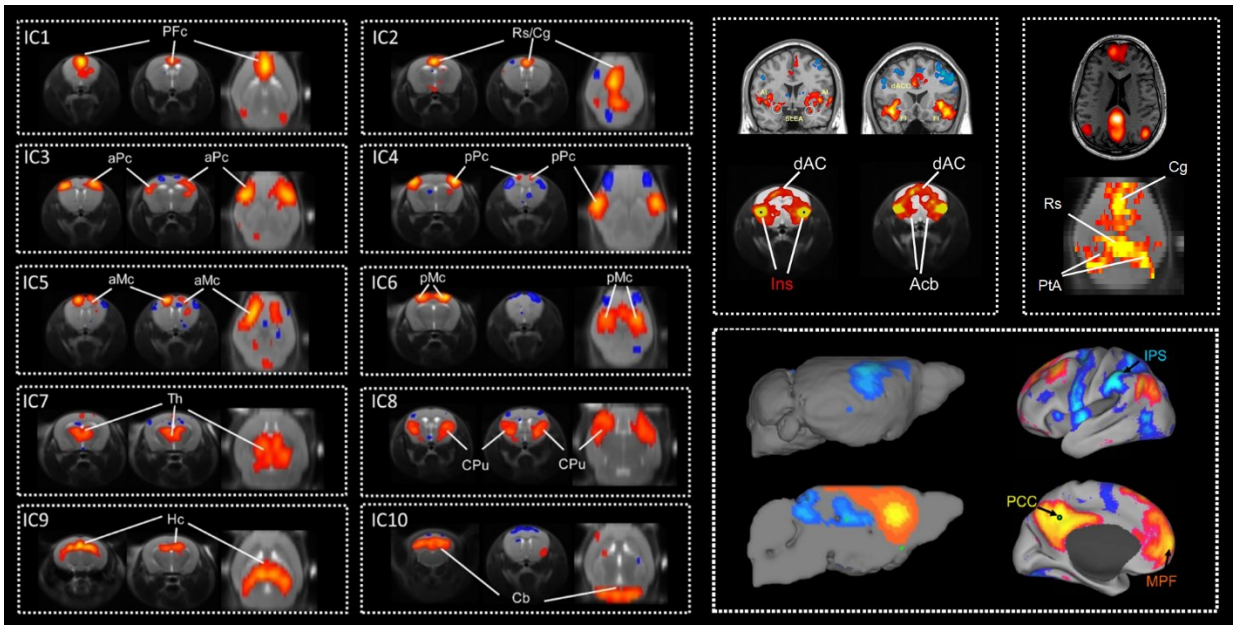

Figure 1.2 The mouse brain contains evolutionarily-relevant rsfMRI networks. *These networks encompass motor-sensory systems, sub-cortical components (Left, IC: independent components, form Sforazzini et al., 2014), as well evolutionarily relevant precursors of the human salience and DMN (from Liska & Gozzi, 2016; Sforazzini et al., 2014)*

1.3 rsfMRI connectivity is disrupted in psychiatric and developmental disorders

The optimization of rsfMRI mapping in rodents and other physiologically accessible species has been welcomed with great excitement by clinical and systems neuroscientists interested in the investigation of rsfMRI connectivity disruption in human brain disorders. Since its inception, rsfMRI has been indeed widely employed to study large-scale brain organization in the diseased brain, with the aim to understand how complex etiopathology could affect interareal communication, and large-scale network organization. Clinical rsfMRI investigations have produced robust and undisputed evidence that rsfMRI connectivity is almost invariably disrupted in all major brain disorders. For example, reduced rsfMRI connectivity in associative cortical regions has been largely documented in schizophrenia (Clinton & Meador-Woodruff, 2004; Friston & Frith, 1995; Garrity et al., 2007; Huang et al., 2010; Lynall et al., 2010). Patients with depression, by contrast, exhibit atypically stronger rsfMRI coupling in the frontal and parietal components of the DMN, as well as in the cortico-midline system (Lin Wang et al., 2012). An opposing rsfMRI signature, consisting of reduced connectivity in prefrontal regions, has been consistently documented in bipolar disorder (Leichsenring et al., 2011; Lis et al., 2007) (Fig. 1.4).

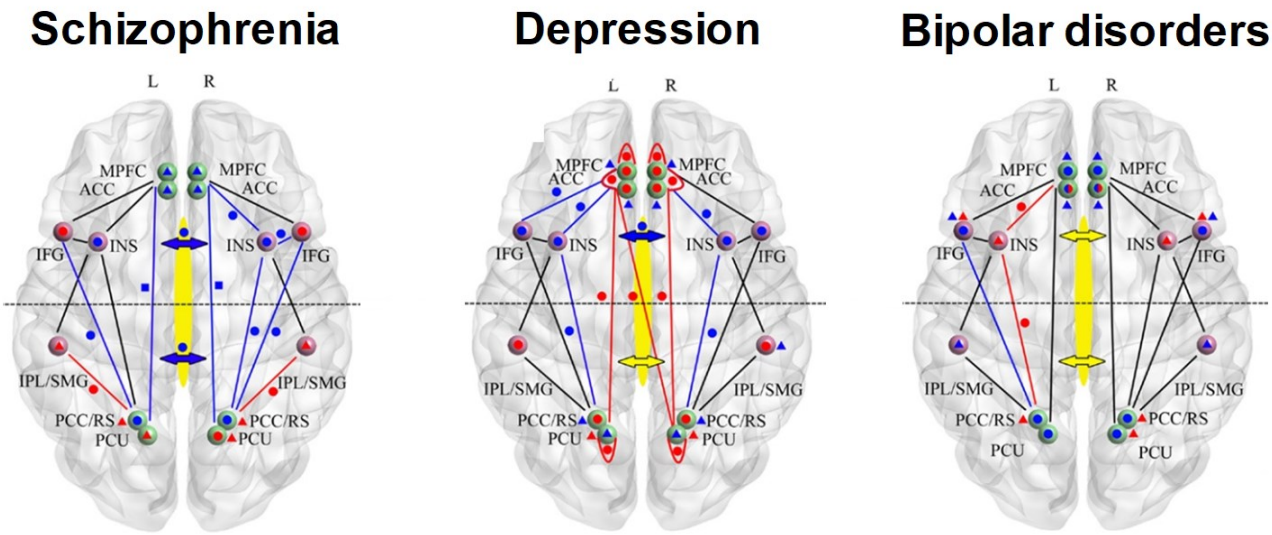

Figure 1.3 Signatures of altered or atypical functional connectivity in brain disorders. *The figure shows how different pathologies can result in different patterns of functional dysconnectivity (adapted from Zhao et al., 2013).*

rsfMRI mapping has also been widely utilized to study "functional connectopathy" in autism spectrum disorders (ASD) and related developmental conditions. The results obtained by these investigations are described in more detail here, as they epitomize both the power and the limitations of the clinical use of rsfMRI to map brain pathology, and the usefulness of complementary approaches in animals to address clinically relevant questions. Initial applications of rsfMRI to clinical ASD were strongly biased by the expectation that this method, in conjunction with other brain mapping techniques, could help objectivize diagnosis of these disorders by revealing an unequivocal signature of network dysfunction specific for autism. A number of imaging studies in both idiopathic (Di Martino et al., 2014) and syndromic autism (Hall et al., 2013; Scott-Van Zeeland et al., 2010) have produced encouraging converging evidence of disrupted rsfMRI connectivity. These initial observations have strongly influenced the field, promoting the so-called "disrupted connectivity theory of ASD" (Geschwind, 2009; Vasa et al., 2016), whereby symptoms of ASD may arise from dysfunctional interregional brain communication inferable from rsfMRI connectivity mapping. In its original declination, this theory posits that individuals with ASD would be characterized by weak connections (under-connectivity) between distant brain regions and increased connections within local regions (over-connectivity) (Belmonte et al., 2004), resulting in altered sensory and cognitive processing. However, a wave of subsequent studies have quelled this initial enthusiasm, revealing great heterogeneity in the clinical manifestation of ASD functional connectopathy, with evidence of

reduced, increased, or mosaic patterns of functional dysconnectivity across clinical cohorts (Di Martino et al., 2014; Holiga et al., 2019; J. V. Hull et al., 2017; Supekar et al., 2013; Vasa et al., 2016). These inconsistent observations have stirred controversy and debate in the field, putting into question the etiological significance of these findings, and questioning the robustness and reproducibility of rsfMRI to investigate the diseased brain (Bossier et al., 2020; King et al., 2019). This ongoing discussion highlights our inability to properly frame and interpret the origin and significance of functional connectopathy in human disorders and highlights the need to complement clinical research with mechanistic investigations in physiologically accessible species. Filling this knowledge gap is of paramount importance, given our current inability to decode and reverse-engineer clinical signatures of aberrant connectivity into interpretable neurophysiological events that can help understand or diagnose brain disorders.

1.4 rsfMRI connectivity is disrupted in mouse models of developmental disorders

While the origin and significance of ASD-related connectional aberrations remain largely unknown, the heterogeneous "connectional landscape" observed in the clinical studies is in fact not surprising in the light of the mounting evidence that the ASD spectrum reflects multiple and diverse genetic and etiological contributions (Satterstrom et al., 2020). Importantly, this observation suggests that the heterogeneous expression of connectivity in ASD might, in reality, be a bona fide reflection of etiological variability in ASD, rather than the byproduct of experimental and technical inconsistencies related to rsfMRI data analysis. Within this framework, connectivity heterogeneity across clinical cohorts would thus be an expected outcome, possibly inducive of patient stratification based on cross-etiological network dysfunction patterns. However, the alternative hypothesis that ASD connectional heterogeneity is more prosaically the expression of rsfMRI related noise remains, and current clinical research does not at present allow to rigorously disambiguate these two opposing views.

rsfMRI measurements in transgenic rodent lines, where advanced genetic techniques allow for precise control of environmental and genetic variability (Liska & Gozzi, 2016), have recently allowed us to rigorously address this question (Zerbi et al., 2021). Specifically, recent collaborative work between our lab and the University of Zurich has sought to address the long-standing question of whether heterogenous functional connectivity in ASD would be expected to converge onto a single signature of network dysfunction of diagnostic value for ASD, or whether it could be instead conceptualized as the sum of different functional dysconnectivity modes. To rigorously address this

question, we used mouse rsfMRI to carry out a cross-etiological investigation of fMRI-based functional connectivity across 16 distinct mouse ASD models (Zerbi et al., 2021). This strategy has the advantage of allowing rigorous control of genetic and environmental variation and minimization of motion artifacts via the use of light sedation, thereby circumventing two of the most notorious confounding factors in clinical research. Moreover, these investigations benefitted by the presence of a clearly-defined reference group (i.e. wild-type littermates), enabling to produce relative estimates of rsfMRI connectivity as in analogous human case-control studies (Di Martino et al., 2014). Interestingly, this investigation revealed that various ASD-related etiologies produce a wide range of connectional anomalies, including opposing (i.e. over- vs. under-connectivity) signatures of network dysfunction. We note here that the use of the terms over- or under-connectivity refer to between group differences, and, as extensively described and discussed in chapter 3, do not necessarily imply increased (or decreased) *direct* communication between regions. Nonetheless, this finding argues against the existence of a biologically meaningful, specific signature of rsfMRI dysfunction in ASD. Importantly, these diverse and often diverging connectional fingerprints could nonetheless be clustered into four homogeneous connectivity sub-types, each with specific signs of network dysfunction and reported as follow:

1. "Under-connectivity" in anterior cingulate, caudoputamen, hippocampus, colliculus, insula, somato-motor cortices, and increased connectivity between areas in amygdala, ventral posterolateral thalamus, pontine nuclei, prefrontal, orbitofrontal, and piriform and visual cortices.
2. "Under-connectivity" between cortico-striatal areas and inferior colliculus but increased connectivity between hippocampus, ventral orbital, and lateral septal nuclei cortex.
3. "Under-connectivity" of thalamic VPM, anterior cingulate, insula, hippocampus and only a moderate over-connectivity in the accumbens shell and hypothalamus.
4. "Over-connectivity" in hypothalamus and hippocampus and under-connectivity between piriform and olfactory-related areas, striatum and polymodal thalamus.

Across these clusters, independently from the directionality of the atypical connectivity (i.e., over- or under-connectivity), somatomotor, olfactory, and cortical areas showed a higher level of vulnerability (Fig 1.5, Zerbi et al., 2021). These results are important, as they suggest that etiological variability is a key predictor of connection heterogeneity in ASD, thus explaining inconsistent results in clinical populations. Moreover, they also promote a profound reconceptualization of heterogenous

rsfMRI dysconnectivity in autism: rather than challenge the heterogeneous nature of clinical findings. Clinical efforts should be aimed at embracing this variability and parsing it into cross-etiological "connectivity neuro-subtypes" of putative pathophysiological relevance.

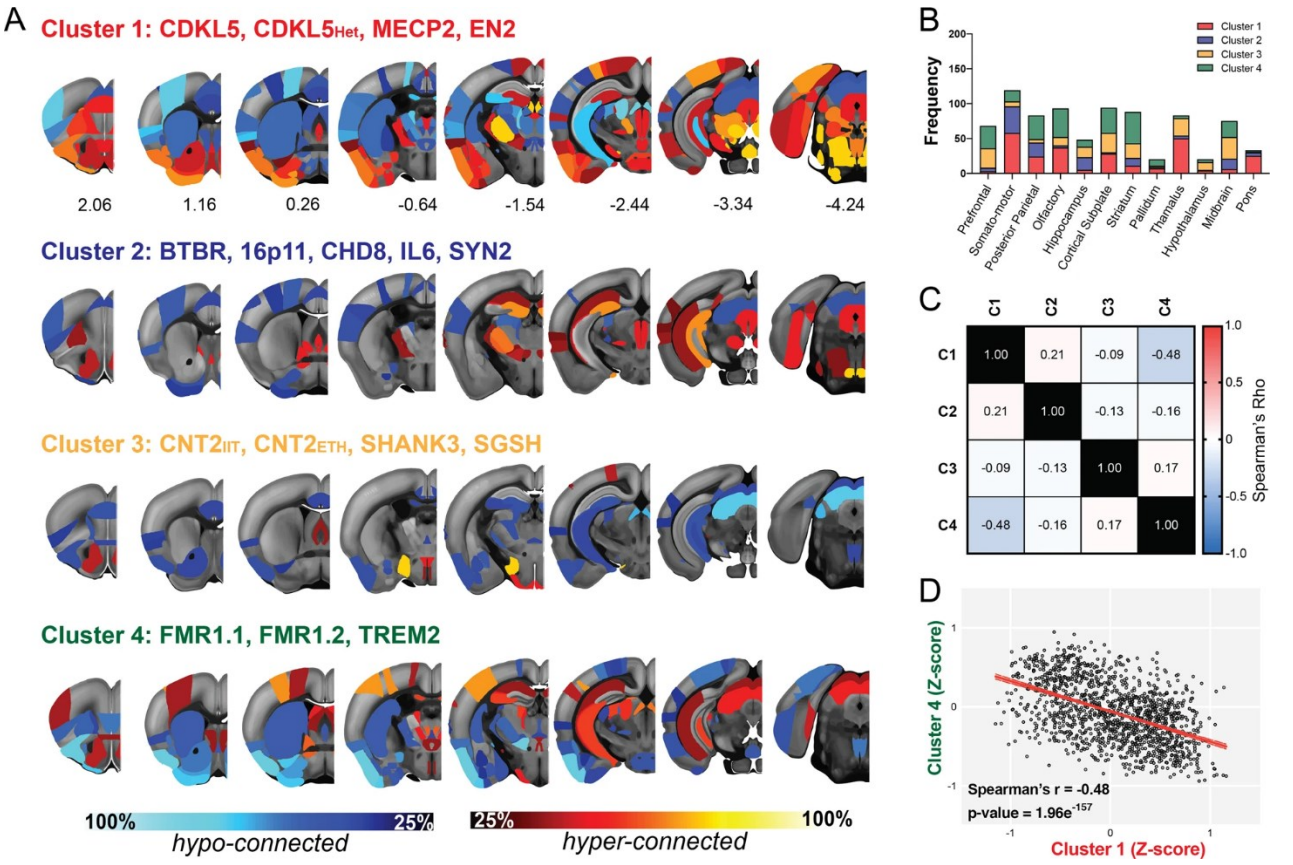

Figure 1.4 Functional connectivity signatures across 16 models of autism can be clustered into different groups, potentially revealing etiologically relevant connectivity subtypes (Zerbi et al., 2021).

These findings have been described in great detail as they set the stage for the research described in this thesis along two main directions. First, they demonstrate that the translational nature of rsfMRI enables this approach to address research questions of high clinical relevance. Second, the identification of cross-etiological signatures of rsfMRI dysconnectivity reveals the critical need to elucidate the physiological underpinnings of network dysfunction with the ultimate goal of decode and reverse engineering altered or aberrant rsfMRI coupling into interpretable (and mechanistically relevant) cascades of physiological events. This admittedly highly ambitious goal can only be attained via a systematic dissection of the neural drivers of rsfMRI connectivity via targeted neural manipulations in model organisms. In the next chapter, I will expand on this strategy and will discuss more in detail some of the experimental approaches employed in this thesis to achieve this goal.

1.5 Towards physiological decoding of fMRI dysconnectivity

1.5.1 Neural constituents of cortical circuits

A major goal of my thesis was to probe the neural drivers of functional coupling in cortical areas as assessed with rsfMRI using cell-type-specific neuromanipulations in the mouse. The information gathered in these investigations may thus help characterize and possibly decode corresponding dysconnectivity signatures into physiologically interpretable signals. In this chapter I will briefly review some key cell populations that I manipulated in this thesis and their contribution to cortical network function.

Cortical networks comprise glutamatergic excitatory neurons and local inhibitory GABAergic interneurons that modulate signal flow and shape mesoscale network dynamics (Gonzalez-Burgos et al., 2015). Propagation of activity in excitatory networks is predictable and straightforward: excitation generates further excitation, independent of time, wiring complexity, and strength of excitation. Excitatory glutamatergic neurons, also known as principal cells (PCs), are defined by their capacity to activate through excitatory neurotransmitters other neurons and encode information through action potential intensity and frequency. Although less abundant than their excitatory counterparts, GABAergic inhibitory interneurons (IN) are critically involved in controlling excitation and the emergence of brain rhythms. One defining feature of this class of neurons is their high heterogeneity, which forms the basis of distinct functional categories based on morphological, electrophysiological, and molecular features. This heterogeneity has been exploited to provide a functional and molecular classification of IN in the neocortex. Among the best characterized and most studied classes of INs are cells that express the calcium-binding protein parvalbumin (PV) and those expressing the neuropeptide somatostatin (Sst) (Tremblay et al., 2016). These two markers, together with the expressions of ionotropic serotonin receptor 5HT3a (5HT3aR), appear to be present in non-overlapping IN populations in the neocortex (Tasic et al., 2016; Zeisel et al., 2015), and together, account for nearly 100% of neurons expressing GAD-67 mRNA, a neural marker specific for GABAergic neurons (Rudy et al., 2011).

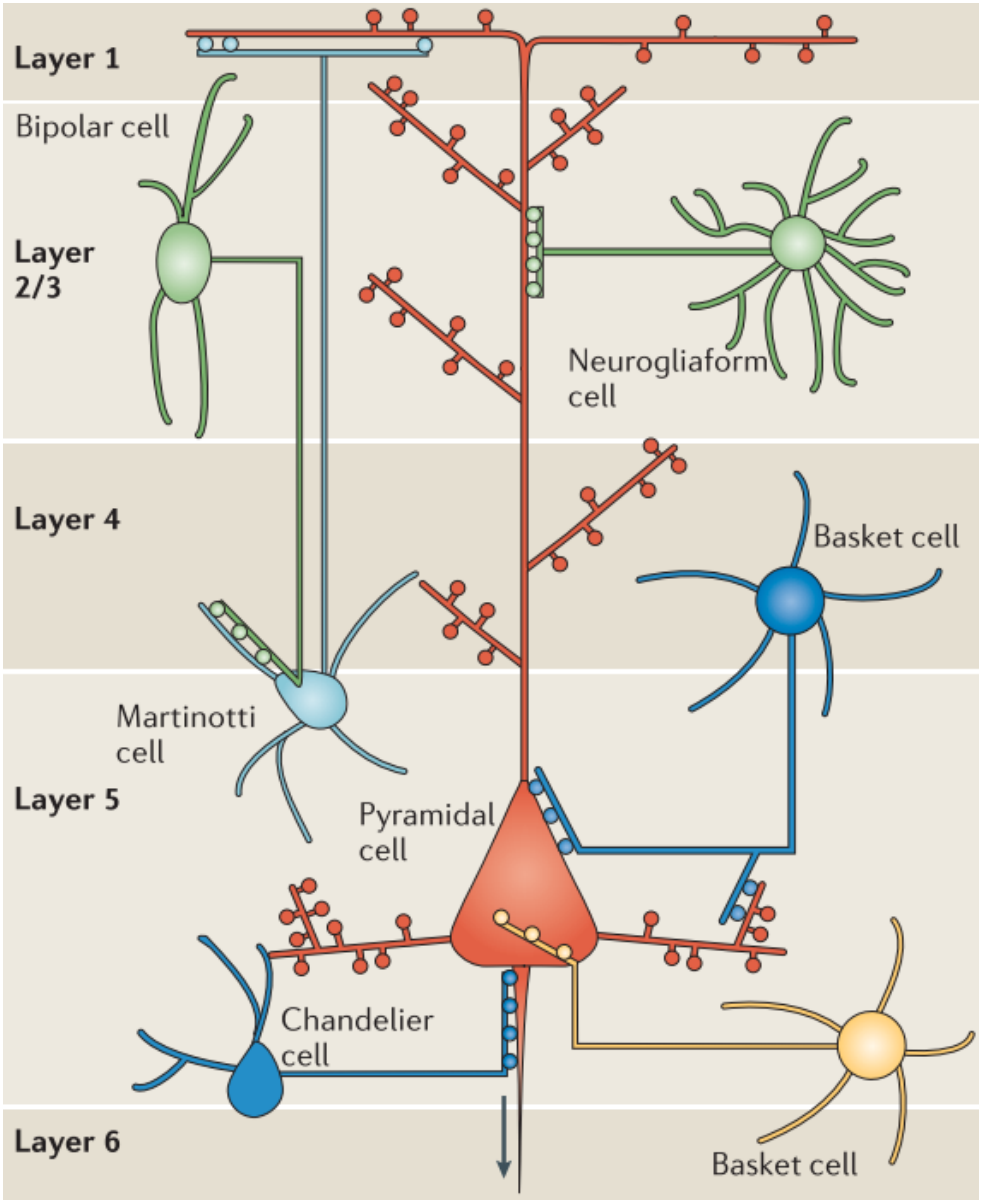

Figure 1.5 Different classes of cortical interneurons are distinguished on the basis of their morphology and pattern of connectivity. Adapted from Marín (2012)

PV positive neurons have attracted a lot of interest in the preclinical and clinical community, given the emerging evidence linking their dysfunction to psychiatric disorders (Marín, 2012; Morris et al., 2008; Urban-Ciecko & Barth, 2016) and the possibility of manipulating them via genetically engineered mouse lines. PV positive neurons include two morphological types: fast-spiking (FS) basket cells and chandelier cells. Chandelier INs, also known as axo-axonic neurons, are the most recognizable INs in terms of morphology (DeFelipe et al., 2013) due to the unique candlestick-like synaptic terminal arrays they form to specifically target the initial axon segment of PCs. In contrast, basket cells make peri-somatic "basket" terminals on the soma and proximal dendrites of PCs and

INs. PV FS basket cells are the largest population of INs in the neocortex. By producing hyperpolarizing and/or shunting inhibition close to the site of action potential generation, both types of INs powerfully influence the output of their target cells (Rudy et al., 2011). Specifically, the speed and precision of the PV-mediated cell signaling allow this type of cells to function as coincidence detectors and to impose this function onto their postsynaptic targets. These features, in turn, make PC-cells a class of INs pivotally involved in the emergence and control of meso- ad macroscale neural network synchronization and dynamics, with a prominent involvement in the generation of fast rhythms (Cardin et al., 2009; Sohal et al., 2009; Tremblay et al., 2016; Xue et al., 2014).

Networks built from excitatory and PV inhibitory neurons can self-organize and generate complex properties. One of the most interesting is the generation of electrophysiological oscillations and mesoscale network dynamics (Buzsáki, 2006). Different morphological and biophysical properties of INs can convey different rhythmicity. For example, when inhibition is mediated by fast-acting $GABA_A$ receptors like the ones present in the PV cells, the corresponding oscillation frequency will correspond to the gamma frequency band (40–100 hertz) of the local field potential (Buzsáki, 2006; Buzsáki et al., 2004; Fries, 2005). Changing the time constant of the $GABA_A$-receptor the mediated GABA response will affect the frequency of the interneuron network oscillators (Buzsáki, 2006; Buzsáki et al., 2004; Fries, 2005). These properties are of great interest in the light of the emerging view that large-scale interregional neuronal communication could be mechanistically subserved by neuronal coherence in brain rhythms (Fries, 2005). According to this view, neuronal oscillations and rhythmic excitability fluctuations produce a temporal window for communication. In the case of bi-directional communication, only coherently oscillating neuronal clusters can interact effectively. Importantly, in case of the absence of synchronicity or phase-shifting in large-scale rhythms, the communication between different brain areas would be strongly impaired, possibly affecting macroscale functional coupling and network communication (Buzsáki, 2006; Fries, 2005). Taken together, these features suggest that a proper tuning of local and long-range excitatory and Inhibitory (E/I) balance are critical for the establishment and maintenance of long-range functional coupling. In this respect, regional deviations in overall neural output, or local E/I imbalances are expected to prominently affect brain communication and functional connectivity as assessed with rsfMRI and other functional mapping methods. Accumulating evidence of the coexistence of E/I imbalance and functional dysconnectivity in several brain disorders (briefly reviewed in the following chapter) lend indirect support to this hypothesis.

1.5.2 Excitatory and inhibitory balance and functional dysconnectivity in autism

One long-standing conceptual framework used to explain pathological changes in the autistic brain and related developmental disorders is that genetically distinct forms of autism share a common increase in synaptic E/I ratio, leading to hyperexcitability, excess spiking, and increased "noise" in cortical circuits (Rubenstein & Merzenich, 2003). Supporting this hypothesis, a large body of evidence points to a deficient GABAergic activity in patients with ASD, as well as mouse lines modeling the disorders (Chao et al., 2010; Gibson et al., 2008). Moreover, substantial comorbidity between ASD and epilepsy exist, with as many as 30% of autistic patients presenting clinical signs of seizures (Canitano, 2007; Gillberg & Billstedt, 2000). Other observations are broadly consistent with this framework, including the involvement of many autism-related mutations in the dysregulation of excitatory synapses (Davenport et al., 2019; Pathania et al., 2014), and post-mortem studies reporting a reduced number of GABAergic interneurons in people with autism (Zikopoulos & Barbas, 2013).

It should, however, be pointed out that, despite the popularity and plausibility of the E/I imbalance theory of autism, physiology studies using transgenic mouse models of ASD provided only mixed support for this hypothesis. The number of investigations of synaptic function in genetic mouse models of ASD reported reduced inhibitory activity in the mouse hippocampus and neocortex (Chao et al., 2010; Gibson et al., 2008). However, other investigations have challenged this view, reporting a greater decrease in excitation than inhibition (Dani et al., 2005) or increased inhibition altogether (Harrington et al., 2016). It is possible that the observed discrepancies might be due to variability across studies like area of interest, cell type, ASD genotype, and physiological methods of analysis, which complicate the identification of common synaptic and local circuit defects (Chao et al., 2010; Dani et al., 2005; Delattre et al., 2013). A recent attempt to clarify this heterogeneity comes from a study conducted on four different autism animal models by Antoine et al. (2019). This research showed reduced inhibition coupled with a more modest reduction in excitation, driving an increase in the E/I conductance ratio (Antoine et al., 2019). However, in these models, circuit-level neocortical activity was not affected, opening up the intriguing possibility that E/I ratio imbalance could be a homeostatic response (i.e., an adaptive compensation) to stabilize neuronal activity, which would in turn call into question the causal contribution of E/I imbalance to ASD (Antoine et al., 2019).

Notwithstanding the current controversy on the etiological role of this phenomenon and its generalizability to ASD, clinical evidence of a possible overall brain hyper-excitability in ASD remains

prominent (as denoted by high ASD and epilepsy comorbidity). Importantly, with the vast majority of research on the pathological relevance of E/I focusing on microcircuit organization. However, one key aspect that appears to have been largely neglected is whether and how E/I imbalance may be associated with disease-relevant traits affecting macroscale network communication and dynamics, a set of functions that are critical for proper brain functioning (Brock et al., 2007; Rubenstein & Merzenich, 2003). This notion would be consistent with the evidence of atypical or disrupted rsfMRI connectivity in ASD (Vasa et al., 2016), as neurobiological deficits in the function of both excitatory and inhibitory neuronal populations could lead to local E/I imbalance and consequently impaired functional coupling in ASD.

As discussed above, a large body of evidence points to a deficient inhibitory activity in patients with ASD and in mouse lines modeling the disorders (Chao et al., 2010; Gibson et al., 2008). Because of the established role of inhibitory function in determining brain rhythms and functional coupling (Yizhar et al., 2011), a novel, unifying conceptual framework whereby local alterations in E/I balance would lead to disrupted macroscale functional coupling is thereby conceivable. Such an interpretative construct would mechanistically link the E/I imbalance and disrupted connectivity of ASD into a single broad conceptual umbrella, suggesting that regional E/I alterations could cause functional connectivity disruption observed in ASD.

Importantly, the biological plausibility of this hypothesis can be rigorously and simply tested in proof-of-concept studies entailing the combination of cell-type-specific manipulations of neural excitability with brain-wide functional connectivity mapping in animals. Specifically, chemogenetic tools have recently been developed for long-term neuronal manipulations that appear to be ideally designed to mimic disease-induced altered connectivity (Farrell & Roth, 2013). This method entails the expression of a genetically modified receptor on targeted neurons, which can be remotely activated by an exogenous, biologically inert ligand (Farrell & Roth, 2013; Sternson & Roth, 2014). The combination of chemogenetics and rsfMRI (chemo-fMRI, (Giorgi et al., 2017)) is, therefore, a powerful investigational tool that can be employed to deconstruct rsfMRI connectivity and understand how regional brain activity (and local E/I balance) can affect brain-wide coupling, with implications for the modeling and interpretation of dysconnectivity in brain disorders. This approach and its potential as a perturbational tool in neuroimaging research are discussed more in detail in the following chapter, as they represent the technical foundations of this thesis.

1.6 Deconstructing rsfMRI connectivity with chemo-fMRI

Chemogenetics techniques rely on the expression of engineered receptors into a specific cell population to modulate their activity by systemically administering an exogenous designer ligand that is biologically inert, or devoid of prominent direct pharmacological effects (Farrell & Roth, 2013; Sternson & Roth, 2014). This neural platform entails the expression of engineered G-protein coupled receptors to regionally modulate neural activity with cell-type specificity (Sternson & Roth, 2014; Zhu & Roth, 2015). The combined use of chemogenetics and fMRI represents a novel experimental strategy for bridging different levels of investigation in experimental neuroscience. Giorgi and colleagues reported the first demonstration of this approach in 2017, coining the term "chemo-fMRI" to refer to the combined use of fMRI and chemogenetics. The authors of this study used chemo-fMRI to causally probe the brain-wide substrates modulated by endogenous serotonergic activity (Giorgi et al., 2017). A subsequent influential chemo-fMRI study probed the effect of chemogenetic inactivation of the amygdala on rsfMRI patterns of connectivity in rhesus monkeys (Grayson et al., 2016). The authors found that, as predicted by the structurally-based model of connectivity, this manipulation reduced amygdala-cortical and cortico-cortical coupling. These studies demonstrate the power of combining a focal DREADD manipulation with rsfMRI to detect changes in local and global network organization in vivo. Similar findings have been reported in two recent rodent chemo-fMRI studies (Peeters et al., 2020; Tu et al., 2020).

In our study, we have expanded these investigations by probing how regional neural silencing and increased E/I affect brain-wide functional connectivity within the mouse DMN. For the specific purpose of these studies, we employed “designer receptors exclusively activated by designer drugs (DREADDs) (Roth, 2016). These are engineered acetylcholine G-coupled receptors maximally responsive to clozapine-N-oxide (CNO), a metabolite of the antipsychotic drug clozapine (Manvich et al., 2018; Roth, 2016). Depending on the interacting G-protein, two main classes of DREADDs have been developed: Gi-coupled (hM4Di) and Gq-coupled (hM3Dq) DREADDs. Gi-DREADDs promote Gi-protein-dependent intracellular signaling, leading to neuronal inhibition via activation of inward rectifying K channels, thereby hyperpolarizing, hence inhibiting neuronal activity (Roth, 2016), and silencing synaptic transmission (Fig. 1.6) (Stachniak et al., 2014). When expressed pan-neuronally in both excitatory and inhibitory populations, hM4Di DREADDs can be used to produce neural silencing (Wiegert et al., 2017). Notably, the use of this approach in combination with rsfMRI thus offers the opportunity to deconstruct rsfMRI coupling by inactivating a neural node and assessing how neural

activity reconfigures in response to this manipulation. We have used this strategy extensively in a series of studies we describe in greater detail in chapter 3.

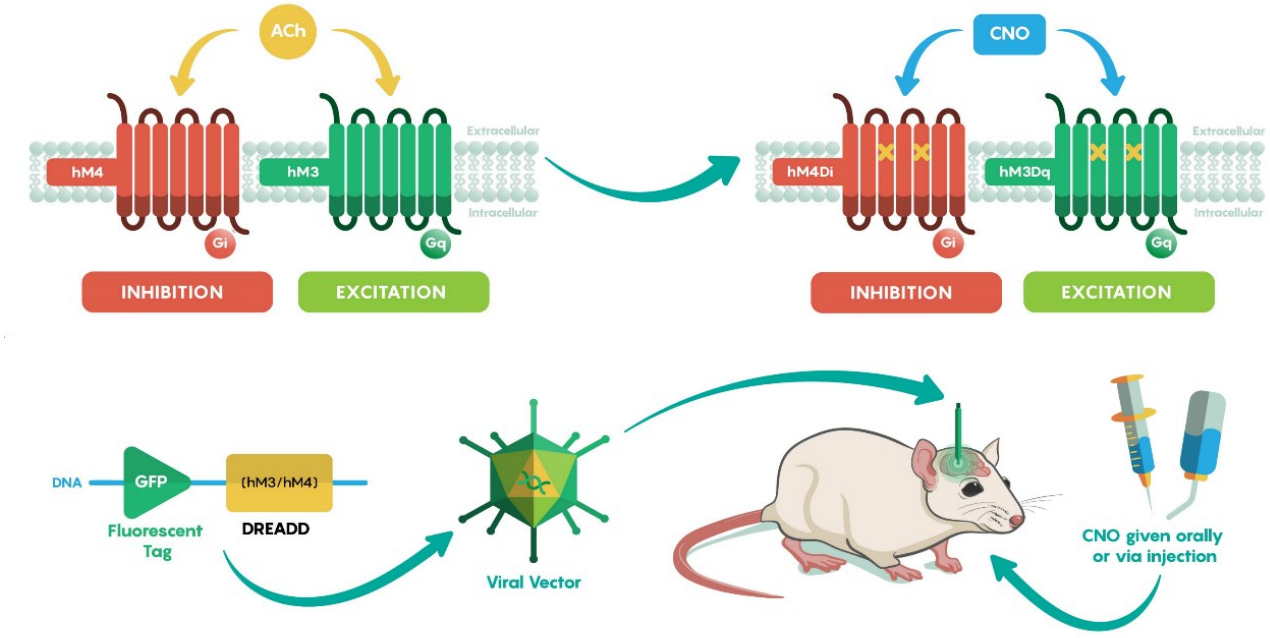

Figure 1.6 Muscarinic acetylcholine receptors have been engineered to produce different DREADDs. *Through viral vectors, DREADDs can be expressed in specific neuronal populations. The peripheral administration of an inert ligand leads to receptor activation, triggering an intracellular signaling cascade that can enhance or inhibit neuronal activity. Figure adapted from Ju (2022).*

Ligand-mediated activation of hM3Dq leads instead to intracellular Gq-mediated signaling cascade, enhancing neuronal firing and leading to desynchronized spiking activity at the population level (Campbell & Marchant, 2018). This manipulation can therefore be used to produce a generalized increase in neuronal excitability (and therefore increased E/I) when hM3Dq is expressed in pyramidal cells. An analogous outcome can be attained by expressing inhibitory DREADD hM4Di in inhibitory neurons via the use of double floxed constructs in Cre-expressing lines (Yizhar et al., 2011). This manipulation can reduce inhibitory output producing excitatory disinhibition. We have used both these strategies to causally link regional imbalances in E/I and network-level regional synchronization as measured with rsfMRI. We briefly report on the results of this study in chapter 4 below.

While chemo-fMRI allows for the functional deconstruction of network activity, some key methodological issues related to the use of this approach must be highlighted. First, the temporal resolution of chemogenetics is very low (i.e. hours). While the absence of DREADD precise temporal control can be problematic in behavioral research, this aspect does not appear to be an issue in

imaging studies in which a neural mass phenomenon like rsfMRI can greatly benefit from the prolonged modulation of large brain regions attainable with chemogenetics. A second noteworthy limitation of chemogenetics is the possible confounding contribution of off-target pharmacological effects, like in the case of the in vivo back-conversion of CNO into the antipsychotic drug clozapine (Gomez et al., 2017). While this phenomenon can result in unspecific effects, rigorous CNO dose management (Giorgi et al., 2017) or the use of more selective ligands (Bonaventura et al., 2019; Nagai et al., 2020) can minimize these contributions. Regardless of the ligand employed, it is however essential to consider that the accurate control of these effects requires the experimental use of a specific control group in which the baseline effect of the selected dose of DREADD actuator is rigorously assessed. To control for possible DREADD-related off-target effects, the studies we present in chapters 3 and 4 were designed to control for this confound by using a reference CNO-treated control arm. The results of our work show that these limitations can be accurately controlled, allowing for a proficient use of chemo-fMRI to deconstruct fMRI connectivity.

Chapter 2: Aim of this work

This work was aimed to probe the neural drivers of rsfMRI coupling via the implementation of cell-type-specific neural manipulations in the mouse. By examining how rsfMRI networks reconfigure in response to regional changes in neural activity, we sought to unravel the neural underpinnings and dynamic rules governing brain-wide rsfMRI coupling, paving the way to future decoding of corresponding (dys)connectivity signatures into physiologically interpretable signals.

In a first set of proof-of-concept investigations, we empirically probed the widely held notion that neural inhibition of a cortical node would result in reduced fMRI coupling of the silenced area and its long-range terminals (Chapter 3). To this aim, we chronically (Kir2.1 overexpression) and acutely (hM4Di activation) inhibited the mouse medial prefrontal cortex (PFC) and measured the ensuing pattern of rsfMRI connectivity and neural coupling via in vivo electrophysiology. Surprisingly, we found that these manipulations produce patterns of fMRI overconnectivity. Using *in vivo* electrophysiology, we identified a specific and mechanistically plausible neural signature for this phenomenon. Our results provide causal evidence that cortical inactivation can counterintuitively increase fMRI connectivity via enhanced, less-localized slow oscillatory processes, with important implications for neural modeling and interpretation of fMRI overconnectivity in brain disorders.

The observation that neural inhibition of the PFC results in fMRI overconnectivity allowed us to predict that neural activation of the same area might produce opposite results, i.e. fMRI underconnectivity and neural desynchronization. We thus chemogenetically excited prefrontal CaMKII positive PCs and inhibited PV positive neurons, hence increasing local E/I balance. Preliminary examination of the obtained results confirmed our predictions, showing that both manipulations produce similar rsfMRI signatures of rsfMRI underconnectivity, effectively reversing the neural signature observed in DREADD inhibition studies. We report a preliminary account of this ongoing work in chapter 4. Taken together, our investigations reveal a set of fundamental rules linking regional brain activity to macroscale functional connectivity, offering opportunities to physiologically interpret rsfMRI signatures of functional dysconnectivity in human brain disorders

Chapter 3: Increased fMRI connectivity upon chemogenetic inhibition of the prefrontal cortex

This Chapter will be published as:

"Increased fMRI connectivity upon chemogenetic inhibition of the prefrontal cortex"

Federico Rocchi*, Carola Canella*, Shahryar Noei*, Daniel Gutierrez-Barragan, Ludovico Coletta, Alberto Galbusera, Massimo Pasqualetti, Giuliano Iurilli, Stefano Panzeri, Alessandro Gozzi.

Accepted for publication, Nature communications, 2022

*shared first authorship

3.1 Introduction

A rapidly expanding approach to understand the functional organization of brain networks is to map large-scale patterns of spontaneous activity via non-invasive neuroimaging. The ease and reproducibility of "resting state" fMRI (rsfMRI) have promoted the widespread use of this approach, leading to the observation that spontaneous fMRI activity is organized into highly coherent functional networks, defined by temporally correlated fluctuations in BOLD signal (Power et al., 2014). The non-invasive nature of rsfMRI has fueled the use of this method to map intrinsic brain network organization in the healthy human brain, as well as in psychiatric or neurological conditions, in which evidence of disrupted or aberrant rsfMRI functional coupling has been largely documented (Power et al., 2014). However, despite the growing popularity of rsfMRI, our knowledge of the underpinnings of brain-wide fMRI coupling remains very limited.

Multiple lines of evidence suggest that structural and rsfMRI-based connectivity are robustly related (Power et al., 2014). First, structural and functional connection strengths are correlated both at the whole-brain and mesoscopic scale (Coletta et al., 2020; Hagmann et al., 2008; Z. Wang et al., 2013), and rsfMRI network topography closely recapitulates patterns of anatomical connectivity in several mammalian species (Coletta et al., 2020; Goñi et al., 2014; Honey et al., 2009). Second, experimental resection of callosal connections (O'Reilly et al., 2013) or chemogenetic inactivation of the amygdala result in reduced rsfMRI connectivity with regions anatomically linked to the manipulated area (Grayson et al., 2016). Lastly, computational modeling corroborates a tight relationship between structural and functional connectivity, as synchronous rsfMRI fluctuations can be modeled by dynamical systems endowed with realistic anatomical connectivity patterns of long-range axonal interactions (Ponce-Alvarez et al., 2015). Accordingly, simulated axonal lesions in these models result in reduced functional coupling (Alstott et al., 2009).

These observations have prompted the widespread use of statistical dependencies in spontaneous fMRI signal as an index of interareal functional communication (Power et al., 2014). However, the neural mechanisms linking regional brain activity to large-scale rsfMRI network connectivity remain unclear. For example, growing experimental evidence suggests that, while tightly constrained by underlying anatomy, rsfMRI connectivity may only partially reflect direct interactions between areas, as widespread BOLD signal modulation might arise via subcortical connections, whether through the thalamus via long-range loops (Gent et al., 2018), or as a result of diffuse neuromodulation mediated by brainstem nuclei (Liu et al., 2018; Munn et al., 2021). This notion is epitomized by the observation

of intact rsfMRI coupling among brain regions not directly structurally connected as in the case of acallosal humans, primates, and rodents (O'Reilly et al., 2013; Sforazzini et al., 2016; Tyszka et al., 2011). Moreover, rsfMRI network topography can dynamically reconfigure in response to local perturbations (Eldaief et al., 2011) or pathological processes (Pagani et al., 2021). In keeping with this, neurological disorders such as Parkinson's disease, stroke, and Alzheimer's disease have been often found to be associated with unexpectedly increased interareal rsfMRI connectivity despite the loss of cortical function characterizing these conditions (Hillary & Grafman, 2017; Siegel et al., 2016). Taken together, these observations point at a complex relationship between interareal brain activity and rsfMRI coupling, and call for a deeper investigation of the neural mechanisms underlying the reconfiguration of rsfMRI connectivity in response to varying interareal input or pathological perturbations.

Here we combine rsfMRI, neural and chemogenetic inhibition (chemo-fMRI (Giorgi et al., 2017)), and in vivo electrophysiology in the mouse to probe how inactivation of a cortical area causally affects rsfMRI coupling. Surprisingly, we find that chronic and acute inhibition of the medial prefrontal cortex (PFC), a core component of the mouse default mode network (DMN, Whitesell et al., 2021), can increase rsfMRI coupling with its thalamo-cortical targets. This effect is associated with decreased ϒ power in the suppressed region and robustly increased low frequency (0.1-4 Hz) electrophysiological coherence between functionally overconnected PFC targets. These findings reveal a highly dynamic, non-monotonic relationship between regional cortical activity and network-wide rsfMRI connectivity, and provide an interpretative framework for the observation of counterintuitively increased rsfMRI connectivity in pathological conditions characterized by impaired cortical function.

3.2 Methods

3.2.1 Ethical statement

All in vivo experiments were conducted in accordance with the Italian law (DL 26/214, EU 63/2010, Ministero della Sanità, Roma). Animal research protocols were reviewed and consented by the animal care committee of the University of Trento and Italian Ministry of Health (authorization no. 852/17 to A.G.). All surgical procedures were performed under anesthesia.

3.2.2 Animals

Adult (6 week old) male C57Bl6/J mice, and transgenic animals expressing Cre recombinase in parvalbumin-positive GABAergic neurons (B6.129P2-Pvalbtm1(cre)Arbr/J, (Cardin et al., 2009) were bred in house. Mice were housed with temperature maintained at 21 ± 1°C and humidity at 60 ± 10%.

3.2.3 Anatomical definition of mouse medial prefrontal cortex

Our anatomical definition of mouse medial prefrontal cortex (PFC) reflects recent neuroanatomical (Carlén, 2017) and cytoarchitectural cross-species comparisons (Vogt & Paxinos, 2014), according to which the mouse PFC comprises a prelimbic region, corresponding to primate Brodmann area 32 (A32), the anterior cingulate cortex, corresponding to Brodmann area A24b, and the infralimbic cortex, corresponding to Brodmann area A24a. Our viral manipulations were therefore aimed to inhibit an anatomical ensemble comprising all the above mentioned regions at the following coordinates, expressed in millimeter from Bregma: 1.7 from anterior to posterior, +/- 0.3 lateral, −1.7 deep (Paxinos & Franklin, 2004).

3.2.4 Viral injections

Mice were anesthetized with isoflurane and head-fixed in a stereotaxic apparatus (Stoelting). Injections were performed with a Hamilton syringe mounted on Nanoliter Syringe Pump with controller (KD Scientific), at a speed of 0.05 ul/min, followed by a 5–10 min waiting period, to avoid backflow of viral solution. To prevent layer- or cell-type specific expression (Nathanson et al., 2009), all in vivo viral transductions were carried out using high-titer (> 1013 vg/mL) viral suspensions. The

following injections volumes were employed: 300 nL (AAV8-hSyn-hM4D(Gi)-mCherry and AAV8-hSyn-GFP; http://www.addgene.org) or 2 µL (AAV8-hSyn-MYC-mKir2.1(E224G/Y242F)-IRES-GFP, Xue et al. 2004, http://www.vectorbiolabs.com or AAV8-hSyn-GFP http://www.addgene.org), or 1 µL (AAV8-CamkII-hM3D(Gq)-mCherry; http://www.addgene.org) or 300 nL (AAV9-hSyn-DIO-hM4D(Gi)-mCherry; http://www.addgene.org) of viral suspension were injected bilaterally in the mouse PFC (see coordinates above). Control groups for both CamkII-hM3D(Gq) and PV-hM4D(Gi) were obtained by sham-injecting genotype-matched littermates. rsfMRI or electrophysiological recordings were carried out no sooner than three weeks after the injection to allow for maximal viral expression.

3.2.5 rsfMRI acquisitions

The animal preparation protocol was recently described in detail (Ferrari et al., 2012; Gutierrez-Barragan et al., 2019; Sforazzini et al., 2014). Briefly, mice were anesthetized with isoflurane (5%, induction), intubated and artificially ventilated (2%, surgery). The left femoral artery was cannulated for continuous blood pressure monitoring. At the end of surgery, isoflurane was discontinued and substituted with a shallow halothane regimen (0.75%) to obtain light sedation and to preserve cerebral blood flow auto-regulation (Gozzi et al., 2007). Ventilation parameters were adjusted to maintain normo-physiological paCO2 (< 40 mmHg) and paO2 levels (> 90 mmHg, corresponding to >98% hemoglobin saturation). To probe the generalizability of our findings, we also repeated our inhibitory chemo-fMRI manipulations under a combination of medetomidine and low-dose isoflurane (0.05 mg/kg bolus and 0.1 mg/kg/h IV infusion, plus 0.5% isoflurane, (Grandjean et al., 2020; Lee et al., 2021).

rsfMRI data acquisition commenced 30 min after isoflurane cessation. Functional images were acquired with a 7T MRI scanner (Bruker, Ettlingen) equipped with a BGA-9 gradient set (380 mT/m, max. linear slew rate 3,420 T/m/s) as previously described (Liska et al., 2015), using a 72 mm birdcage transmit coil and a 4-channel solenoid coil for signal reception. Single-shot BOLD rsfMRI time series were acquired using an EPI sequence with the following parameters: TR/TE 1000/15 ms, flip angle 60°, matrix 98 x 98, FOV 2.3 x 2.3 cm, 18 coronal slices, slice thickness 550 µm, bandwidth 250 KHz. rsfMRI acquisition with Kir2.1-transduced (AAV8-hSyn-MYC-mKir2.1(E224G/Y242F)-IRES-GFP, n = 16) and control mice (AAV8-hSyn-GFP, n = 19) encompassed 35-minute long timeseries, corresponding to 2100 volumes.

Chemo-fMRI acquisitions comprised two consecutive rsfMRI timeseries, encompassing 1800 volumes (30 min) and 2100 volumes (35 min), respectively. CNO (2 mg/kg, Sigma Aldrich) was injected intravenously fifteen minutes (volume #900) after the start of the first scan. The first 900 fMRI volumes of this first timeseries scan were used as pre-CNO baseline rsfMRI reference in time-resolved analyses. Based on the pharmacokinetic profile of CNO, the post CNO window was split into temporal domains as follows: the first 15 min post injection (900 volumes) were considered part of a drug equilibration window, while the following 35 min (2100 volumes) were considered to cover the DREADD active time window (Trakoshis et al., 2020). All group comparisons in the chemo-fMRI study were carried out within this latter time window, unless otherwise stated. After post-mortem analyses of viral expressions, a total of n = 15 hM4Di and n = 19 GFP-transduced animals were retained for analyses.

3.2.6 Image preprocessing and analysis

Raw rsfMRI timeseries were preprocessed as described in previous work (Gutierrez-Barragan et al., 2019; Sforazzini et al., 2014). Briefly, the initial 120 volumes of the time series were removed to allow for thermal gradient equilibration. Data were then despiked, motion corrected, and spatially registered to a common reference template. Motion traces of head realignment parameters (3 translations + 3 rotations) and mean ventricular signal (corresponding to the averaged BOLD signal within a reference ventricular mask) were used as nuisance covariates and regressed out from each time course. All rsfMRI time series also underwent band-pass filtering within a frequency window of 0.01–0.1 Hz (halothane) or 0.01-0.25 Hz (MED-ISO, Grandjean et al., 2020) followed by spatial smoothing with a full width at half maximum of 0.6 mm. To control for the effects of global fMRI signal regression on the mapped changes, all rsfMRI timeseries were also recomputed by regressing average fMRI signal within an intracerebral mask

rsfMRI connectivity of the mouse DMN in Kir2.1 and chemo-fMRI scans was probed using a seed-based approach. In the case of the chemo-fMRI study, this quantification was carried out during the CNO active time window. A 5x5x2 seed region was selected to cover the PFC areas targeted by viral injections. Voxel-wise intergroup differences in seed-based mapping were assessed using a 2-tailed Student's t test ($|t| > 2$, $p < 0.05$) and family-wise error (FWE) cluster-corrected using a cluster threshold of $p = 0.05$ as implemented in FSL (https://fsl.fmrib.ox.ac.uk/fsl/). The antero-posterior connectivity profile of the DMN was assessed by computing Person correlation between the PFC seed

abovementioned and a series of 6 x 6 x 2 voxel seeds placed along the midline extension of the cingulate and retrosplenial cortices as previously described (Pagani et al., 2019). Quantification of cortico-thalamic connectivity was carried out with respect to a meta-regional parcellation of the mouse cortex in volumes-of-interest. To rule out a possible confounding contribution of spurious neurovascular changes in CNO-induced rsfMRI connectivity alterations, we calculated and statistically compared the characteristic hemodynamic response function between Kir2.1 and control mice, and between hM4Di-expressing and control mice upon CNO-administration (active phase), as previously described (Pagani et al., 2019; Wu et al., 2013).

Whole-brain connectivity in hM4Di and Control mice was calculated across a set of volumes of interest recapitulating anatomical areas of the Allen brain atlas. The anatomical probed area were selected according to their coverage of previously characterized network systems of the mouse brain (Liska et al., 2015; Sforazzini et al., 2014; Whitesell et al., 2021): TH: thalamus (thalamus polymodal association cortex related, Thalamus Sensory-Motor cortex related); STR: striatum (Striatum dorsal region left, striatum dorsal region right, striatum ventral region left, striatum ventral region right); LCN: lateral cortical network (LCN: primary motor cortex left, primary motor cortex right, primary somatosensory cortex left, primary somatosensory cortex right, secondary somatosensory cortex left, secondary somatosensory cortex right, Lateral septal complex left, lateral septal complex right); HCP: hippocampus (Ammon's horn left; Ammon's horn right, dentate gyrus left; dentate gyrus right, Entorhinal area left, entorhinal area right, subiculum left, subiculum right); DMN: default mode network (anterior cingulate area; Infralimbic area, secondary motor cortex left, secondary motor cortex right, orbital area, prelimbic area, posterior parietal association areas left, Posterior parietal association areas right, retrosplenial area);

To relate the strength of underlying anatomical connectivity to the regions exhibiting increased rsfMRI connectivity with voxel resolution, we extracted outgoing projections from the affected PFC regions using a spatially-resampled (0.027 mm3) version of a voxel scale model of the Allen Brain Institute structural connectome (Coletta et al., 2020). We then plotted the strength of PFC-departing structural projections against the corresponding between-group difference in rsfMRI connectivity using the cluster-corrected difference map and assessed differences in the distribution of overconnected areas with respect to all the brain voxels using a Wilcoxon rank-sum test.

To quantify the contribution of distinct thalamic subregions to overall group differences, we used k-means clustering to partition voxels within the thalamus, based on whole-brain rsfMRI group-

difference obtained using the PFC seed as recently described (Schleifer et al., 2019; Vassilvitskii & Arthur, 2006). This approach revealed two major thalamic clusters, one medial and one bilateral partition encompassing sensory areas. Seed-based functional connectivity was subsequently computed for each of the two-resultant k-means clusters independently, and the resulting functional connectivity maps were compared and quantified across cortical VOIs.

3.2.7 Electrophysiological recordings

Electrophysiological recordings were carried out in animals subjected to the same animal preparation and sedation regime employed for rsfMRI mapping (Ferrari et al., 2012; Sforazzini et al., 2014). Briefly, mice were anesthetized with isoflurane (5% induction), intubated, artificially ventilated (2% maintenance), and head-fixed in a stereotaxic apparatus (Stoelting). The tail vein was cannulated for CNO injection. To ensure maximal consistency between viral injections and recording site, the skull surface was exposed and an insertion hole in the right PFC was gently drilled through the skull corresponding to the location of prior viral injection point. A single shank electrode (Neuronexus, USA, interelectrode spacing 1 - 2.5 mm) was next inserted through the overlying dura mater by a microdrive array system (Kopf Instruments, Germany) at an insertion rate of 1 µm/min to reach the same stereotaxic coordinates employed for viral injection. The site receptive fields were plotted manually and the position and size of each field were stored together with the acquisition data. After electrode insertion, isoflurane was discontinued and replaced by halothane at a maintenance level of 0.75% to induce rsfMRI-comparable sedation. Electrophysiological data acquisition commenced 1 hour after isoflurane cessation. Such transition time was required to ensure complete washout of isoflurane anesthesia and avoid residual burst-suppressing activity associated with extended exposure to deep anesthetic levels.

Neural activity was next recorded in consecutive 5 min time bins to cover a 15 min pre-injection time window, and a 60 min post CNO timeframe in n = 5 hM4Di and n = 5 GFP-expressing mice. Signals were amplified using an RHD 2000 amplifier system (Intan Technologies) at a sampling rate of 20 kHz. For CamkII-hM3D(Gq) (n = 4) and PV-hM4D(Gi) (n = 6) experiments we acquired respectively n = 4 and n = 7 control animals. In the case of control Kir2.1 recordings, a four shank electrode was inserted along the coronal plane to bi-hemispherically cover the right (Kir2.1-expressing) and left (GFP-expressing) PFC (n = 4). The left region served as internal reference control

to better assess the efficacy of Kir2.1 neural inhibition. Electrophysiological signals were then recorded into 5 min time bins to cover a 35 min time-window.

To measure multi-electrode coherence, three electrodes were inserted in key cortical and subcortical substrates identified as overconnected in our chemo-fMRI mapping in n = 4 hM4Di and n = 5 GFP-expressing mice. A multi-probe micromanipulator (New-Scale Technologies) was used to insert three 16 channels single shank electrode (Neuronexus, USA, interelectrode spacing 1 - 2.5 mm) in the right prefrontal cortex, centromedial thalamus and retrosplenial cortex, respectively. Representative electrode locations are reported in Figure 3.1, corresponding to the following stereotaxic coordinates: PFC 1.7 mm AP, +/- 0.3 mm ML, -1.7 mm DV; mediodorsal thalamus: -1.7 mm AP, -0.3 mm ML, -3.5mm DV (5° insertion angle); retrosplenial cortex: -2.4 mm AP, -0.3 mm ML, -1.3 mm DV. To reduce tissue damage, an insertion rate < 1 µm/min was employed, allowing for a 30 minute equilibration every 400 µm traveled. Ground electrodes were put in contact with the cerebral brain fluid through a window drilled in the skull. Signals were then recorded into 1 min time bins to cover a 15-min pre-injection baseline and a 40-min post CNO time window.

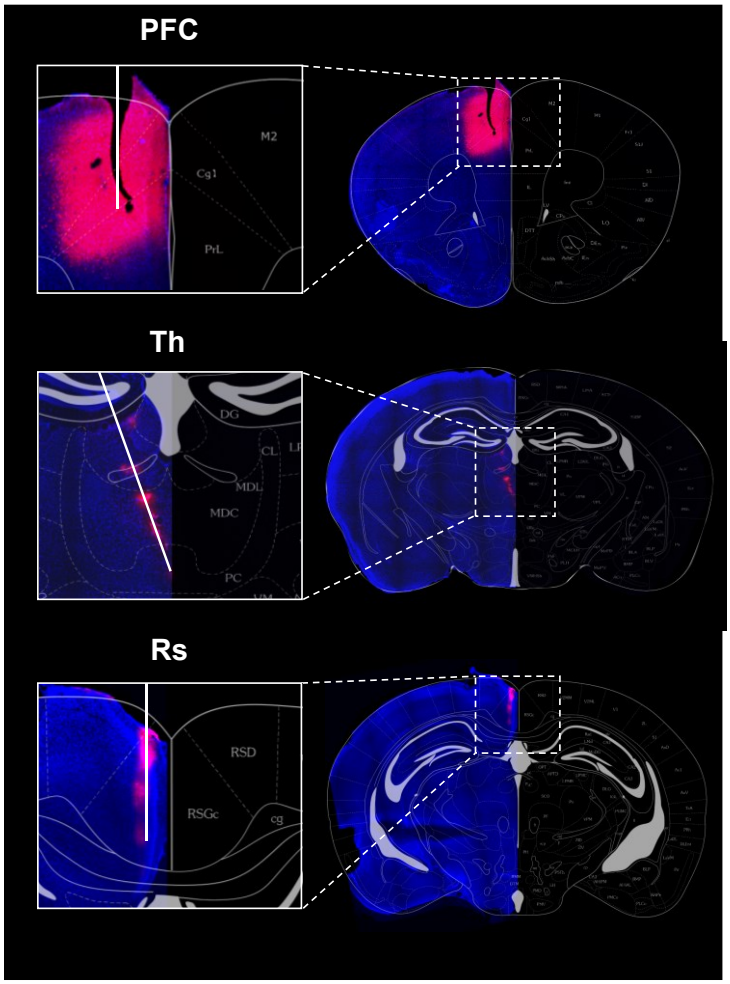

Figure 3.1 Histological validation of electrode placement. *Electrode insertion traces (Th and Rs, red, lipophilic dye DiI) are here highlighted with a white line to indicate approximate electrode profile and insertion angle. In the PFC, red signal represents hSyn-hM4Di viral expression, and area of electrode insertion is indicated by a the corresponding mechanically-induced lesion produced before electrode removal at the end of recording session. Individual color channels have been adjusted to increase contrast. PFC: medial prefrontal cortex; Th: thalamus; Rs: retrosplenial cortex.*

LFP and multi-unit activity (MUA). To compute the LFP signal, raw extracellular recordings were first down-sampled to 4 kHz, then band-pass filtered to 1-250 Hz using a previously published two-step procedure (Belitski et al., 2008). Briefly, raw timeseries were first low-pass filtered using a 4th order Butterworth filter with a cut-off frequency of 1 kHz. The resulting timeseries were next down-sampled to 2 kHz, then again filtered using a Kaiser window filter between 1Hz to 250Hz (with a sharp transition bandwidth of 1Hz, passband ripple of 0.01 dB and a stop band attenuation of 60 dB) and then resampled at 1 kHz. All the filtering was applied both in forward and backward temporal direction to avoid any phase transitions due to filtering.

To compute multi-unity activity (MUA) we again followed the procedure described in (Belitski et al., 2008). Briefly, we computed a band-passed high-frequency signal using a 4th order Butterworth filter with a <100 Hz cut off frequency, then band-pass filtered between 400 and 3000 Hz using a Kaiser window filter (with transition band of 50 Hz, stopband attenuation of 60 dB, and passband ripple of 0.01 dB). From the high frequency signal we detected spike times using a spike detection threshold corresponding to 4-times the median of the high frequency signal, then divided by 0.6745 as suggested in (Quiroga et al., 2004). Spikes were considered to be biologically plausible, and as such retained in these computations, only if occurring more than 1 ms apart.

To quantify effectiveness of Kir2.1 in suppressing spontaneous activity, firing rate was computed (in units of spikes/s) by dividing the number of spikes per electrode by the recording duration in seconds. The resulting spike rates were averaged across the channels corresponding to the virally targeted or control region. The average spike rate for four subjects was next tested against each other using paired t test. To assess the effect of chemo-fMRI manipulations, spiking activity was computed in experimental and control animals as described above and segmented into one-minute bins. We next computed the channel averaged firing rate for each segment, and normalized this value with respect to the firing rate recorded during baseline (pre-CNO) period. The resulting baseline normalized firing rate index was then used to assess changes in spiking rate upon CNO injection in the two experimental cohorts.

To determine the time lag at which different firing rate samples from the same channels could be considered as approximately statistically independent, we computed for each subject the autocorrelation of the channel-averaged firing rate for each subject and computed the time lag after which the autocorrelation function drops below the 95th percentile. We then, for each subject, retained samples of the baseline-normalized firing rate at different times separated by the above obtained lags. We next separately analyzed the baseline-normalized rates in three different periods: 0 to 15 minutes (transient time), 15 to 35 minutes, and 35 to 55 minutes after CNO the injection (active time). We pooled all the retained data points in these windows both over time and over subjects and then compared the median between the two populations using a two-sided Wilcoxon rank-sum test. The obtained p-values were corrected using a Benjamini-Hochberg FDR correction.

LFP spectrograms were computed using a Fourier transform with a Kaiser window with a frequency resolution of 0.15 Hz, temporal resolution of 6 seconds, and with 50% overlapping windows. Spectrograms and their differences were smoothed in time with the resolution of 30

seconds, and in frequency with the resolution of 1Hz using a median filter. To quantify the effect of CNO on LFP rhythms, we computed a spectrogram modulation index as follows. First, we computed the channel-averaged spectrograms for the duration of the baseline recording. Next, we averaged time-frequency spectral profiles over time, resulting in frequency-resolved spectral profiles. The effect of CNO was next assessed by computing a modulation index, defined as the ratio of channel-averaged spectrogram after injection minus baseline, time-averaged spectrogram, and the sum of the same quantities, for every time window and for every frequency. This modulation index ranges between -1 and 1 and describes the changes due to drug injection over time for each frequency.

To obtain a statistical assessment of CNO effects across groups and bands, we computed the autocorrelation of spectrograms for every subject at every frequency, using (as for our assessment of firing rate) only spectrograms computed at time points far enough to be approximately statistically independent. The time lag to determine such approximately independent points was identified as the interval after which the spectrum's autocorrelation function dropped below the 95th percentile. We next computed the median of the modulation index over different frequency bands defined as follows: slow (0.1-1 Hz), δ (1-4 Hz), θ (4-8 Hz), α (8-12 Hz), β (12-30 Hz) and γ (30-70 Hz). Data within each band were pooled over uncorrelated time points (determined as above by taking time samples separated by lags at which autocorrelation became negligible) and over subjects, and the population medians were compared using two-sided Wilcoxon rank-sum tests, followed by FDR correction.

3.2.8 Multielectrode coherence

Channel averaged spectrograms were preprocessed as described above. Raw spectral power coherence was assessed by computing the magnitude of squared coherency using Welch's overlapped averaged periodogram method (Welch, 1967) with a 50% overlapping window of 2 seconds length. Coherence was calculated for every 60-second bin of channel-averaged recordings. Temporal smoothing was carried out using a 60-second median filter as described above. CNO spectrograms (30-40 post CNO injection window) were normalized with respect to the last 3 minutes of pre-CNO baseline using a modulation index as before. To obtain a quantifiable assessment of the CNO effect across different groups and bands, data within each band were pooled into 60-second bins. Subject and the population medians were compared for each region separately using one-sided Wilcoxon rank-sum tests, followed by FDR correction. The use of 60 second bins was motivated by estimations of the time lags at which autocorrelation of electrophysiological signals drops below the 95th percentile value (and thus samples are approximately independent) as described above.

To assess changes in ultra-slow fluctuations in the ϒ band envelope of LFP, following the work from Nir et al. (2008), we computed LFP data spectrogram for the last 10 minutes of baseline and 30 to 40 minutes of post injection window, using a moving window of 2 seconds width and 0.75 percent overlap, resulting in an estimation of the resulting ultra-slow power for each 0.5 second interval. The ϒ-band envelope was computed as the integrated power of the spectrograms in the ϒ band (30-70 Hz), following previously published procedures (Mateo et al., 2017). The power spectrum of this time series was next computed, after correction for 1/f component (Mateo et al., 2017), revealing a peak in the 0.02-0.05 Hz region. Interareal coherence was then computed as described above for both experimental and control mice. To assess the effect of chemogenetic manipulations, we defined a coherence modulation index as described above for other frequency bands. Between group statistical assessments were carried out using two-sided Wilcoxon rank-sum tests, followed by FDR correction.

To quantify interregional phase coupling, LFP data were first filtered using a third order Butterworth filter in delta band, and the instantaneous phase of each channel was computed by taking the phase of the analytical signal resulted from the Hilbert transform. For all possible pairs of channels belonging to two different regions, we next computed the corresponding Phase Locking Value (PLV) as follows:

$$\mathrm{PLV} = \frac{1}{\mathrm{N}}\left|\sum_{j=1}^{N} e^{i\left(\theta_{ch1}(t_j)-\theta_{ch2}(t_j)\right)}\right|$$

Where N is the number of data points in time and $\theta_{ch1}(t_j), \theta_{ch2}(t_j)$ are the instantaneous phase of the LFP of channel 1 and 2 at time j. The PLV value for each pair during the 30 to 40 minutes post CNO was next normalized with respect to the PLV value of the last 3 minutes of the pre-CNO baseline using a modulation index and was pooled over channel pairs and animals. The obtained population medians of the control and experimental group for each region pair were next compared using two-sided Wilcoxon rank-sum tests, followed by FDR correction.

3.2.9 Power spectrum of simulated spiking activity

To understand whether the increase in δ and slow LFP power observed with DREADD-induced inhibition could be explained by selective elimination of spikes not occurring at the preferred, most excitable, phase of the considered oscillation, we simulated 10 seconds epochs of spikes locked to a

cosine “LFP” wave oscillating at 1 Hz. In the first scenario, representing the DREADD conditions, we generated 100 spikes (rate of 10 spikes per second) tightly distributed around the preferred phase π with values taken from a von Mises distribution with an extremely high value (20) of the concentration parameter. For the second case (representing sham condition), we added 100 more spikes distributed almost randomly across phases, with values taken from a von Mises distribution with an extremely low value (0.5) of the concentration parameter. We then smoothed spike temporal components with a Gaussian kernel (100 ms width) and computed the power spectra of the resulting spike train with the multitaper method (Matlab pspectrum function).

3.2.10 Relationships between spikes and LFP phases

We computed at each time point the phase of the LFP in a given frequency band as the angle of the Hilbert transform of the band passed LFP. We considered for this analysis the slow and δ bands. Signal in each band was band-passed using a 3rd order Butterworth filter. To measure the locking of spikes to specific phases of each band, we considered the distribution of the LFP phase values at the time of each MUA spike. From this distribution, we computed the phase locking value (PLV) as 1 minus the circular variance of this distribution (Methods Section “Multielectrode coherence”). PLV ranges from 0 (no locking or relationship between phase and spike times) to 1 (perfect locking of spikes to a certain phase). As for other quantities, we also computed a PLV modulation index as the difference of PLV values between the active-drug and baseline periods divided by the sum of PLV values in the active-drug and baseline periods. A two-sided Wilcoxon was used to check if the median PLV modulation index is higher for the experimental data with respect to control data.

Violin plot representations of all electrophysiological analyses include individual statistically-independent points (see above) used for intergroup comparisons. Plots were generated using Prism Graphpad 9.1. Plot truncation at extremities is introduced by the software to avoid representation of kernel density-related fictitious values above the highest data value or below the smallest.

3.2.11 LFP-LFP phase differences

To characterize the phase differences across areas, we computed the distribution across time of the difference in the instantaneous phase (computed as explained above) of PFC and Rs electrode pairs. From this distribution, we considered a channel pair to have significant PLV (see

"Multielectrode coherence" section above) if its PLV value exceeded the 95th percentile of surrogate PLV distribution obtained by shuffling LFPs in time prior to filtering, and if the same PLV value was also greater than 0.1. We report in Fig. 3.10 the distribution of preferred phase differences (the circular mean of the phase difference distribution) for these significant channels. In the same figure, we also report (as thick lines) the values of the circular mean across all significant channels in each condition. We here report only the results of retrosplenial and PFC electrode pairs in the δ band, because this was the only combination exhibiting very stable mean circular phases across all baseline conditions and during the active time of the control injection. Circular and statistics were all computed with CircStat package (Berens, 2009).

3.3 Results

3.3.1 rsfMRI overconnectivity upon chronic inactivation of the mouse prefrontal cortex

The robust structural foundations of rsfMRI connectivity suggest that neural inhibition of a network node would result in diminished functional coupling with regions receiving direct axonal projections from the inactivated region (Alstott et al., 2009; Grayson et al., 2016; Suárez et al., 2020). To test this prediction and more broadly investigate how rsfMRI dynamically reconfigures in response to local neural suppression, we carried out rsfMRI measurements in a cohort of mice in which neuronal activity in PFC was chronically inhibited via bilateral viral transduction of the inward rectifying potassium channel Kir2.1 (Fig. 3.2a). Our interest in the PFC was motivated by its translational relevance as a key component of the mouse default mode network (DMN), a major phylogenetically conserved rsfMRI network that in rodents is composed by three hubs, namely the PFC, the retrosplenial cortex and the medial thalamus (Coletta et al., 2020; Whitesell et al., 2021). Prior research in awake animals has shown that virally-mediated Kir2.1 expression results in a reduction of both evoked and spontaneous neuronal excitability lasting several weeks (Beier et al., 2017; Xue et al., 2014). In keeping with this, in vivo electrophysiological recordings in the PFC of mice unilaterally transduced with Kir2.1 revealed a robust reduction of spontaneous firing rate in the targeted cortical area with respect to its contralateral control regions ($N = 4$, paired t test, $p = 0.002$, Fig. 3.3).

We next compared the patterns of rsfMRI connectivity in Kir2.1 and GFP-transduced control littermates by imaging Kir2.1 transduced mice four weeks after viral injections (Fig. 3.2a). Consistent with previous investigations (Bertero et al., 2018; Pagani et al., 2019), seed-based probing revealed significant long-range correlation between the PFC and thalamo-cortical components of the mouse DMN in both cohorts (Fig. 3.2b). Surprisingly, between-group comparisons revealed foci of significantly increased rsfMRI connectivity in the posterior cingulate/retrosplenial cortex and centromedial thalamic regions of Kir2.1 transduced mice (t test, $p < 0.05$, $t > 2.03$, FWE cluster-corrected, $p < 0.05$; Fig. 3.2c). Regional quantifications of DMN connectivity via multiple prefrontal-DMN seeds corroborated these findings, revealing increased rsfMRI synchronization along the entire midline extension of this network (two-way repeated measures ANOVA, $F_{1, 33} = 6.93$; $p = 0.013$; Fig. 3.2d) and its centromedial thalamic targets (t test, $t_{33} = 2.589$, $p = 0.014$; Fig. 3.2e). Voxel-wise mapping did not reveal any foci of reduced functional connectivity with the PFC ($t > 2.03$, FWE cluster-corrected, $p < 0.05$). Importantly, all the thalamic and cortical regions showing increased rsfMRI

connectivity in Kir2.1 mice are characterized by high axonal projection density from the PFC, as seen by comparing the magnitude of inter-group rsfMRI connectivity differences with incoming axonal connectivity strength inferred from a voxel-model of the mouse brain connectome (Coletta et al., 2020) (Fig. 3.2f, Wilcoxon rank-sum test, $p<0.0001$). Interestingly, the direction and anatomical location of DMN rsfMRI overconnectivity was not altered by global fMRI signal regression (Fig. 3.4), with the exception of thalamic areas, in which the connectivity difference between groups was attenuated. Together, these findings reveal that chronic inhibition of neural activity in the PFC may counterintuitively increase rsfMRI functional connectivity between long-range thalamo-cortical targets of the mouse DMN.

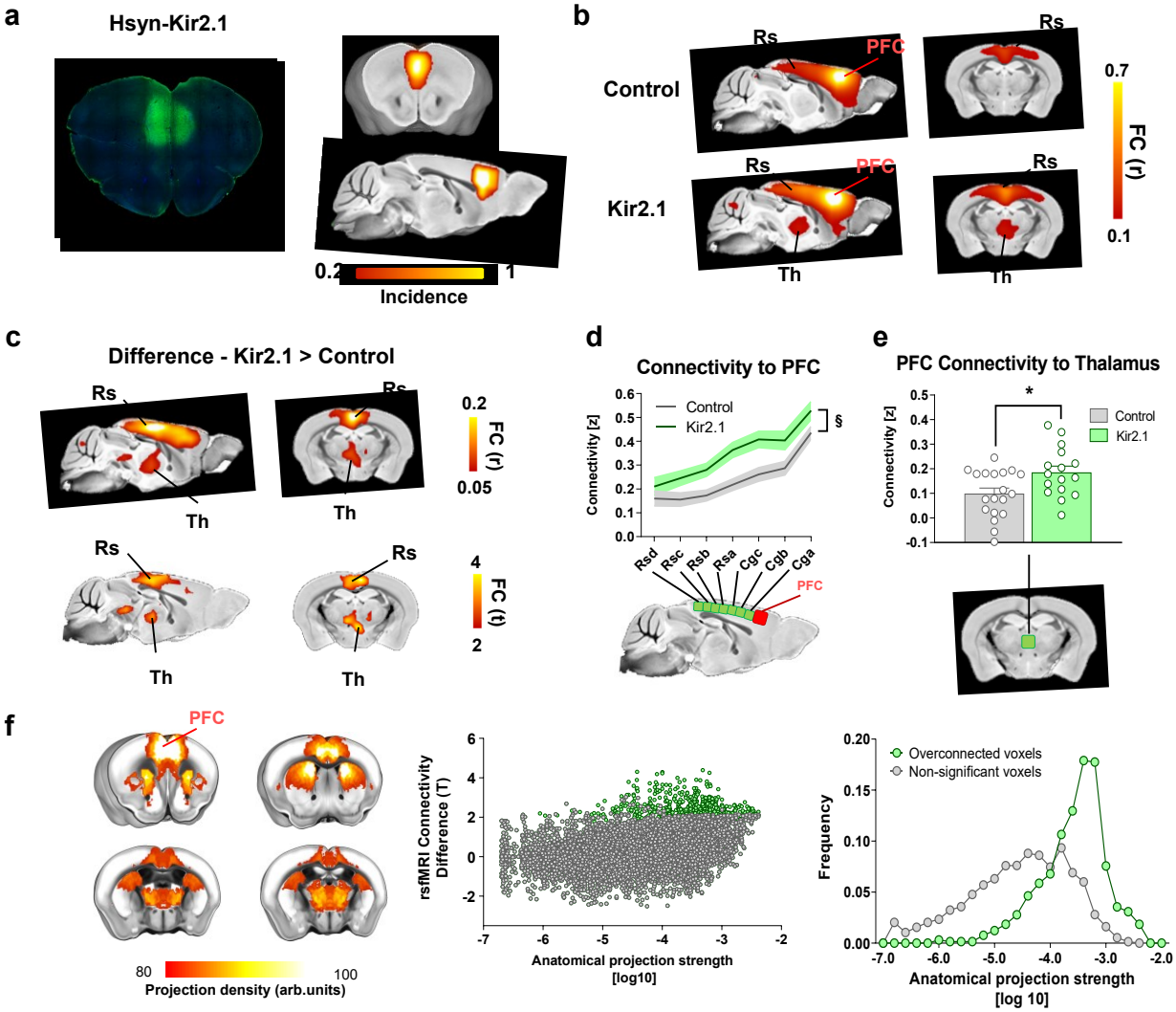

Figure 3.2 Chronic inhibition of the mouse PFC results in rsfMRI overconnectivity (a) *Viral expression localization. The potassium channel Kir2.1 (n = 16) or GFP (control, n = 19) were transduced bilaterally into the PFC of adult male mice. Left: Representative histology sample shown Kir2.1 (green). Right: Heatmaps illustrate a qualitative*

regional assessment of viral expression across subjects. ***(b)*** *Seed based connectivity mapping of the PFC in GFP (control), and Kir2.1-transduced subjects.* ***(c)*** *Corresponding group difference maps. Area exhibiting significantly increased rsfMRI connectivity in Kir2.1 expressing mice are depicted in red-yellow (r and T stat difference map).* ***(d)*** *Antero-posterior profiling of rsfMRI connectivity of the PFC within the midline axis of the mouse DMN (§ p = 0.014, two-way ANOVA with repeated measurements, genotype effect, n = 16 and n = 19 Kir2.1 or GFP-expressing mice, respectively).* ***(e)*** *Fronto-thalamic rsfMRI overconnectivity in Kir2.1 expressing mice (*p = 0.014, two-sided t test, n = 16 and n = 19 Kir2.1 or GFP-expressing mice, respectively). Data in (e) and (f) are presented as mean values ± SEM.* ***(f)*** *Regions exhibiting rsfMRI overconnectivity in Kir2.1 mice are robustly innervated by the PFC. Left: Axonal projections from the PFC (top 20% strongest connections). Middle: scatter plot illustrating intergroup differences in rsfMRI connectivity as a function of PFC structural connectivity strength. Green dots indicate significantly functionally overconnected voxels. Right: Distribution of overconnected voxels as a function of axonal connectivity strength Green. FC: functional connectivity; DMN: Default Mode Network; Cg: cingulate cortex; PFC: prefrontal cortex, RS: retrosplenial; Th: Thalamus.*

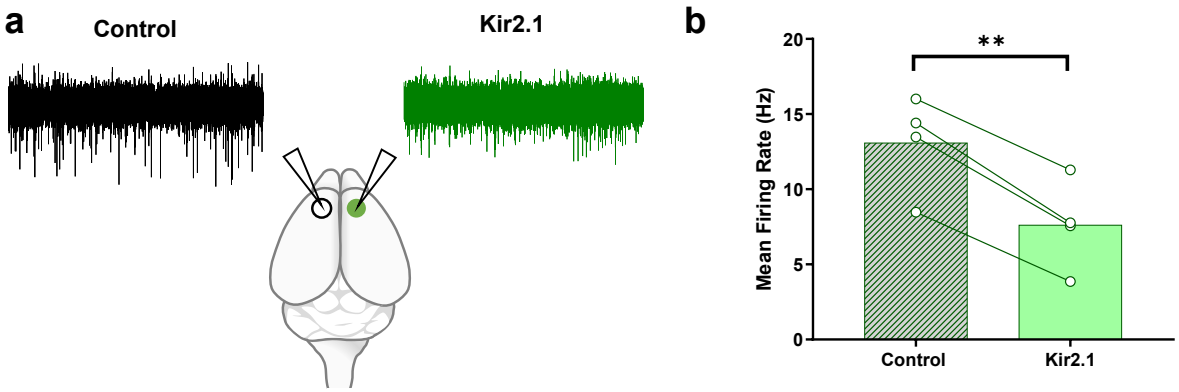

Figure 3.3 Overexpression of the potassium channel Kir2.1 in the PFC reduces spontaneous neural activity. (a) *Experimental design: Kir2.1 injection was performed unilaterally in the right PFC. A viral vector encoding GFP was injected in the contralateral area. Electrophysiological recordings were carried out bilaterally using a four-shank electrode.* ***(b)*** *Mean spontaneous firing rate for the control side (no Kir2.1 expression), and the side expressing Kir2.1. (n=4; ** p = 0.002, two-sided paired t-test).*

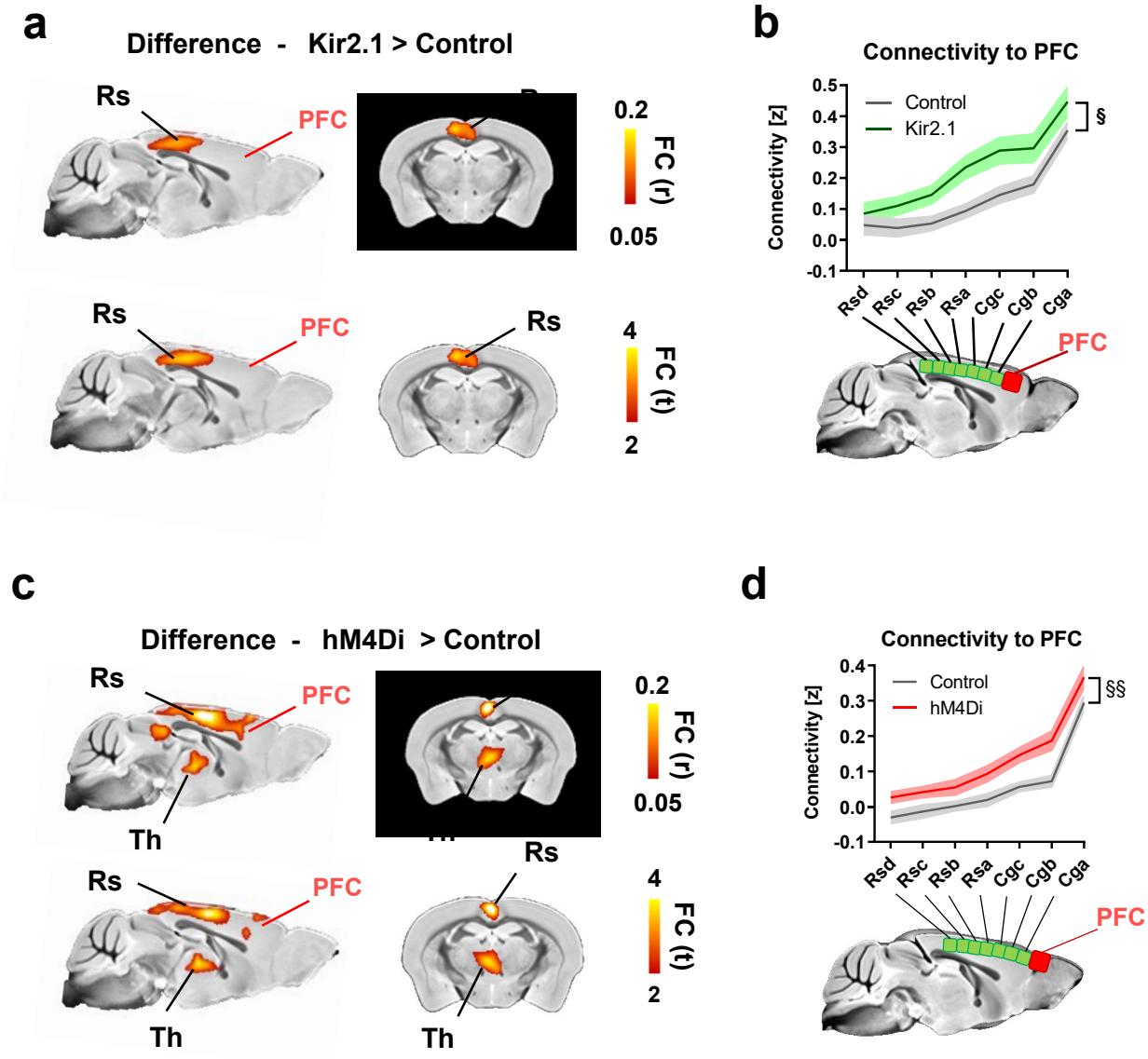

Figure 3.4 rsfMRI overconnectivity in Kir2.1 and DREADD-expressing mice persists after global fMRI signal regression. ***(a)*** *Between-group difference maps (Pearson's r, and corresponding T stat difference maps). rsfMRI connectivity was here computed after fMRI global signal regressions.* ***(b)*** *Antero-posterior profiling of rsfMRI connectivity of the PFC along the midline axis of the mouse DMN in the two cohorts revealing consistent overconnectivity in Kir2.1 mice (§ p = 0.013, 2-way ANOVA repeated measurements, genotype effect, n = 16 and n = 19 Kir2.1 or GFP-expressing mice, respectively).* ***(c-d)*** *rsfMRI overconnectivity in hM4Di mice is not affected by rsfMRI global signal regression* ***(c)*** *Between-group difference maps (Pearson's r, and corresponding T stat difference maps, two-sided).* ***(d)*** *Antero-posterior profiling of rsfMRI connectivity of the PFC along the midline axis of the mouse DMN in the two cohorts upon fMRI global signal regressions (§§ p < 0.001, 2-way ANOVA repeated measurements, genotype effect, n = 15 and n = 19 hM4Di or GFP-expressing mice, respectively). Data in (b) and (d) are presented as mean values ± SEM. Cg: cingulate cortex; PFC: prefrontal cortex, RS: retrosplenial cortex, TH: Thalamus; FC: functional connectivity.*

3.3.2 rsfMRI overconnectivity upon acute chemogenetic inactivation of the mouse prefrontal cortex

To corroborate the specificity of Kir2.1 findings and obtain mechanistic insight into the neural correlates of the observed fMRI overconnectivity, we designed a new set of experiments in which DREADD-based chemogenetics was employed to induce a time-controlled, acute inhibition of PFC activity during rsfMRI scanning. It should be noted that the same manipulations we hereafter refer to as "chemogenetic inhibition/inactivation", are often termed and interpreted as "chemogenetic silencing" in neuro-behavioral neuroscience (Wiegert et al., 2017).

An overview of experimental procedures is provided in Figure 3.5. To enable remote inhibition of fronto-cortical activity, we bilaterally transduced the PFC with the inhibitory hM4Di DREADD using a pan-neuronal promoter (Figure 3.5a), a strategy widely used to regionally inhibit excitatory neural function in behavioral studies (Wiegert et al., 2017). In keeping with previous investigations, the use of a high titer viral suspension resulted in reliable and homogeneous transduction of neurons across cortical layers (Nathanson et al., 2009). Three weeks after viral injection, control (GFP- transduced) and hM4Di-expressing animals underwent rsfMRI scanning or electrophysiological recordings before and after intravenous injection of the DREADD activator clozapine-N-oxide (CNO). To account for the relatively slow pharmacokinetic profile of CNO in the rodent brain (Jendryka et al., 2019; Trakoshis et al., 2020), both imaging and electrophysiological recordings were split into a pre-CNO injection baseline, a transitory (0 -15 min) drug-equilibration period, and an active time window (15-50 min post CNO injection) to which all our analyses refer to, unless otherwise specified (Fig. 3.5b-c).

To test the efficacy of chemogenetic inhibition, we first performed a set of electrophysiological recordings in the PFC of hM4Di- or GFP-transduced control animals prior to and after CNO administration, under the same experimental conditions used in rsfMRI imaging (Fig. 3.5d-e). Baseline electrophysiological traces revealed the presence of appreciable spontaneous multi-unit activity in the PFC of both groups (mean firing rate 15.0 ± 2.2 spikes/s in hM4Di-expressing, and 14.1 ± 3.8 in GFP-transduced mice, n = 5 each group, $p = 0.85$, t test). As expected, CNO administration robustly inhibited firing rate in hM4Di expressing mice, but not in control subjects (Fig. 3.5e-f, $p<0.01$ FDR corrected, t test). DREADD-induced PFC inhibition was characterized by a gradual decrease of neural firing upon CNO administration, reaching a steady-state approximately 10-15 min after the intravenous bolus (Fig. 3.5f).

Prompted by recent work suggesting that DREADDs may alter or disrupt, rather than completely silence, neuronal activity in vivo (Schmidt et al., 2019), we next examined more in detail

the firing patterns of individual electrode sites in multi-unit activity (MUA) recordings. For each group, we compared the firing rates of each MUA site under basal conditions with those obtained in the same recording site upon CNO administration. A scatterplot of spike rate across paired conditions revealed that, during the active phase, the vast majority of MUA sites in DREADD-expressing mice showed a marked decrease in firing rate, with virtually no site showing any appreciable decrease in firing in control animals (Fig. 3.5g). Given that MUA is strongly biased by the spiking activity of pyramidal neurons (Logothetis, 2008), these analyses suggest that our chemogenetic manipulations produce a general decrease in excitatory firing.

To probe whether acute chemogenetic inhibition of the PFC would produce rsfMRI overconnectivity as observed with Kir2.1, we next compared rsfMRI connectivity patterns in hM4Di transduced and control mice upon acute CNO administration (active phase, Fig. 3.6). Recapitulating the results of chronic PFC inhibition, voxel-wise mapping revealed foci of significantly increased rsfMRI connectivity in the posterior cingulate/retrosplenial cortices and midline thalamic regions of DREADD-expressing mice (t test, $p < 0.05$, $t > 2.03$, FWE cluster-corrected, $p < 0.05$; Fig. 3.6a). Regional quantifications corroborated the presence of rsfMRI overconnectivity along the cingulate and retrosplenial axis of the DMN, and between the PFC and medio-dorsal thalamic areas (two-way repeated measures ANOVA, $F_{1,32} = 6.58$; $p = 0.0155$; t test $t_{32} = 4.30$, $p = 0.001$, respectively; Fig. 3.6b-c), a set of regions characterized by dense incoming projections from the PFC (Fig. 3.7, Wilcoxon rank-sum test, $p<0.0001$). Notably, the direction and the anatomical location of the observed rsfMRI overconnectivity was regionally unaltered by global fMRI signal regression (Figure 3.4), arguing against an unspecific contribution of arousal related global dynamics or global fMRI co-activation to the mapped changes (Gutierrez-Barragan et al., 2019; Turchi et al., 2018).

Baseline PFC connectivity in these areas was comparable across groups (voxel-wise mapping, $Z>2.03$ cluster corrected, PFC-Cingulate, two-way ANOVA, $F_{1,32} = 0.48$, $p = 0.49$, Thalamo-PFC, t test, $t_{32} = 0.23$, $p = 0.81$), and overconnectivity gradually emerged in the hM4Di cohort after CNO administration, peaking during the DREADD active time-window (PFC-Rs: $T_{32} = 2.158$, $p = 0.03$, PFC-Th: $T_{32} = 4.301$, $p = 0.0001$, t test, Fig. 3.6d). Moreover, no intergroup differences were observed in the estimated characteristic hemodynamic response function in this area (kernel height $p > 0.6$; time-to-peak $p > 0.12$, full-width-at-half-peak $p > 0.37$, t test) nor were between-group differences in arterial blood pressure ($p > 0.7$, t test) or blood gas levels observed ($PaCO_2$ $p = 0.49$; PaO_2 $p = 0.22$, t test). These control measurements rule out major spurious vascular or hemodynamic contributions

and corroborate the specificity of the mapped changes. Importantly, a replication of our chemo-fMRI study in a new set of animals imaged using a combination of medetomidine and low-dose isoflurane (Grandjean et al., 2020; Lee et al., 2021) revealed increased rsfMRI coupling between PFC and thalamic and retrosplenial areas (Fig. 3.8), recapitulating our findings in halothane-anesthetized mice. This result suggests that the observed overconnectivity does not reflect pharmacological interaction of DREADDs with the specific anesthetic used, but represents a more general phenomenon that extends to other sedatives and anesthetic condition. More broadly, our chemo-fMRI results show that acute inactivation of PFC activity results in a pattern of DMN overconnectivity closely recapitulating that observed with chronic Kir2.1-mediated neural inhibition, suggesting that the ensuing overconnectivity is not manipulation-specific, nor the indirect consequence of homeostatic reactivity to protracted neural suppression.

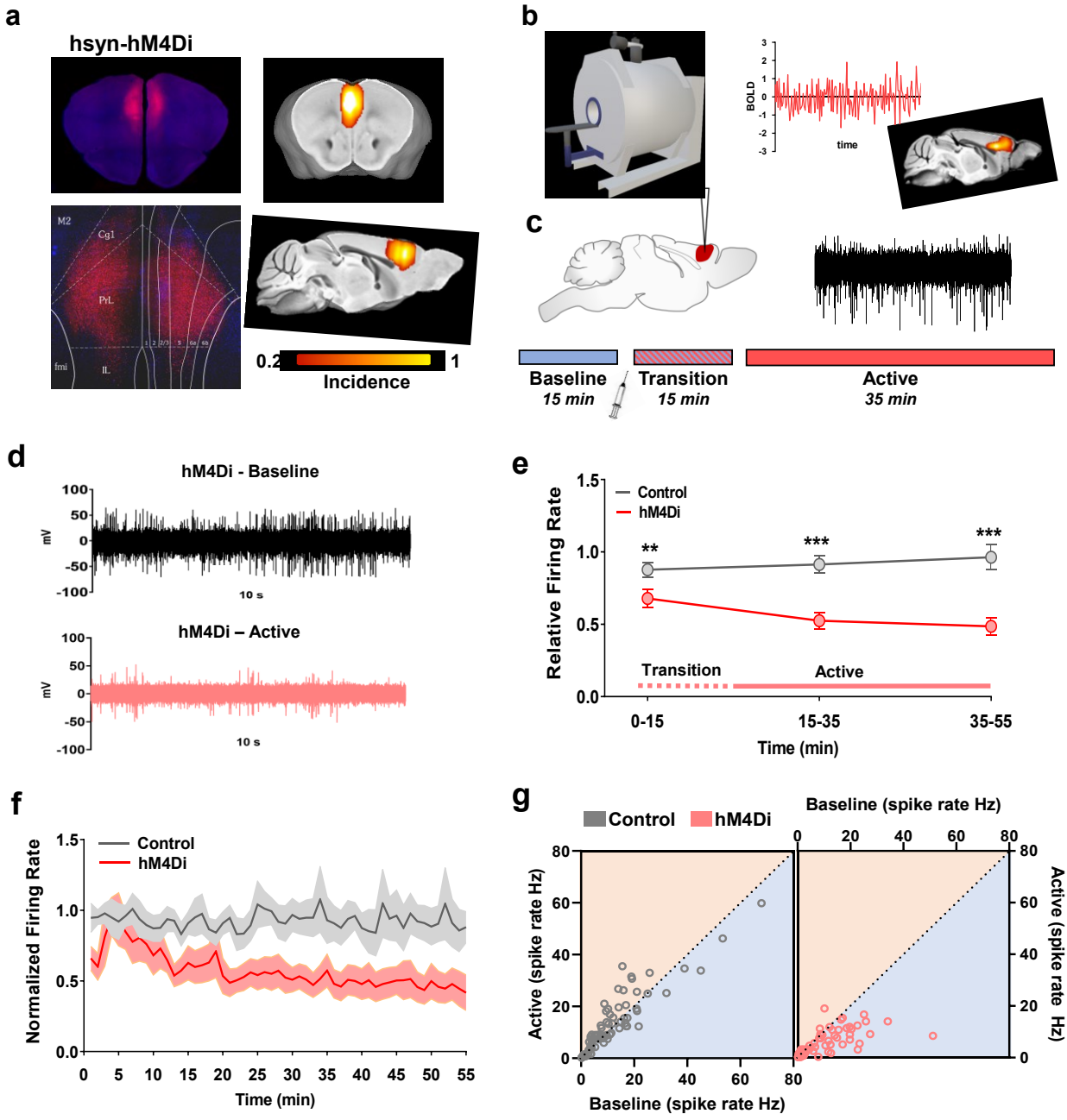

Figure 3.5 Chemogenetic inhibition of neural firing in the PFC ***(a)*** *Experimental design of chemo-fMRI experiments. AAV8-hSyn-hM4Di (n = 15) or AAV8-hSyn-GFP (control, n = 19) were bilaterally injected into the PFC of wild type. Left: Representative histology sample shown hM4Di (red) expression. Right: Heatmaps illustrate a qualitative regional assessment of viral expression across subjects.* ***(b)*** *Mice underwent chemo-fMRI scanning or* ***(c)*** *electrophysiological recordings to probe effectiveness of chemogenetic manipulations. A reference acquisition timeline is reported to depict timeseries binning into a 15 min pre-CNO reference baseline, a drug equilibration window (15 min, transition), and a 35 min CNO active time window (active).* ***(d)*** *Representative raw traces collected before and after CNO injection in representative recordings site of a hM4Di-expressing mouse.* ***(e-f)*** *Reduced firing rate in hM4Di-expressing mice (n = 5) compared to GFP-transduced controls (n = 5, two-sided Wilcoxon rank-sum tests, FDR corrected **q < 0.01, ***q < 0.001,). Data are presented as mean values ± SEM.* ***(g)*** *Scatterplot comparing the firing rate of individual PFC recording channels during baseline conditions (x axis) and the active phase (y axis) in control and DREADD-expressing animals (two-sided Wilcoxon rank-sum test FDR corrected, **q<0.01, ***q<0.001).*

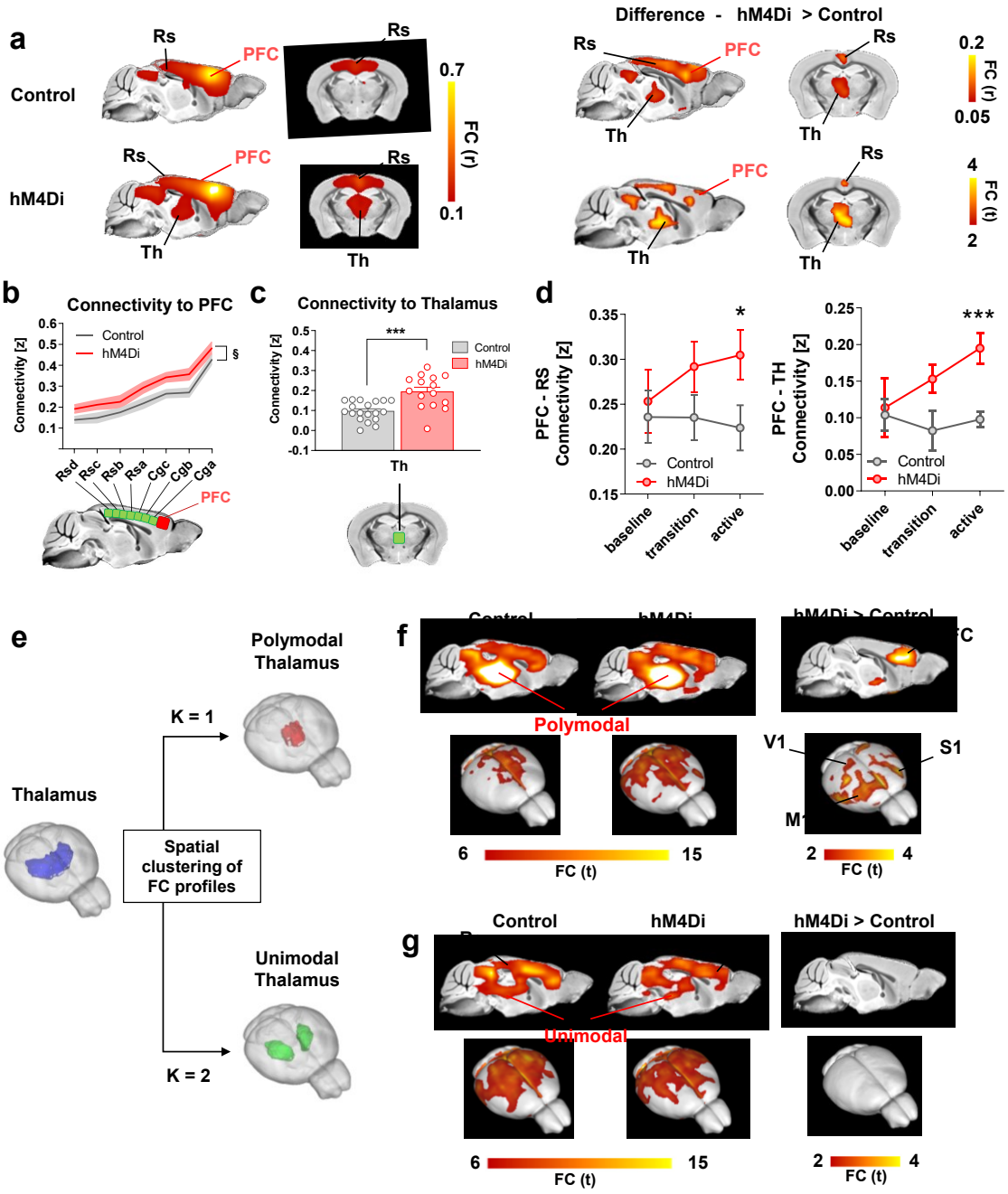

Figure 3.6 Chemogenetic inhibition of the mouse PFC results in rsfMRI overconnectivity ***(a)*** *Seed-based connectivity of the PFC and between group difference map revealed rsfMRI over-connectivity in the DMN of hM4Di expressing mice during the active phase.* ***(b)*** *Antero-posterior profiling of rsfMRI connectivity of the PFC along the midline axis of the mouse DMN in the two cohorts (§ p = 0.106, two-way ANOVA repeated measurements, genotype effect, n = 15 and n =19 control or hM4Di-expressing animals, respectively).* ***(c)*** *Thalamo-cortical rsfMRI hyper synchronization in hM4Di expressing mice and* ***(d)*** *prefrontal-retrosplenial and prefrontal-thalamic connectivity timecourse (*p = 0.039, ***p < 0.001, two-sided t test, n = 15 and n = 19 hM4Di or GFP-expressing mice, respectively.) Data in (b), (c) and (d) are presented as mean values ± SEM. (e) k-means clustering of PFC-thalamic rsfMRI connectivity profiles (thalamus, blue; polymodal thalamus, red; unimodal thalamus, green) in Control (n= 19) and hM4Di (n= 15) animals.* ***(f-g)*** *Seed connectivity of sub-thalamic partitions (f, polymodal thalamus; g, unimodal thalamus) and corresponding between group*

difference maps. FC: functional connectivity; Cg: cingulate cortex; M1: motor cortex; S1: Sensory cortex; PFC: prefrontal cortex, RS: retrosplenial cortex; Th: Thalamus; V1: visual cortex.

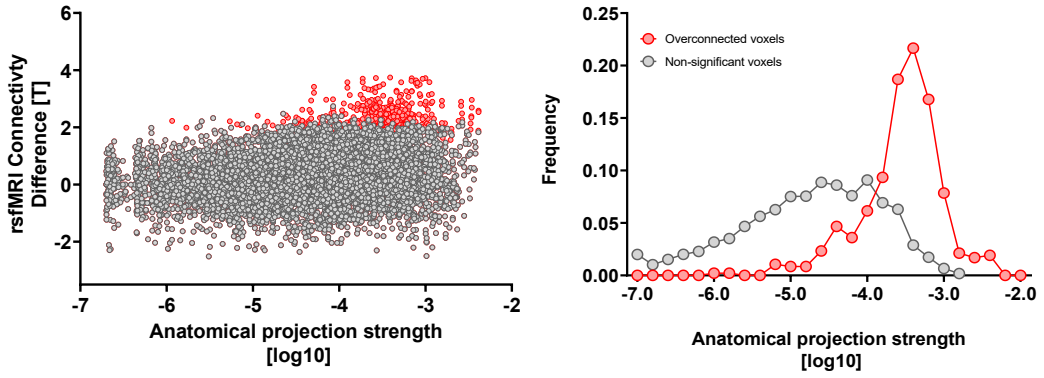

Figure 3.7 Voxels exhibiting rsfMRI overconnectivity upon chemogenetic inhibition of the PFC are robustly innervated by the PFC. *Left: scatter plot illustrating intergroup differences in rsfMRI connectivity as a function of PFC structural connectivity strength. Note that all significantly overconnected voxels (red) contain robust axonal projections from the PFC. Right: distribution of voxels exhibiting the most significant rsfMRI connectivity (red) and those that are not affected (grey).*

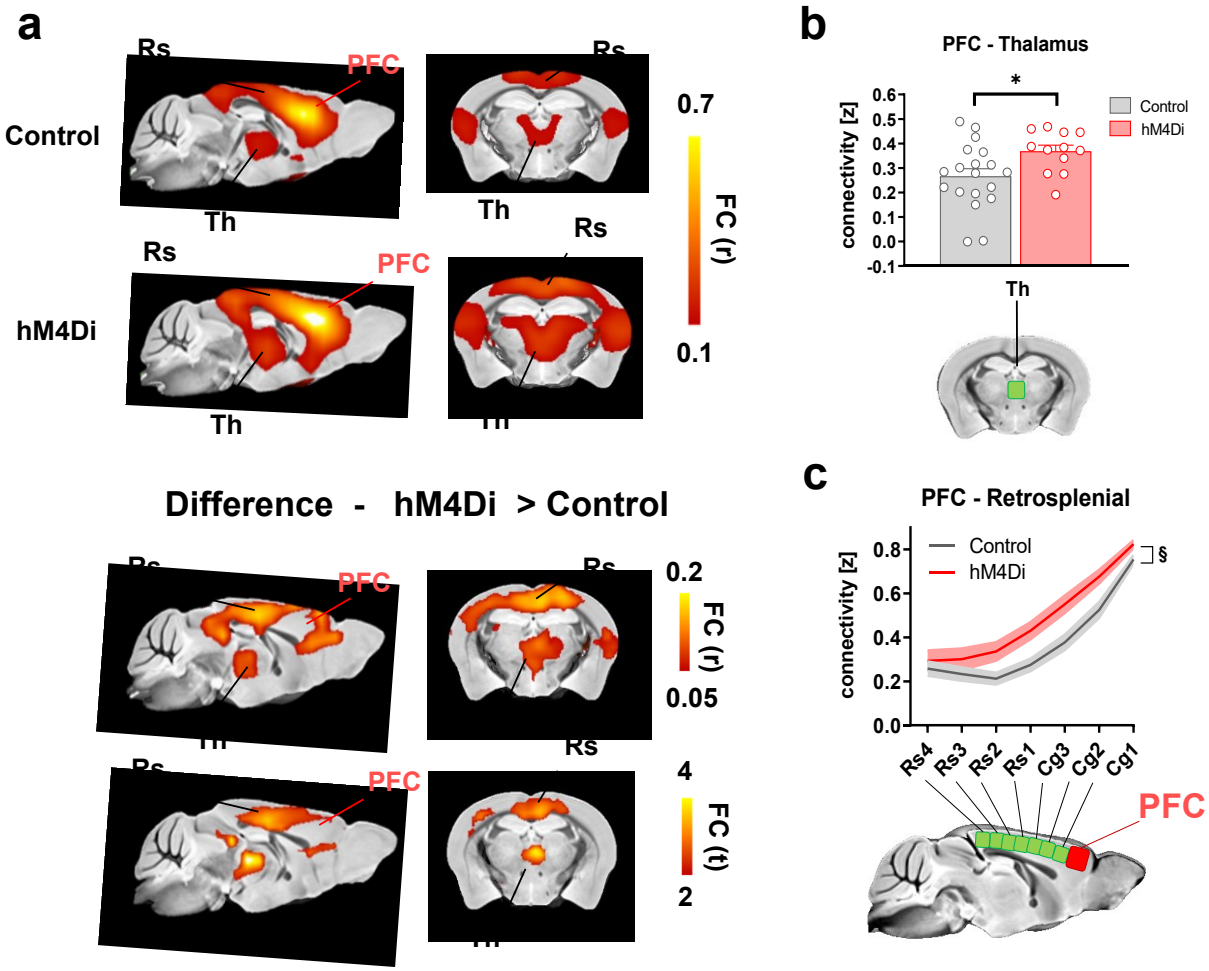

Figure 3.8 Chemogenetic inhibition of the mouse PFC under medetomidine-isoflurane anesthesia recapitulates the rsfMRI overconnectivity profile observed in halothane-anesthetized mice. (a) *Seed-based connectivity of the PFC in control (hSyn-GFP n = 19) and experimental (hSyn-hM4Di, n = 12, top) animals (top) and corresponding between-group connectivity difference map (Pearson's r, and T stat, respectively, bottom).* ***(b)*** *Thalamo-cortical rsfMRI overconnectivity in hM4Di expressing mice (*p = 0.03, two-sided t test, n = 12 and n = 19 hM4Di or GFP-expressing mice, respectively).* ***(c)*** *Antero-posterior profiling of rsfMRI connectivity of the PFC along the midline axis of the DMN in the two cohorts (§ p = 0.012, 2-way ANOVA repeated measurements, genotype effect, n = 12 and n = 19 hM4Di or GFP-expressing mice, respectively). Data in (b) and (c) are presented as mean values ± SEM. Cg: cingulate cortex; PFC: prefrontal cortex, RS: retrosplenial cortex; Th: Thalamus; FC: functional connectivity.*

3.3.3 Chemogenetic inhibition of the prefrontal cortex leads to thalamo-cortical rsfMRI overconnectivity

Topographical mapping of rsfMRI connectivity upon chemogenetic inhibition of the PFC revealed foci of overconnectivity in polymodal medio-dorsal and centro-medial areas of the thalamus, a set of higher order nuclei densely innervated by the mouse PFC (Mitchell, 2015). We thus probed the rsfMRI connectivity of the thalamus to assess whether the observed foci of thalamic overconnectivity could underlie or involve the engagement of additional brain regions outside the DMN. To obtain a regionally unbiased identification of polymodal (i.e. densely-PFC projecting) versus more unimodal lateral portions of the thalamus, we used k-means clustering to partition thalamic voxels based on their whole-brain rsfMRI connectivity profile, as previously described (Schleifer et al., 2019). Consistent with the neuroanatomical organization of this region, our approach revealed two segregable thalamic sub-territories, one encompassing its centromedial and anterodorsal (PFC-innervated) polymodal components, and the second encompassing more lateral (unimodal/sensory) areas (Fig. 3.6e). This anatomical segregation is also of potential mechanistic interest, as polymodal thalamic areas have been recently shown to serve as key generators and cortical propagators of slow neural rhythms (e.g. δ) relevant to rsfMRI coupling (Gent et al., 2018; He et al., 2008; Hughes et al., 2011; Nir et al., 2008).

Interestingly, seed-based probing of the unimodal thalamus did not reveal significant rsfMRI connectivity differences between hM4Di-expressing and control animals (Fig. 3.6g), whereas seed-based probing of the polymodal thalamus revealed in hM4Di expressing-mice a widespread pattern of cortical overconnectivity, exceeding the boundaries of the PFC to encompass motor and somatosensory territories, including the retrosplenial cortex (Fig. 3.6f, t test, $p < 0.05$, $t > 2.03$, FWE cluster-corrected, $p < 0.05$, Fig. 3.9). To probe the network specificity of these effects, we next

mapped whole-brain rsfMRI connectivity in hM4Di and control animals using a whole-brain parcellation scheme (Fig. 3.10). This analysis revealed the presence of significant clusters of rsfMRI overconnectivity only in regions of the DMN and in polymodal thalamic areas of DREADD-expressing animals, the latter areas exhibiting overconnectivity with larger cortical regions. No meaningful clusters of rsfMRI over- or under-connectivity were otherwise observed in any of the areas probed. These results show that, upon acute suppression of fronto-cortical activity, PFC-innervated polymodal thalamic regions, but not unimodal areas, exhibit over-synchronous rsfMRI coupling with large cortical areas.

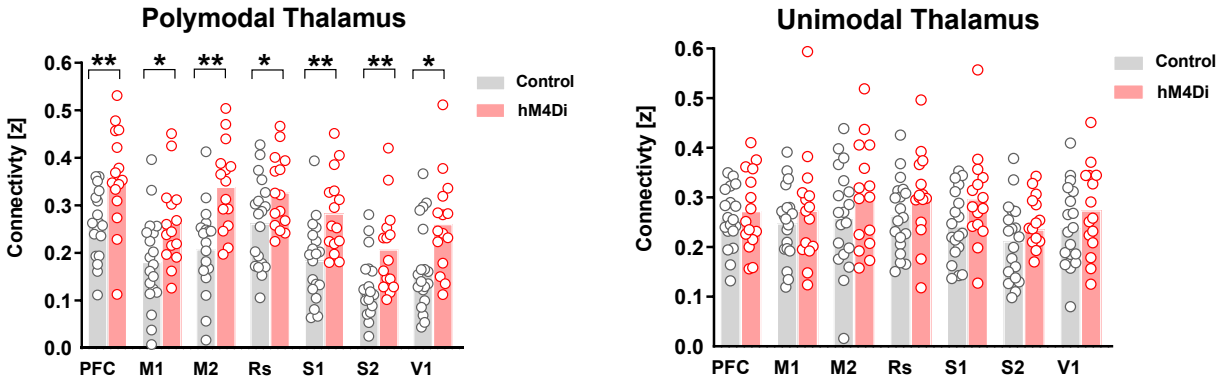

Figure 3.9 The polymodal thalamus is functionally overconnected to cortical areas. *Quantification of thalamo-cortical connectivity extracted from polymodal (left) and unimodal (right) thalamic partitions (*q<0.05, **q<0.01, two-sided t test, FDR corrected, n = 15 and n = 19 hM4Di or GFP-expressing mice, respectively). Source data are provided as a Source Data file. M1: primary motor cortex; M2: secondary motor cortex; S1: primary somatosensory cortex; S1: secondary somatosensory cortex; PFC: prefrontal cortex, RS: retrosplenial cortex; V1: primary visual cortex.*

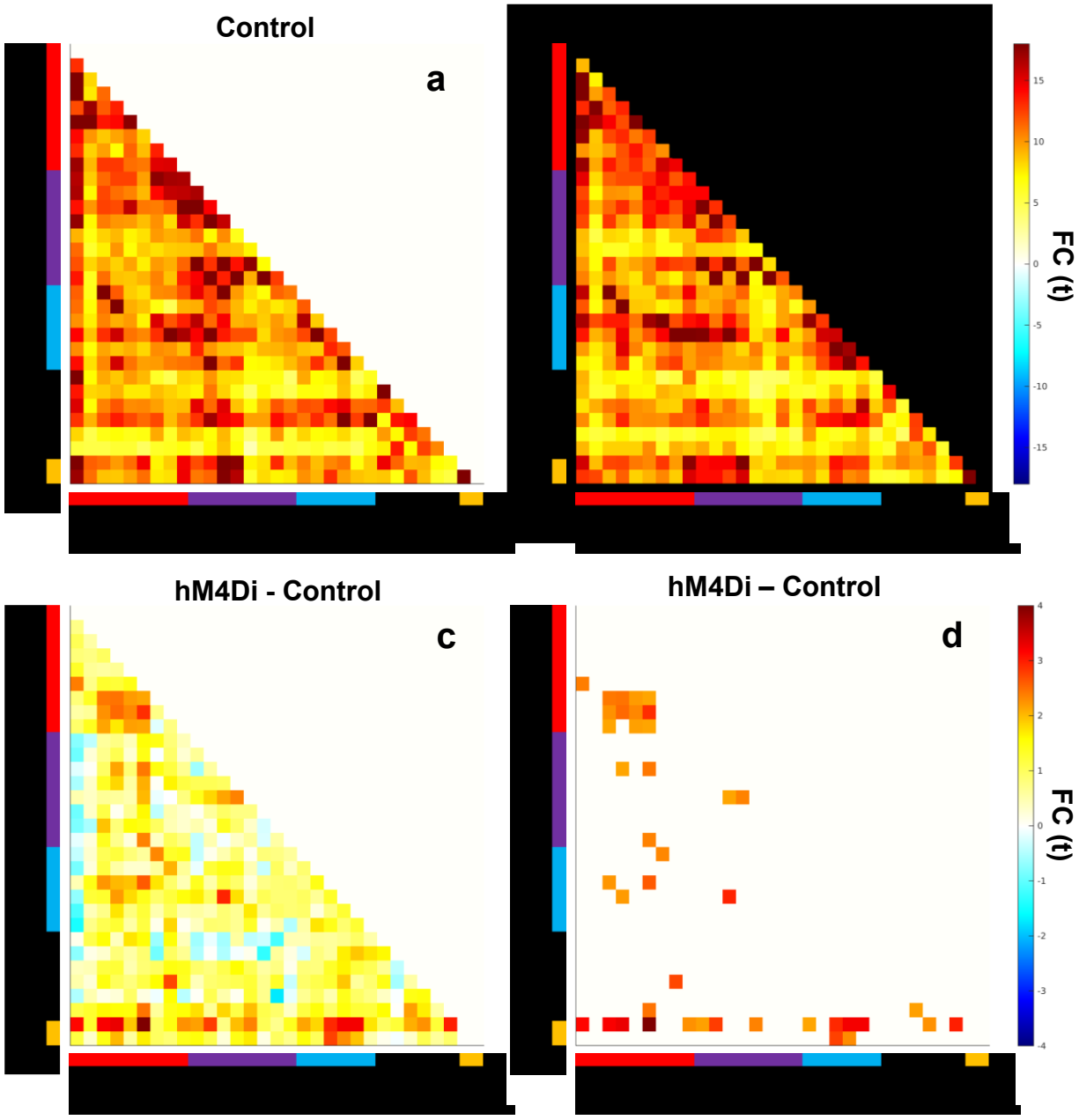

Figure 3.10 Whole-brain rsfMRI connectivity in control and hM4Di-expressing mice. *Correlation matrices in* ***(a)*** *and* ***(b)*** *depict inter-areal connectivity in control and hM4Di mice respectively.* ***(c)*** *Mean difference map (t), and* ***(d)*** *regions exhibiting connectivity differences larger than |t|> 2.1, corresponding to p < 0.05, two-tailed t test (uncorrected). TH: thalamus; STR: striatum; LCN: lateral cortical network; HCP: hippocampus; DMN: default mode network; FC: functional connectivity.*

3.3.4 Chemogenetic inactivation of the prefrontal cortex inhibits firing not locked to slow rhythms, resulting in increased slow oscillatory power

To obtain insight into the neural rhythms underlying the observed rsfMRI overconnectivity, we next analyzed local field potential (LFP) traces obtained from the same set of PFC electrophysiological recordings analyzed in Fig. 3.5. Consistent with the observed firing rate reduction, LFP spectrograms

from hM4Di-transduced animals revealed an overall shift of LFP power towards lower frequencies, with a robust decrease in β- and γ-band power after CNO administration with respect to CNO treated controls ($F_{1,22} = 239.4$, $p < 0.1$ and $p<0.001$, respectively, Fig. 3.11a-b). Notably, the LFP power reduction in these frequency bands was also accompanied by a prominent increase in δ and slow-band (defined here as 0.1 – 1 Hz) LFP power in DREADD-expressing subjects (Fig. 3.11b, slow $p < 0.001$, δ $p < 0.01$, θ $p = 0.77$; α $p = 0.34$; β $p = 0.01$; γ $p<0.001$; Wilcoxon rank-sum tests, FDR corrected). Given that higher LFP frequencies typically reflect local neural interactions, while lower LFP frequencies are instead associated with larger scale phenomena (Einevoll et al., 2013; Logothetis, 2008) these results suggest that chemogenetic inhibition of PFC suppresses local, rather than global, neural processes.

To investigate the relationship between DREADD-induced reduction in firing and the concomitant increase in local slow and δ oscillatory power, we next performed phase locking analyses of MUA firing in the PFC. Interestingly, our investigations revealed that in DREADD-expressing animals, the fewer residual spikes recorded after CNO injection exhibited strong phase locking to ongoing slow and δ LFP oscillations. Such strong phase locking was not observed in control animals or in baseline recordings, where spike distributions were instead more equally spread across δ and slow oscillation phases (Fig. 3.11c-e). These observations suggest that chemogenetic inhibition of the PFC leads to a selective reduction of firing not locked to ongoing slow rhythms, resulting in a concomitant increased phase locking of residual firing to high-excitability phases of ongoing low frequency oscillations. The resulting spiking activity is therefore on average greatly reduced, but also considerably more periodic and phase-locked to underlying low frequency oscillatory rhythms.

To better illustrate the relationship between increased oscillation power and enhanced spike locking in the slow and δ bands, we performed a simple simulation. Specifically, we first simulated spike trains to have weak phase locking to a slow rhythm, with spikes happening almost equally across phase angles of the oscillatory cycle as observed in control conditions. To mimic DREADD-induced effects, we next selectively removed spikes emitted at the non-preferred phases of slow oscillatory activity as observed in our recordings. To mimic DREADD-induced effects, we next selectively removed spikes emitted at the non-preferred phases of slow oscillatory activity as observed in our recordings. In keeping with our experimental results, this simple simulation showed that the removal of “asynchronous" off-preferred-phase firing reduces power of high frequency spiking activity, while simultaneously increasing the power of the low-frequency rhythm residual spikes are entrained to

(Fig. 3.12). This suggests that DREADD-induced increase in slow LFP power does not necessarily reflect the generation of a new, “artificial” rhythm, but can be simply explained by the emergence of increased phase locking to existing slow oscillatory activity.

Finally, to further probe the mechanistic specificity of our findings, we measured rsfMRI connectivity profiles produced by cell-type specific manipulations designed to increase local PFC firing. We found that chemogenetic inhibition of fast-spiking Parvalbumin (PV) GABAergic cells or hM3Dq-based excitation of pyramidal (CamkII-expressing) neurons both produced PFC underconnectivity with cortical terminals of the DMN (Fig. 3.13). Notably, both manipulations produced neural signatures characterized by increased local firing rate and a robust shift of LFP power towards higher frequencies, effectively reversing the corresponding electrophysiological signature observed in our DREADD inhibition studies (Fig. 3.11). These effects were far more prominent in mice undergoing DREADD-based stimulation of pyramidal neurons, a manipulation that was also associated with largely suppressed slow and δ-band LFP activity. Taken together, these new investigations suggest that the observed functional overconnectivity does not reflect an increased excitatory/inhibitory ratio in the PFC, or an unspecific functional inhibition of GABAergic neurons.

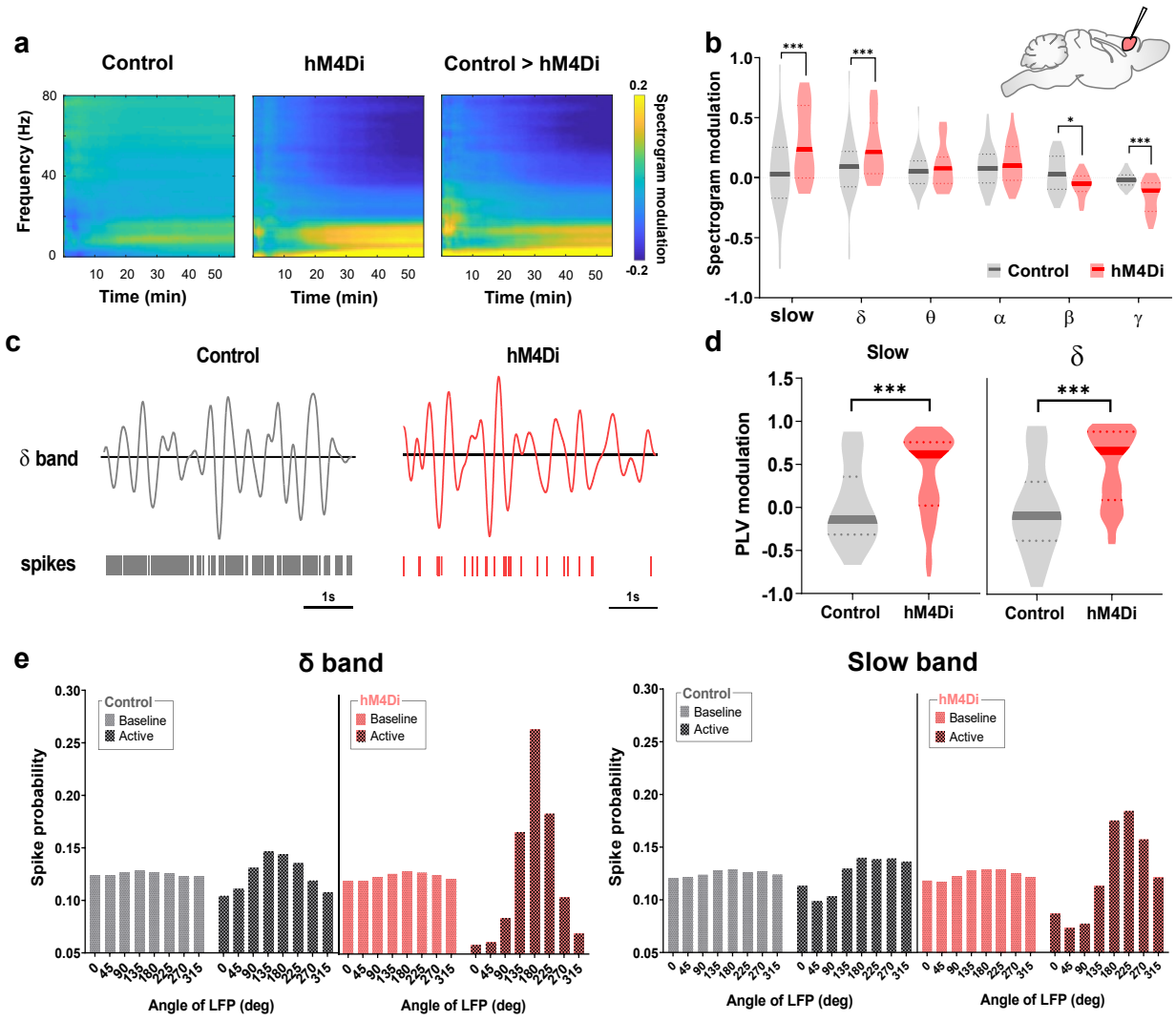

Figure 3.11 Chemogenetic inhibition of the PFC reduces γ activity but increases slow oscillatory power ***(a)*** *Mean post-injection spectrogram in control (Left), hM4Di-expressing animals (center), and mean between group difference (right).* ***(b)*** *Quantification of band-specific power spectrum changes upon CNO injection in both groups (*q <0.05, ***q<0.001, two-sided Wilcoxon rank-sum tests followed by FDR correction, for n = 50 and n = 60 statistically independent recordings from n = 5 hM4Di and n = 5 control mice, respectively).* ***(c)*** *Example traces of bandpassed δ-band LFPs and corresponding spiking activity (right) from a representative PFC recording channel during active phase in control and DREADD-expressing mice. Note the presence of greatly reduced, but more phase-locked firing in animals expressing hM4Di channel.* ***(d)*** *Violin plots depicting PLV of PFC spikes to slow and δ bands (***q<0.001, two-sided Wilcoxon rank-sum tests followed by FDR correction for n = 79 and n = 80 statistically independent recordings from n = 5 hM4Di and n = 5 control mice, respectively). (e) Probability of firing (all sessions and datapoints) as a function of the phase angle of δ (bottom) and slow (top) bands. Phase conventions are such that 0 and 180 deg represent the peak and through of LFP, respectively. (Violin plots: thick lines represent median, dashed lines indicate 25th and 75th percentile, respectively). PLV: phase locking value.*

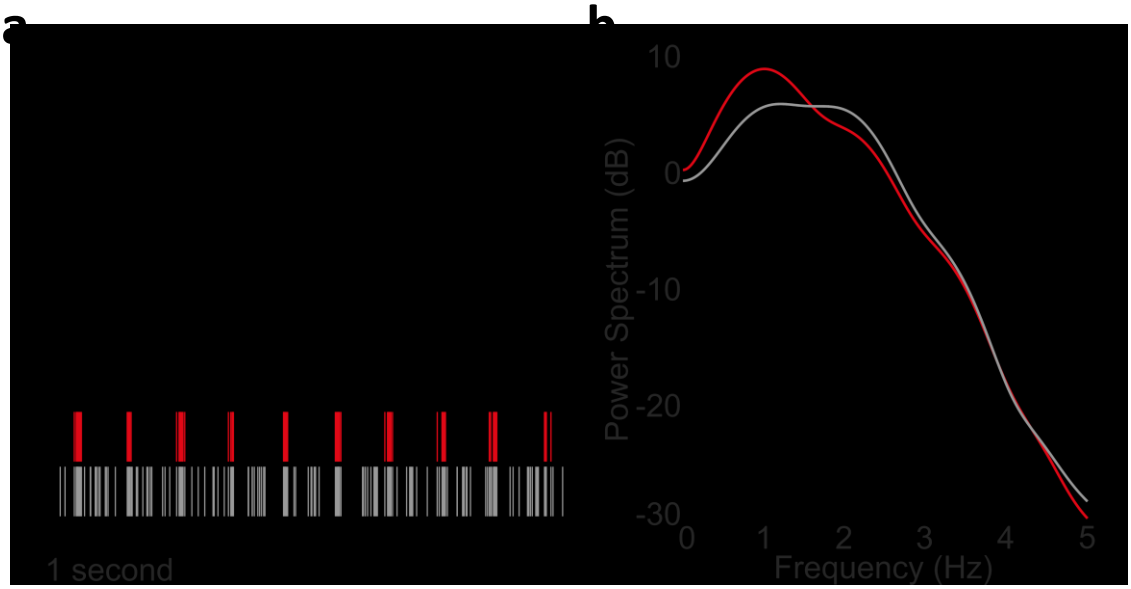

*Figure 3.12 A simple simulation of the effect of suppressing neural firing not locked to slow rhythms. **(a)** Top (black line): 1 Hz simulated sinusoidal "LFP" wave to which spikes trains are locked. Middle (red lines): spike trains strongly locked to the LFP wave, conceptualizing firing during DREADD-induced manipulation. Bottom (red lines): spike trains obtained from the red ones but adding also an equal number of unlocked spikes, conceptualizing firing during control conditions. **(b)** Power spectra of the resulting spike trains.*

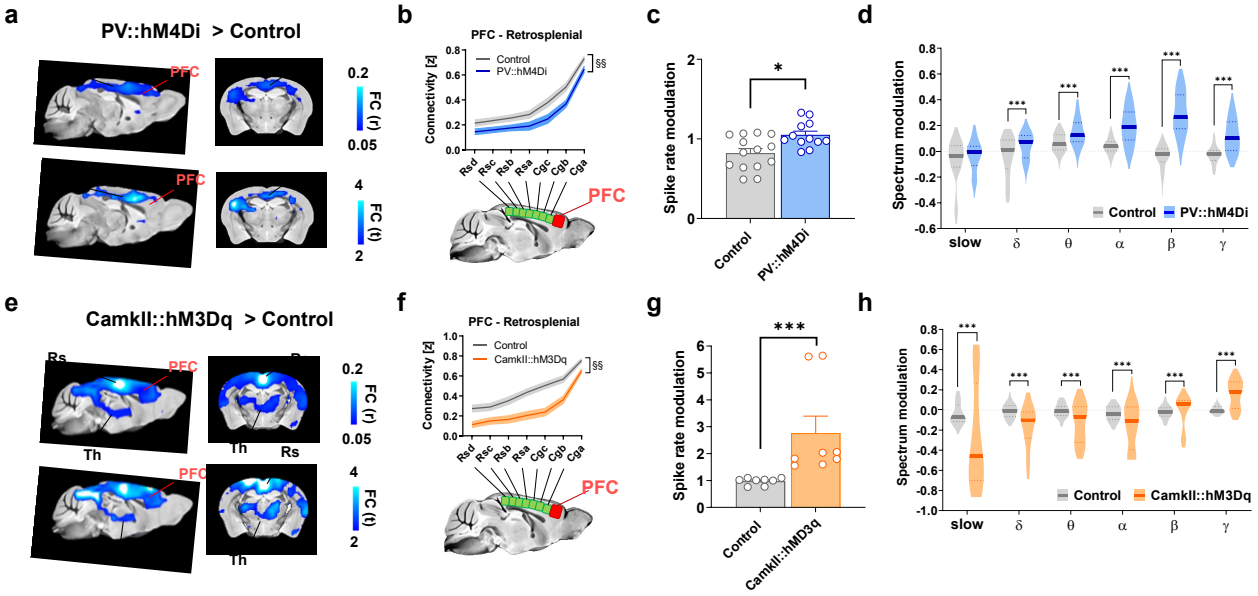

*Figure 3.13 Chemogenetic inhibition of parvalbumin GABAergic cells (a-d) and stimulation of pyramidal neurons (e-h) produce rsfMRI underconnectivity. **(a)** Between group PFC seed-based connectivity difference maps revealed rsfMRI underconnectivity (blue) in the DMN of PV::hM4Di expressing mice during the active CNO phase. PV::Cre mice were bilaterally injected with hSyn-DIO-hM4Di (n = 16). Control PV::Cre animals underwent sham injections (control, n = 17). **(b)** Antero-posterior profiling of rsfMRI connectivity of the PFC along the midline axis of the mouse DMN (§§ p = 0.008, 2-way ANOVA repeated measurements, genotype effect, PV::hM4Di n = 16, sham n = 17). **(c)** Increased firing rate in PV::hM4Di mice upon CNO injection (two-sided Wilcoxon rank-sum test, p = 0.019, n = 12 and n = 14 statistically independent recordings in n = 6 PV::hM4Di*

and n = 7 control mice, respectively). ***(d)*** *Quantification of the corresponding band-specific power spectrum changes in the PFC (***q < 0.001, two-sided Wilcoxon rank-sum test followed by FDR correction, n = 120 and n = 140 statistically independent recordings in n = 6 PV::hM4Di and n = 7 control mice, respectively).* ***(e)*** *Between group PFC seed-based connectivity difference map in mice expressing CamkII::hM3Dq (n = 20), or CamkII::cre mice subjected to sham viral injections (control, n = 17) during the CNO active phase. This analysis revealed the presence of robust rsfMRI underconnectivity (blue) in the DMN.* ***(f)*** *Antero-posterior profiling of rsfMRI connectivity of the PFC along the midline axis of the mouse DMN in the two cohorts (§§ p < 0.001, 2-way ANOVA repeated measurements, genotype effect, CamkII::hM3Dq n = 20, sham n = 17).* ***(g)*** *Largely increased firing rate in hM3Dq-expressing mice compared to controls (*** p < 0.001, two-sided Wilcoxon rank-sum test, n = 8 and n = 8 statistically independent recordings in n = 4 CamkII::hM3Dq and n = 4 sham mice, respectively).* ***(h)*** *Quantification of corresponding band-specific power spectrum changes upon CNO injection (*** q < 0.001, two-sided Wilcoxon rank-sum test followed by FDR correction, n = 80 statistically independent recordings in n = 4 CamkII::hM3Dq and n = 4 control mice, respectively). Data in barplots (c) and (g) are presented as mean values ± SEM. Violin plots: thick lines represent median, dashed lines indicate 25th and 75th percentile, respectively. Cg: cingulate cortex; PFC: prefrontal cortex, RS: retrosplenial cortex; Th: Thalamus; FC: functional connectivity.*

3.3.5 Chemogenetic inhibition of the prefrontal cortex increases interareal slow oscillatory coherence

The increase in slow and δ band LFP power observed in the chemogenetically-inhibited PFC led us to hypothesize that the resulting rsfMRI overconnectivity could be driven by enhanced low-frequency neural coherence, as opposed to direct interareal communication via higher frequency neural oscillations (Besserve et al., 2015; Bosman et al., 2012; Van Kerkoerle et al., 2014). To test this hypothesis, we carried out a new set of simultaneous multi-electrode LFP recordings in the PFC, retrosplenial, and centromedial (polymodal) thalamus of control and DREADD- transduced animals (Fig. 3.14). We selected these region pairs because they exhibit the highest functional overconnectivity in our chemo-fMRI study. Spectral-power quantifications after CNO administration revealed a reduction of γ and β LFP power in all the three recording sites, together with increased slow and δ LFP power in the PFC, but not in the retrosplenial cortex or centromedial thalamus of DREADD-transduced animals (Fig. 3.15a).

To explore the possible neural correlates of fMRI connectivity in terms of frequency-dependent neural communication, we next computed LFP power coherence between electrophysiological signals recorded at these electrode pairs and probed the presence of increased coupling between the recording sites. Notably, we found a clear CNO-induced increase in low-frequency LFP power coherence in PFC-Rs and PFC-polymodal thalamic areas in hM4Di-transduced animals (Fig. 3.15b). In keeping with rsfMRI evidence of increased thalamo-cortical connectivity upon PFC inhibition, enhanced low-frequency power coherence was also observed between the thalamus and retrosplenial cortex (Fig. 3.15b). Quantification of these changes in canonical LFP frequency

bands revealed significantly increased power coherence in the slow and δ bands for all the three electrode pairs (Fig. 3.14a-c, $q < 0.05$, Wilcoxon rank-sum test, FDR corrected, all pairs). We next computed inter-areal coherence between the envelope of ϒ-band amplitude because ultra-slow (~0.1 Hz) variation in ϒ-band envelope has been linked to arteriole dynamics and suggested to be a contributing factor to rsfMRI coupling (Mateo et al., 2017; Nir et al., 2008). Mean coherence plots of ϒ-envelope over the ultra-slow frequency range (0.02-0.5 Hz (Mateo et al., 2017)) revealed only marginally increased CNO-induced coherence in hM4Di expressing mice (Fig. 3.15c). In keeping with this observation, we did not find evidence of significantly increased ultra-slow ϒ-envelope coherence (integrated between 0.02 to 0.5 Hz) between any electrode pairs ($q > 0.1$, Wilcoxon rank-sum test, FDR corrected).

To link these oscillatory changes to the observed rsfMRI patterns, following the procedure described in Wang et al. (2012), we next compared the obtained electrophysiological coherence values with corresponding (separately-measured) interareal rsfMRI connectivity in hM4Di and control animals (Fig. 3.14d-e). We first compared between-group band-specific LFP coherence differences across all electrode pairs with corresponding interareal rsfMRI connectivity changes measured during the active CNO phase (Fig. 3.14d). These quantifications revealed that δ and slow LFP bands were the only frequency ranges exhibiting CNO-induced increased coherence between PFC-retrosplenial and PFC-thalamic electrode pairs, in agreement with the corresponding CNO-induced interareal rsfMRI connectivity increases (Fig. 3.14d). While considerably smaller, between-group ultra-slow LFP gamma-envelope coherence also revealed CNO-induced increases in all the three electrode pairs (Fig. 3.14d). Other LFP bands did not show full concordance with rsfMRI findings: for example, β band coherence increased after CNO administration in PFC-retrosplenial but not in PFC-thalamus electrode pairs. Similarly, no meaningful between-group changes in power coherence upon DREADD stimulation was observed in the θ and γ LFP bands (Fig. 3.14d). Further supporting a key contribution of slow and δ rhythms to the observed rsfMRI overconnectivity, we found that pairwise LFP coherence difference across all the recorded sites in these two bands exhibited a linear relationship with corresponding group-level pair-wise rsfMRI connectivity measured in both DREADD and control animals during the CNO active window (Fig. 3.13e, δ $R2 = 0.92$, $p = 0.002$; slow $R2 = 0.73$, $p = 0.029$, uncorrected). Only δ LFP coupling however retained a significant correlation with rsfMRI connectivity upon FDR correction ($q=0.008$, FDR corrected). A much weaker correlation between band specific LFP coherence and pairwise rsfMRI connectivity was apparent for all the other bands (Fig. 3.14e, $p > 0.11$ all bands). These findings were paralleled by the

observation of similarly robust increased interareal δ- and slow-band LFP phase coherence, a widely used measure of functional synchronization in LFP/EEG studies (Bowyer, 2016) (Fig. 3.14f). Taken together, these results corroborate a neural origin for our imaging findings and implicate increased slow and δ LFP coherence as a plausible neural driver of the observed rsfMRI over-synchronization.

Our findings can be summarized in a simple illustrative scheme (Fig. 3.16) in which chemogenetic inhibition of the PFC (node A) reduces high-frequency local activity via a preferential suppression of spikes not locked to ongoing, global low frequency rhythms. This in turns produces a breakdown of high-frequency communication between the manipulated area and its targets (B and C). At the same time, the residual firing activity in the inhibited node becomes more entrained with ongoing low-frequency fluctuations, here depicted as a global slow rhythm. The observed functional overconnectivity may then reflect the resulting increase in interareal slow and δ LFP coherence, which we have empirically found, under our experimental conditions, to predict the direction and magnitude of rsfMRI coupling better than the coherence of faster rhythms. Importantly, this model is also broadly consistent with examinations of LFP signatures of directionality of interactions between areas (Fig. 3.17). Specifically, using phase-lag quantifications as a measure of information flow directionality, we found that in the δ band PFC activity preceded in phase retrosplenial cortex activity, a finding consistent with previous reports of antero-posteriorly travelling δ wave activity in the anesthetized mouse brain (Mitra et al., 2018). Consistent with our hypothesis, after CNO administration the phase difference between PFC and retrosplenial cortex in DREADD-expressing animals was greatly reduced, implying that chemogenetic suppressions of local high frequency results in more synchronous and less phase-lagged δ activity. This finding suggests that after chemogenetic inhibition, PFC activity becomes more entrained with global, slow covarying rhythms.

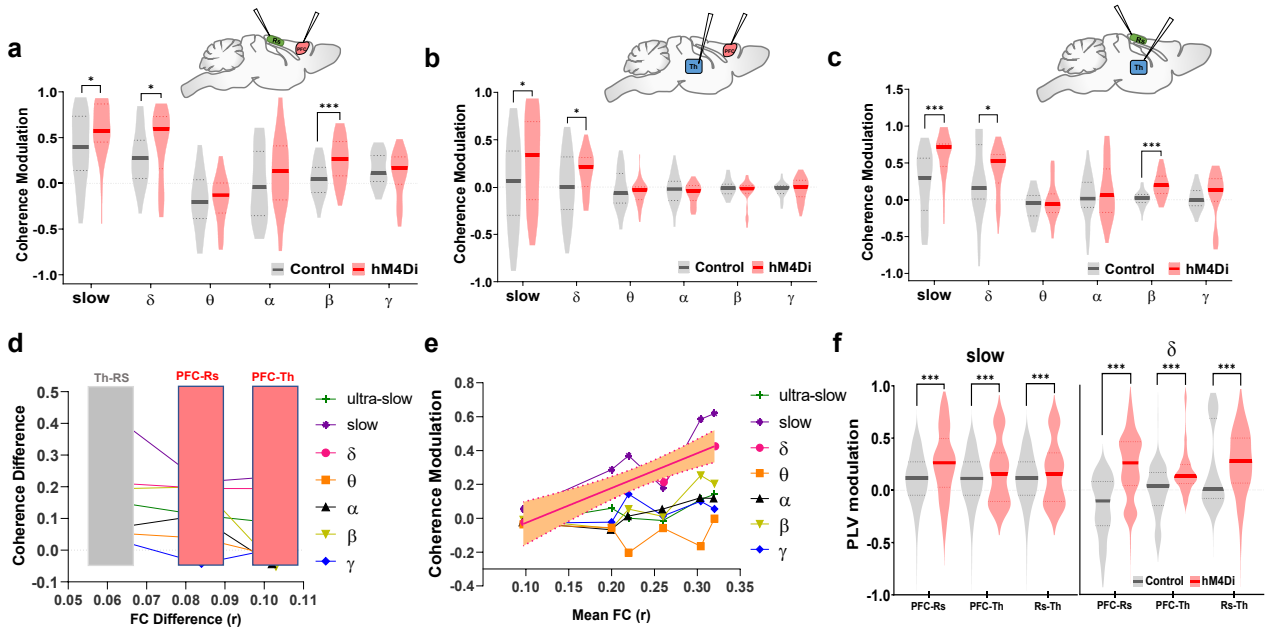

Figure 3.14 Chemogenetic inhibition of the PFC results in increased interareal slow oscillatory coherence. *Baseline normalized power coherence at different frequency bands for PFC-retrosplenial* ***(a),*** *PFC-thalamus* ***(b)*** *and retrosplenial-thalamus* ***(c)*** *electrode pairs (*q <0.05, ***q<0.001, one-sided Wilcoxon rank-sum test, FDR corrected for n = 50 and n = 40 statistically independent recordings from n = 5 hM4Di and n = 4 control mice, respectively).* ***(d)*** *Band specific coherence and mean functional connectivity (FC) difference (hM4Di – Control) for all pairs of electrophysiologically-probed regions. Mean FC data were extracted for corresponding regional pairs during the CNO active time window in hM4Di and control animals.* ***(e)*** *Correlation between corresponding band specific coherence and mean functional connectivity for all pairs of electrophysiologically-probed regions (PFC-Rs; PFC-Th; Rs-Th). Shaded area indicates 95% CI for δ.* ***(f)*** *Baseline normalized phase coherence in slow and delta band between electrode pairs (Violin plots: thick lines represent median, dashed lines indicate 25th and 75th percentile, respectively; ***q<0.001, two-sided Wilcoxon rank-sum tests, FDR corrected). PLV: phase locking value.*

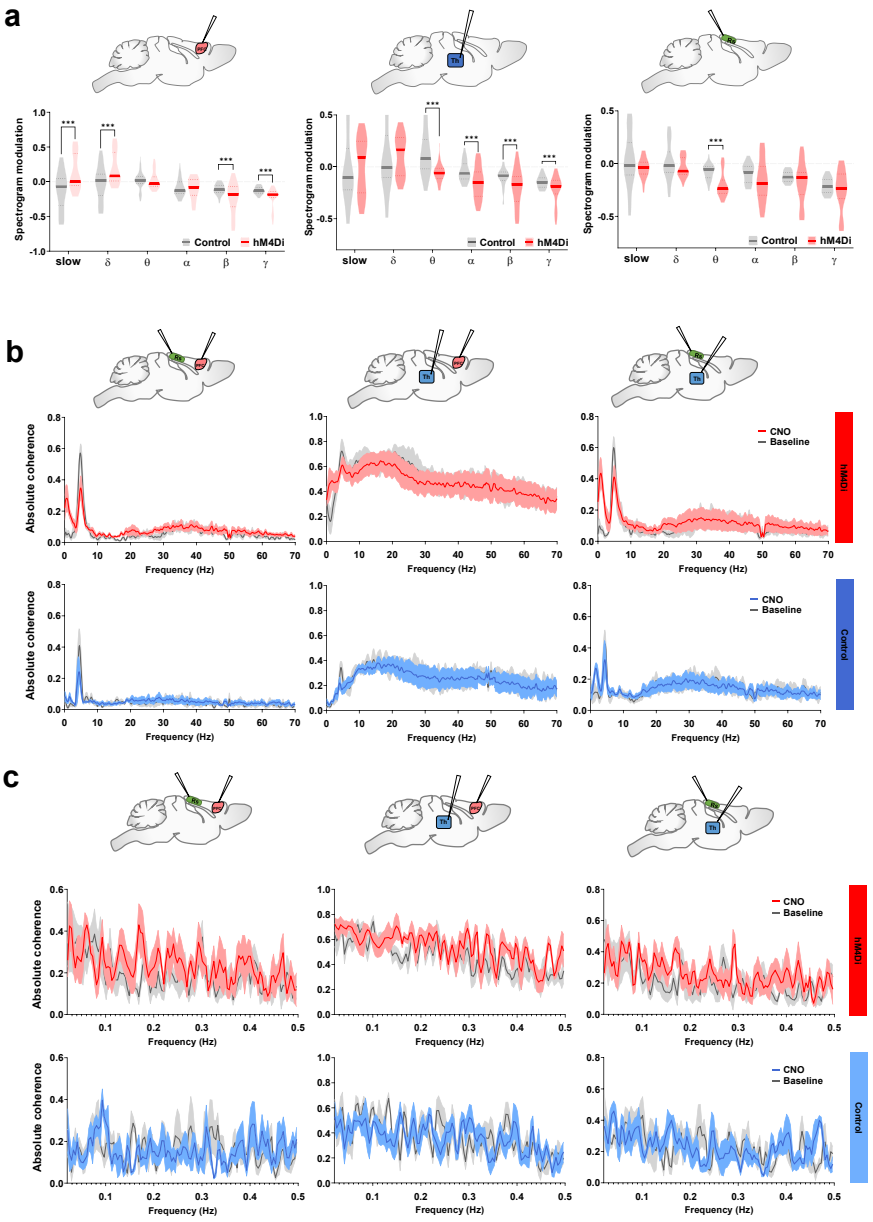

Figure 3.15 LFP power spectra and absolute coherence in multi-electrode recordings. ***(a)*** *Quantification of band-specific power spectrum changes in LFPs recorded in the PFC (left), centromedial thalamus (Th; center) and retrosplenial cortex (Rs; right) upon systemic CNO administration. Power was quantified with respect to pre-injection baseline (violin plots: thick lines represent median, dashed lines indicate 25th and 75th percentile, respectively; two-sided Wilcoxon rank-sum tests, followed by FDR correction, ***q<0.001, n = 50 and n = 40 statistically independent recordings in n = 5 hM4Di and n = 4 control mice, respectively).* ***(b)*** *Mean absolute power coherence for all pairs of electrophysiologically-probed regions (PFC-Rs; PFC-Th; Rs-Th) during both baseline and CNO active time window in hM4Di and control animals (mean ± SEM).* ***(c)*** *Mean absolute power coherence of ultra-slow oscillation for all pairs of electrophysiologically-probed regions (PFC-Rs; PFC-Th; Rs-Th) computed for both baseline and CNO active time window in hM4Di and control animals (mean ± SEM).*

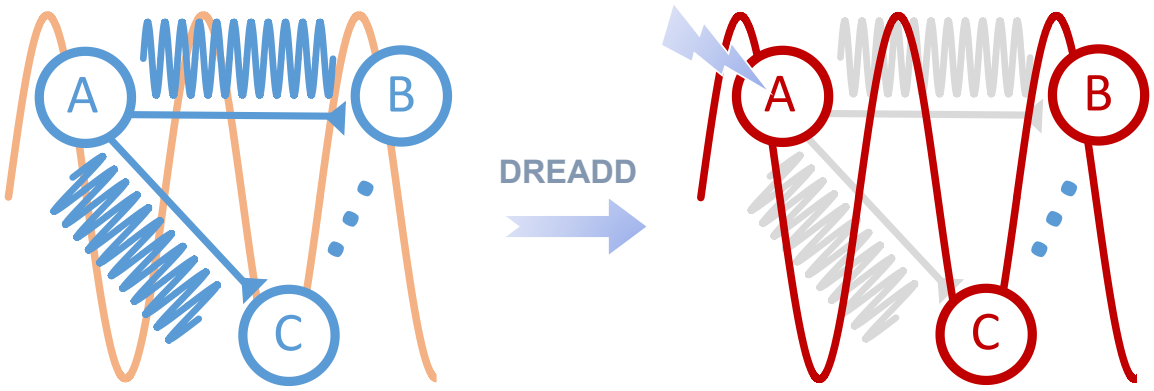

Figure 3.16 A schematic illustration of our findings. *Chemogenetically inhibiting neural activity in cortical node A (i.e. PFC) reduces high-frequency direct interactions between the manipulated region and its targets (B and C), concomitantly producing higher entrainment of residual spiking activity with ongoing global low-frequency oscillations (node C). Under the assumption (supported by our data) that rsfMRI interareal connectivity is primarily driven by low-frequency neural synchronization, this interpretative framework predicts both the observed increase in interareal slow and δ LFP coherence, and the corresponding increase in interareal rsfMRI connectivity.*

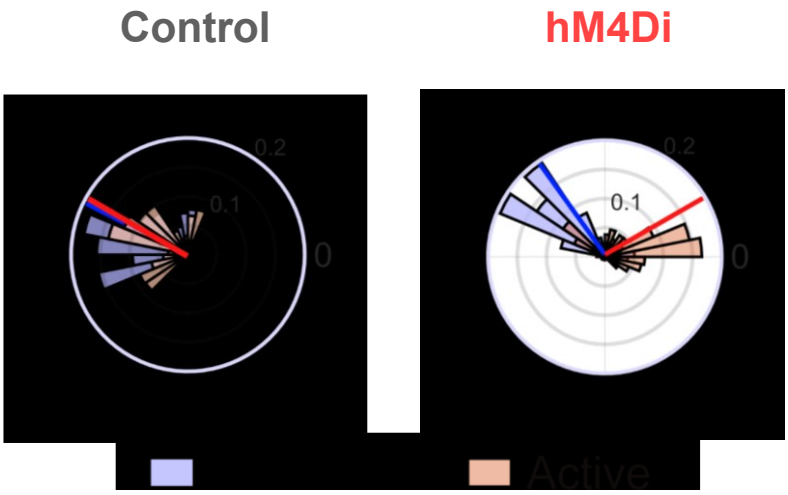

Figure 3.17 LFP δ-band phase difference between PFC and Rs cortices. *Distribution of the difference in average instantaneous phase between PFC and Rs recording channels, before (baseline) and after CNO-administration (active) in control and hM4Di-expressing animals. Thick lines indicate the circular average across channels of the phase difference for baseline (blue) and active (red) phase, respectively.*

3.4 Discussion

Here we combine neural perturbations and mouse rsfMRI to investigate how rsfMRI topography reconfigures in response to targeted cortical inactivation. We report that chronic and acute neural inactivation of the mouse PFC can counterintuitively increase rsfMRI connectivity with DMN targets directly innervated by the inhibited area. Electrophysiological investigations revealed that chemogenetic inactivation of the PFC preferentially and robustly suppresses the firing activity that is not phased locked to highly excitable peaks of ongoing slow-oscillatory rhythms, leading to increased slow and δ band power, and enhanced interareal low-frequency coherence. These observations argue against a neural-independent origin for the observed overconnectivity, and implicate low-frequency neural rhythms in the establishment of the observed rsfMRI overconnectivity.

While critically shaped and constrained by underlying axonal connectivity (Coletta et al., 2020; Hagmann et al., 2008; Z. Wang et al., 2013), spatiotemporal correlations in spontaneous rsfMRI activity can dynamically reconfigure in response to local perturbations. In-depth investigations of the reconfiguration patterns resulting from regional suppression of neural activity are of special interest. These allow for a targeted deconstruction of rsfMRI coupling and may offer opportunities to mechanistically interpret aberrant rsfMRI connectivity patterns in neurological conditions characterized by loss of cortical function (Alstott et al., 2009; Friston & Büchel, 2004; Grayson et al., 2016). Leveraging the recent implementations of chemo-fMRI in the mouse (Giorgi et al., 2017), we causally probed how neural suppression of cortical activity affects brain-wide rsfMRI coupling. In contrast to theoretical (Alstott et al., 2009) and experimental (Grayson et al., 2016) evidence predicting that regional inactivation of a neural node would result in reduced functional synchronization with its direct anatomical targets, we found that both chronic and acute inhibition of the PFC can counterintuitively increase rsfMRI connectivity within thalamo-cortical substrates of the mouse DMN.

Our results advance our understanding of the principles underlying brain-wide rsfMRI coupling in two directions. First, we provide causal evidence that regional suppressions of brain activity does not necessarily lead to reduced neural and functional coupling between the inactivated area and its direct anatomical projection targets, but can result in increased rsfMRI connectivity via enhanced, less-localized slow oscillatory coherence. These observations point at a highly dynamic and non-monotonic relationship between structural and functional connectivity, underscoring a

critical contribution of remote sources of large-scale neural covariation (e.g. δ and slow oscillations (He et al., 2008; Pan et al., 2013)) to the establishment of interareal rsfMRI coupling. This view is in keeping with correlational evidence of a dissociation between rsfMRI connectivity and underlying anatomical connections, such in the case of acallosal brains in which preserved bi-hemispheric connectivity has been repeatedly observed (O'Reilly et al., 2013; Sforazzini et al., 2016; Tyszka et al., 2011). It should be emphasized here that these results should not be intended as a refutation of the structural foundations of rsfMRI connectivity, but rather the basis of an updated framework in which reciprocal interareal rsfMRI coupling can be strongly biased, or even overridden, by slow synchronized input from global rhythm generators.

Second, our results also provide a novel reference framework for the interpretation and reverse engineering of rsfMRI overconnectivity observed in brain pathology, especially in degenerative or neurological states characterized by rsfMRI overconnectivity. Although sometimes compounded by pathophysiological rearrangements in synaptic activity (Busche & Konnerth, 2016), observations of unexpected early-stage increases in functional connectivity in degenerative or neurological conditions characterized by loss of or reduced cortical function such as Alzheimer's disease or stroke have been speculatively conceptualized as the result of compensatory rerouting of signal propagation along indirect structural paths, a neuroadaptive strategy aimed at maintaining task performance (Hillary & Grafman, 2017; Pusil et al., 2019; Siegel et al., 2016). Our findings offer an alternative, network-level physiological mechanism for these clinical observations, suggesting that rsfMRI overconnectivity may reflect reduced high frequency cortical activity of more local origin, and consequently enhanced phase locking of residual firing to the highly excitable phases of global low-frequency rhythms generated in subcortical modulatory centers (Reimann & Niendorf, 2020; Safaai et al., 2015) and/or reflecting cortical-subcortical loops (Gent et al., 2018). EEG and MEG studies in neurological populations are consistent with this hypothesis, as rsfMRI overconnectivity and robust δ hyper-synchronization have been previously observed ipsilaterally to lesioned areas in stroke (Dubovik et al., 2012; Siegel et al., 2016). Similar findings have been reported in Alzheimer's disease patients, in which this effect appears to be especially prominent in polymodal cortical areas (Huth et al., 2012; Ranasinghe et al., 2020). Within such a framework, functional impairments in cortical activity following degenerative pathology could manifest as hyper-synchronization during pre-disease states, eventually reverting to hypotrophy-associated under-connectivity at advanced stages of brain pathology.

While a neural mass phenomenon like interareal rsfMRI coupling cannot be mechanistically dissected into discrete circuital elements, our observation of foci of overconnectivity in polymodal thalamic areas and the increased synchronization of these with larger cortical territories is intriguing, as it points at a putative involvement of higher order thalamic relay in the generation (or propagation) of the observed overconnectivity. This hypothesis would be consistent with the observation that full expression of δ and slow oscillatory activity requires thalamic participation (David et al., 2013; Hughes et al., 2002), and with recent evidence pointing at the presence of a prefrontal-thalamic loop involved in the generation and propagation of δ synchronization (Gent et al., 2018). However, other modulatory mechanisms (Liu et al., 2018; Safaai et al., 2015) or subcortical substrates (Narikiyo et al., 2020) may similarly (or alternatively) play a role in the observed overconnectivity, and the identification of neural generators of rsfMRI coupling and their involvement in the reconfiguration of rsfMRI topography in response to local perturbations remain an open issue.

The observed increases in slow and δ band coherence upon inhibition of the PFC is in excellent agreement with previous reports of a robust association between spontaneous fMRI activity and slow oscillatory activity (Chan et al., 2017; He et al., 2008; Lu et al., 2007, 2016; Neuner et al., 2014; Pan et al., 2013; Liang Wang et al., 2012). Our findings corroborate and expand these investigations by showing that reconfiguration of rsfMRI connectivity in response to local cortical inactivation is supported by increased interareal slow oscillatory coherence, a phenomenon reflecting DREADD-induced reduction of high frequency firing, and concomitantly increased phase locking of residual spiking activity with ongoing global low-frequency oscillations. Recent work has linked ultra-slow (~0.1 Hz) variation in gamma-band amplitude to the vasomotor activity underlying intrinsic rsfMRI connectivity (Mateo et al., 2017; Nir et al., 2008), suggesting that this rhythm may serve as a possible primary generator of interareal rsfMRI coupling. Interestingly, while we found evidence of ultra-slow ϒ envelope coherence across functionally connected areas under basal conditions (Fig. 3.15c), the corresponding coherence increases upon chemogenetic manipulations were very small and did not correlate with corresponding pairwise rsfMRI overconnectivity. This finding suggests that, under the conditions of our manipulations, rsfMRI overconnectivity is most plausibly explained by increased canonical band (e.g. δ) low frequency inter-areal coherence.

Although the light sedation protocol used in our measurements enhances slow oscillatory rhythms (Franks, 2008), such a brain state is unlikely to be the primary reason for our observation of rsfMRI overconnectivity. Supporting this notion, increased rsfMRI connectivity between homotopic cortical

regions has been observed in awake humans upon inhibitory transcranial magnetic stimulation (TMS) of the primary motor cortex (Strens et al., 2002; Watanabe et al., 2014). Analgously increased rsfMRI overconnectivity and δ hyper-synchronization have also been observed patients with stroke and in early stage Alzheimer's disease imaged in conscious conditions (Dubovik et al., 2012; Huth et al., 2012; Ranasinghe et al., 2020; Siegel et al., 2016). Given the highly dynamic nature of rsfMRI network activity, the sign and neurophysiological signatures identified in this study could however conceivably be affected by arousal levels. In this respect, a recent report of rsfMRI underconnectivity after chemogenetic inhibition of the rat postero-dorsal cingulate cortex is of interest in the light of a possible high-arousal state of these awake, restrained animals (Tu et al., 2020). While the lack of electrophysiological recordings in this study prevents a direct comparison with our findings, high-arousal conditions are characterized by a robust shift towards high frequency LFP activity and a possibly dominant contribution of direct feedforward interactions to interareal communication. Under these conditions, the synchronizing contribution of slow oscillatory activity may thus be largely reduced, and chemogenetic inhibition could thus produce qualitatively different effects. As robust methods for mapping rsfMRI activity in awake mice are becoming available (Gutierrez-Barragan et al., 2022), systematic investigations of the effect of DREADD inhibition as a function of arousal state may help probe the plausibility of this model.

Interestingly, TMS investigations (Watanabe et al., 2014)also show that excitatory pulse stimulations may produce rsfMRI de-synchronization, pointing at a possible general, inverse relationship between local cortical activity and interareal rsfMRI coupling. An analogous relationship might also be present in the mouse because, reconstituting the results of our control experiments, decreased rsfMRI connectivity has been recently observed with excitatory DREADD stimulation of somato-motor areas in lightly anesthetized animals (Markicevic et al., 2020). This relationship however requires further corroboration, as KORD-based chemogenetic inhibition of the cingulate cortex was instead reported by others to produce rsfMRI underconnectivity in anesthetized mice (Peeters et al., 2020). These inconsistencies reveal the critical need to couple perturbational rsfMRI studies with electrophysiological recordings to confirm the effect of the designated manipulation, and relate changes in rsfMRI connectivity to underlying neural rhythms.

A strength of our approach is the use of translationally-relevant fMRI-based readouts enabling a possible extrapolation of experimental findings to analogous human research. However, some limitations need to be recognized when assessing the generalizability of our results across species

and conditions. First, the magnitude and direction of rsfMRI connectivity produced by neuronal inhibition could be manipulation specific (Wiegert et al., 2017), an effect that in the case of chemogenetics might also be compounded by possible off-target effects of commonly used chemogenetic actuators (Gomez et al., 2017). By employing (unlike others, Grayson et al., 2016; Peeters et al., 2020; Tu et al., 2020) a design in which CNO is administered under all conditions to all experimental groups, we were able to rigorously control any confounding effect of this actuator via a direct contrast of CNO-treated control and DREADD-expressing animals. As a result, the effects we report in the manuscript are to be attributed to the sole DREADD activation. The observation that chronic inhibition with Kir2.1 reconstitutes the overconnectivity obtained under DREADD manipulation increases our confidence in the validity of our mechanistic inferences. Second, it should be emphasized that the mechanisms that we report here may not be necessarily applicable to awake, behaving conditions, as task-dependent cognitive and sensory processing may strongly and dynamically bias brain rhythms and interregional coupling beyond what could be inferred in the resting, sedated brain. This aspect however does not diminish the translational impact of our findings, owing to the prominent use of resting-state fMRI to map functional network activity and our current inability to back-translate rsfMRI signatures of brain dysfunction into physiologically interpretable events.

In conclusion, the present work provides causal evidence that inhibition of a cortical region can lead to counterintuitively increased patterns of rsfMRI connectivity, an effect mediated by increased interareal slow-frequency coherence. These findings point at a non-monotonic relationship between regional cortical activity and network-wide rsfMRI connectivity, and define novel testable network-level mechanisms for the emergence of rsfMRI overconnectivity in clinical conditions characterized by loss of cortical function.

Chapter 4: General discussion

This chapter offers a general discussion of the results described above, in the broader context of some ongoing unpublished work which I briefly discuss here, and the results of the following manuscript I contributed to:

Trakoshis S, Martínez-Cañada P, Rocchi F, Canella C, You W, Chakrabarti B, Ruigrok AN, Bullmore ET, Suckling J, Markicevic M, Zerbi V, Baron-Cohen S, Gozzi A, Lai MC, Panzeri S, Lombardo MV. (2020). *Intrinsic excitation-inhibition imbalance affects medial prefrontal cortex differently in autistic men versus women* eLife. 2020; 9. 0/08/05.

A full version of the article is available in Appendix I, appended to this thesis (page 92).

4.1 Towards physiological decoding of rsfMRI dysconnectivity?

The results illustrated in chapter 3 show that sustained neural inhibition of a cortical area can lead to rsfMRI overconnectivity between the manipulated area and some of its direct axonal targets. Electrophysiological investigations revealed that this effect is associated with increased coherence in low-frequency oscillations (0.1 - 4 Hz), hence uncovering a possible mechanistic link between increased low-frequency neural dynamics and macroscale rsfMRI over synchronization. This finding advances our understanding of the basic foundational mechanisms linking inter-areal patterns of brain activity to fMRI-based metrics of regional communication widely used in cognitive neuroscience.

In-depth investigations of how regional suppression of neural activity reverberates on the spatiotemporal structure of spontaneous rsfMRI activity are of equal (if not greater) interest for the clinical interpretation of neural patterns of overconnectivity in brain disorders. Specifically, our results show how the combined use of chemo-fMRI and multielectrode investigations allow for a targeted deconstruction of rsfMRI coupling, which in turn offer the opportunities to mechanistically interpret and physiologically decode aberrant rsfMRI connectivity patterns in clinical conditions. We extensively discussed in the previous chapter some of the direct implications of this finding for neurological disorders characterized by loss of cortical activity like stroke or Alzheimer's disease.

Importantly, our results may also allow us to make testable predictions about the network effects of neural manipulations that increase (rather than inhibit) regional activity, hence offering opportunities to physiologically "decode" atypical patterns of functional connectivity. Research along this direction might have very important translational relevance, as increased excitability and elevated excitatory/inhibitory imbalance (E/I imbalance) have been largely implicated in the

etiopathology of ASD and other developmental disorders, in which atypical patterns of functional connectivity have been repeatedly described (discussed in sections 1.5.2). Specifically, our result suggests that increased regional excitability (as opposed to regional inhibition) would lead to an fMRI network desynchronization, a phenotype already observed in multiple models of ASD characterized by E/I imbalance (Bertero et al., 2018; Pagani et al., 2019) and in clinical populations. In the next section, I briefly present the results of ongoing, unpublished investigations aimed to formally test these hypotheses. Given the preliminary nature of these results, and in the interest of keeping my thesis compact, I have decided to briefly mention our findings as part of a general discussion rather than reporting them formally in a dedicated chapter.

4.2 Increased E/I imbalance in the mouse PFC disrupts rsfMRI connectivity

In chapter 3, we showed that PFC inhibition leads to rsfMRI overconnectivity. Following this line of reasoning, we hypothesized that increasing the PFC excitatory neurons' excitability would result in desynchronization between the areas of the DMN. Based on this assumption, we designed a proof-of-concept chemogenetic study aimed to increase the excitability of pyramidal neurons in the PFC. This investigation, which was part of a follow-up line of research, was eventually included in the work described in Chapter 3, as a response to a reviewer's question (depicted in Figure 3.13, methods section 3.2). However, the original goal of this initial study was to generate a large and unspecific increase in regional E/I in PFC, a manipulation that in previous seminal work from Yizhar et al. (2011) was found to produce behavioral alterations of relevance for developmental disorders. To remotely increase fronto-cortical excitability, we bilaterally transduced the PFC with the excitatory hM3Dq DREADD using a calmodulin-kinase-alfa promoter, a strategy enabling reliable targeting of pyramidal neurons (X. Wang et al., 2013; Watakabe et al., 2015). Control (sham injected) and hM3Dq-expressing mice were then subjected to rsfMRI scanning or electrophysiological recordings before and after intravenous administration of the DREADD activator clozapine-N-oxide (CNO). Recapitulating our prior work, to account for CNO's slow pharmacokinetic profile in the mouse brain (Jendryka et al., 2019; Trakoshis et al., 2020), all imaging and electrophysiological recordings were acquired using a combination of medetomidine and low-dose isoflurane (Grandjean et al., 2020; Lee et al., 2021) and divided into three time windows: a pre-CNO injection baseline, a transitory (0 -15 min) drug-equilibration period, and an active time window (15-35 min post-CNO injection) to which all our rsfMRI analyses refer to.

To test the efficacy of the employed manipulation, we initially performed electrophysiological recordings in the PFC of hM3Dq-transduced or control mice before and after CNO injection, under the same experimental settings employed in rsfMRI imaging, and following the procedure described in Chapter 3. As expected, CNO administration robustly increased firing rate in the PFC of hM3Dq expressing mice, but not in control subjects (Fig. 4.1a, $p<0.001$, Wilcoxon rank-sum tests). We next evaluated local field potential (LFP) traces acquired from the same set of recordings. Band-specific spectral analysis of LFP recordings revealed in hM3Dq-transduced animals a robust increase in β- and y-band power after CNO administration with respect to CNO-treated controls, an effect consistent with the observed firing rate increase ($q<0.001$ FDR corrected, Wilcoxon rank-sum tests, Fig. 4.1b). Notably, the LFP power increase in these bands was also accompanied by a reduction in all the other frequencies in DREADD-expressing subjects, an effect that was quantitively prominent in the delta and slow bands (Fig. 4.1b, $q<0.001$, Wilcoxon rank-sum tests, FDR corrected). In the light of our results in chapter 3, these results document that, according to our predictions, this manipulation effectively reverses the neural signature produced by chemogenetic inhibition in the PFC, leading to locally increased firing activity and possibly reduced synchronization with slow global rhythms (Einevoll et al., 2013; Logothetis, 2008). To verify whether this effect would produce fMRI desynchronization (i.e. rsfMRI *hypo*connectivity), we next compared rsfMRI connectivity patterns in hM3Dq transduced and control mice during the active phase upon acute CNO administration. Interestingly, voxel-wise mapping revealed dramatically reduced rsfMRI connectivity between the PFC and its target regions within the DMN in DREADD-expressing mice (t-test, $p < 0.05$, $t > 2$, FWE cluster-corrected, $p < 0.05$; Fig. 4.1c). This effect was corroborated by regional quantifications of rsfMRI underconnectivity along the cingulate and retrosplenial axis of the DMN (two-way repeated-measures ANOVA, $F_{1,35} = 18.25$; $p = 0.001$, Fig. 4.1d). This result is important, as it reveals a putative predictive framework whereby neural inhibition produces over synchronization of the silenced region with ongoing global rhythms, whilst increased excitability shifts LFP oscillations to the higher frequency, possibly desynchronizing them with ongoing slower rhythms. We are now carrying out multi-electrode investigations to test the validity of this notion. Importantly, at the brain-wide level, our manipulation induced patterns of desynchronization between the areas of the DMN, hence establishing a putative unifying mechanistic link between E/I imbalance and impaired functional connectivity.

To further corroborate this notion and extend it to behavioral domains of relevance for developmental disorders, we next carried out behavioral investigations of social activity in the same

mice used for brain imaging using a three-chamber sociability test. This study was prompted by previous work convincingly linking optogenetically induced E/I imbalance in the mouse PFC to socio-behavioral impairments reminiscent of ASD-like core symptoms (Selimbeyoglu et al., 2017; Yizhar et al., 2011). To replicate the experimental conditions upon which our manipulation exertd their maximal effects, behavioral tests were carried out 30 min after CNO administration. As expected, sham mice exhibited social preference, i.e. they spent significantly more time sniffing a stimulus mouse compared to an empty cup (Fig. 4.1e),. By contrast, social preference in hM3Dq-expressing mice was strongly attenuated (paired t-test, $p = 0.07$ Fig. 4.1e). In keeping with this, a comparison of the corresponding metric of sociability (social index, Cutuli et al., 2016) revealed a robust reduction in sociability in DREADD-expressing mice compared to control animals (t-test, $p = 0.009$ Fig. 4.1f). Taken together, these results suggest that behaviorally-relevant disruption of E/I balance results in largely disrupted cortico-cortical fMRI connectivity. More broadly, these findings also suggest that the rsfMRI connectivity can be inversely (and bidirectionally) related to the regional patterns of brain activity, corroborating a non-monotonic nature of this phenomenon.

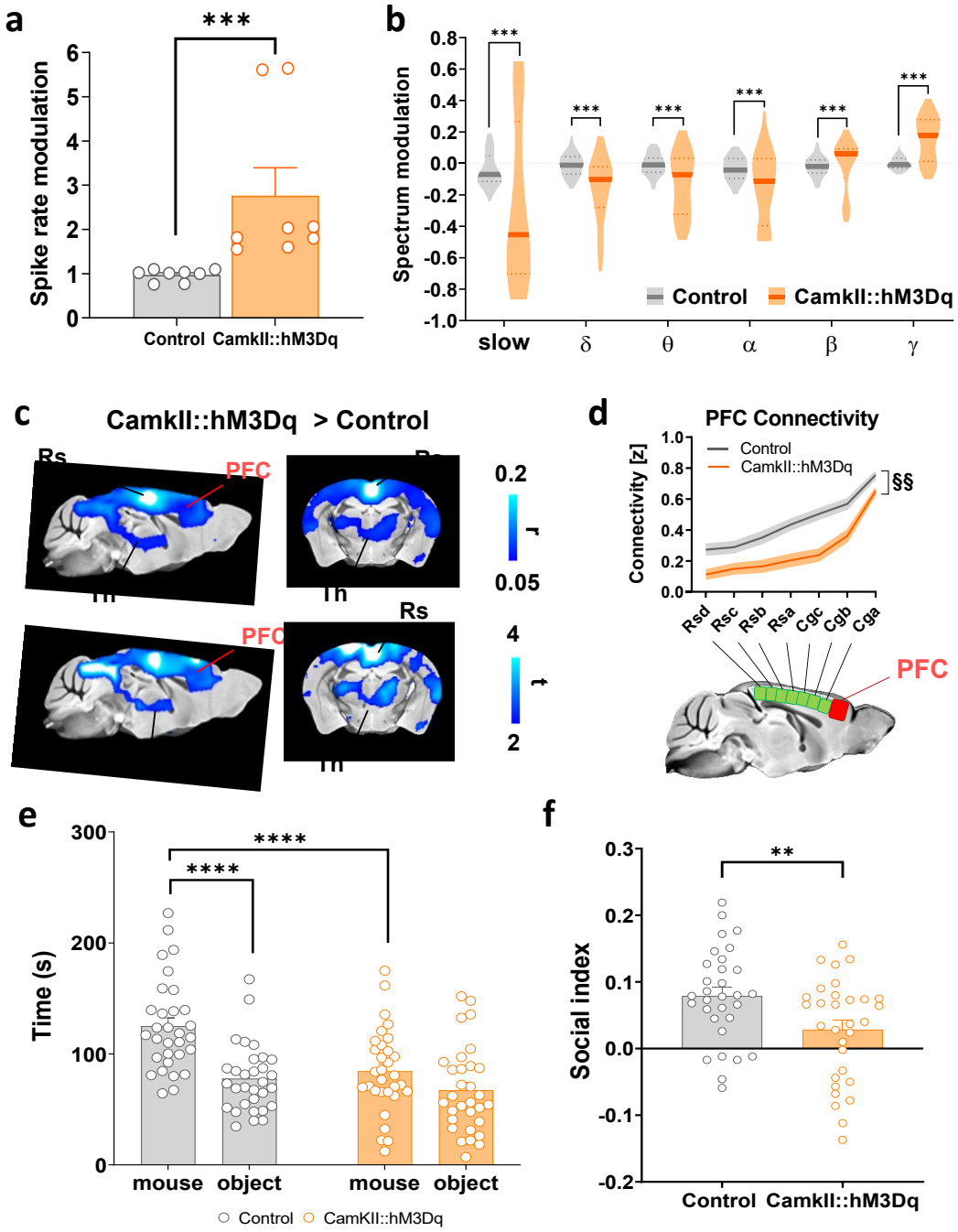

Figure 4.1 Chemogenetic excitation of excitatory neurons. ***(a)*** *Increased firing rate in hM3Dq-expressing mice compared to controls. Wilcoxon rank-sum tests, *** p<0.001.* ***(b)*** *Quantification of corresponding band-specific power spectrum changes upon CNO injection Wilcoxon rank-sum tests, FDR corrected, *** q<0.001.* ***(c)*** *Between-group PFC seed-based connectivity difference map in mice expressing AAV8-CamkII-hM3Dq (n = 20) or subjected to sham viral injections (control, n = 17) during the CNO active phase.* ***(d)*** *Antero-posterior profiling of rsfMRI connectivity of the PFC along the midline axis of the mouse DMN in the two cohorts. §§ p<0.01, 2-way ANOVA repeated measurements, group effect.* ***(e)*** *Result from a three-chamber sociability test (time spent sniffing, (controls n = 31, CamKII::hM3Dq expressing mice, n = 31).* ***(f)*** *Quantification of the results in (e) in terms of sociability index (i.e. time spent sniffing normalized over the total time spent sniffing). *** p < 0.001, ** p < 0.01 Two-tailed Student t-test. Barplots: data are plotted as mean ± SEM. Violin plots: thick lines represent the median, dashed lines indicate 25th and 75th percentile, respectively. Cg: cingulate cortex; PFC: prefrontal cortex, RS: retrosplenial cortex; Th: Thalamus. Panels a-d has been reproduced from previous figure 3.13 e-h.*

Based on the evidence of inhibitory interneuron dysfunction in human developmental disorders (Marín, 2012; Yizhar et al., 2011), we next investigated whether a reduced inhibitory activity would produce a similar neural response, functional connectivity, and behavioral effects. To this aim, we bilaterally injected a floxed version of hM4Di inhibitory DREADD in a mouse line expressing the Cre-recombinase construct in fast/spiking parvalbumin PV+ neurons (Cardin et al., 2009; Markicevic et al., 2018). Littermate mice undergoing sham injections were used as control animals. To test the presence of increased excitability upon chemogenetic inhibition of PV+ interneurons, we performed electrophysiological recordings in the PFC of hM4Di-transduced animals before and after CNO administration. During the DREADD active phase, hM4Di-expressing mice showed a moderate increase in firing rate compared to sham littermates (Fig. 4.2a, p= 0.017, Wilcoxon rank-sum test). Subsequent LFP analyses showed that PV+ neuron inhibition was associated with increased high-frequency LFP power after CNO administration (Wilcoxon rank-sum test, FDR corrected, θ $q < 0.001$; α $q < 0.0$; β $q < 0.0\ 01$; γ $q < 0.01$). However, unlike CamkII::hM3Dq mice, in PV::hM3Di mice delta activity was found to be increased, and no alteration in slow band power was observed (Fig. 4.2b, Wilcoxon rank-sum test, FDR corrected, slow $q = 0.063$, δ $q < 0.001$). Interestingly, subsequent rsfMRI connectivity mapping revealed functional overconnectivity between PFC and cortical terminals of the DMN in PV::hM4Di expressing mice compared to control animals (t-test, $p < 0.05$, $t > 2$, FWE cluster-corrected, $p < 0.05$; Fig. 4.2c; two-way repeated-measures ANOVA, $F_{1,31} = 8.022$; $p = 0.008$, Fig. 4.2d). This effect appeared to recapitulate the connectivity signature observed in CamkII::hM3Dq mice, although the strength and extension of the mapped dysconnectivity were, in this case, largely reduced. A replication of socio-behavioral testing in these mice showed the presence of mildly reduced social preference DREADD-expressing mice upon administration of CNO.

Notwithstanding some (expected) differences in the neural signature associated with these two manipulations, the results we obtained are in excellent agreement, supporting the notion that E/I imbalance in the PFC results in disrupted brain-wide functional hypoconnectivity and reduced sociability, hence mechanistically linking some key endophenotypes that are largely investigated in human developmental disorders like ASD. Importantly, our results also represent an interesting extension of prior behavioral work obtained with optogenetics (Yizhar et al., 2011), suggesting that DREADD represents a valuable experimental platform enabling the induction of long-lasting manipulation of translational relevance for the study of brain disorders. As such, chemogenetic offers the opportunity to investigate these phenomena in longitudinal studies, for example, by probing the role of E/I imbalance in critical developmental periods. Our approach also allowed us to link

bidirectional manipulations of neural activity to functional connectivity as measured with rsfMRI, providing a multiscale characterization of brain connectivity that can help future decoding of brain disorders in the human population. In the next section, I will describe a first example of the possibility of using this approach to physiologically decode dysconnectivity signals and link them to E/I imbalance in human ASD.

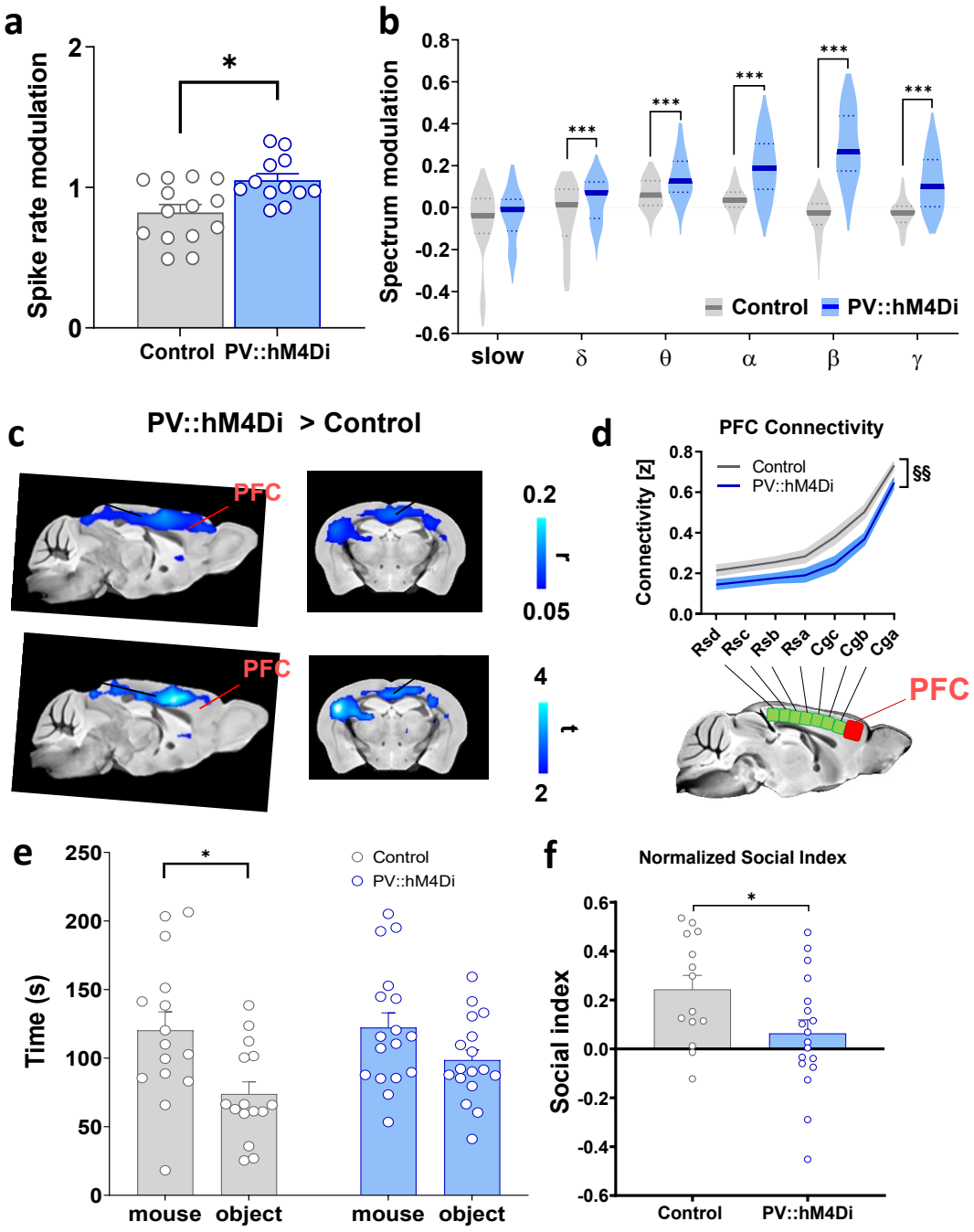

Figure 4.2 Chemogenetic inhibition of PV+ interneurons. ***(a)*** *Increased firing rate in PV::hM4Di mice upon CNO injection. Wilcoxon rank-sum tests, FDR corrected, * q<0.05.* ***(b)*** *Quantification of the corresponding band-specific power spectrum changes in the PFC. Wilcoxon rank-sum tests, FDR corrected, *** q<0.001.* ***(c)*** *Between-group PFC seed-based connectivity difference maps revealed rsfMRI underconnectivity (blue) in the DMN of PV::hM4Di expressing mice during the active CNO phase. PV::Cre mice were bilaterally injected with AAV9-hSyn-DIO-hM4Di (n = 16) or were subjected to sham injections (control, n = 17).* ***(d)*** *Antero-posterior profiling of rsfMRI connectivity of the PFC along the midline axis of the mouse DMN.* ***(e)*** *Time spent sniffing a social stimulus vs. an object in a three-chamber test for social cognition. Data measured during social preference trial in controls (n = 15) and PV::hM4Di expressing mice (n = 17).* ***(f)*** *The time spent sniffing has been normalized over the total time spent sniffing. Two-tailed Student t-test, * p < 0.05. Barplots: data are plotted as mean ± SEM. Violin plots: thick lines represent the median, dashed lines indicate 25th and 75th percentile, respectively. Cg: cingulate cortex; PFC: prefrontal cortex, RS: retrosplenial cortex. Panels a-d has been reproduced from previous figure 3.13 a-d.*

4.3 Decoding E/I imbalance in human fMRI timeseries

The results I presented so far provide insights into the link between E/I imbalance and rsfMRI connectivity alterations, as seen in animal models of ASD. But can these findings translate from animals to humans?

A proof of concept demonstration of this possibility has been described in a collaborative project with the Lombardo and Panzeri labs at the IIT, which we published in 2020 (Trakoshis et al., 2020). The goal of this project was to try and decode PFC-related E/I imbalance in fMRI signals from autistic patients by mapping a timeseries metric estimated from the rsfMRI BOLD signal called "Hurst" (H) exponent (Trakoshis et al., 2020). This metric is the exponent of the 1/f spectral power law depicting rsfMRI signal (as well as many other complex physiological timeseries such as EEG etc.). The Hurst exponent represents a measure of "long-term memory" of physiological timeseries (Wei et al., 2013). High H values are thereby associated with so-called "persistent" (e.g., "slowly fluctuating") timeseries, i.e., those in which an increase in values will most likely be followed by an increase in the short term, and a decrease in values will most likely be followed by another decrease in the short term. By contrast, a low H value will be associated with timeseries with minimal or no temporal autocorrelation. Importantly, recent work has proposed that the exponent of the 1/f spectral power law reflects the extent of E/I imbalance (Gao et al., 2017). This suggests that neurophysiologically increased E/I ratio generates flatter 1/f slope driving H (as measured in BOLD fMRI) to be decreased.

In our work, we used a bottom-up strategy, employing computational models of local neuronal microcircuitry, to predict how H in LFP and rsfMRI BOLD data will behave when the E/I balance is disrupted. Our modeling showed an inverse relationship between the H index and E/I ratio in simulated LFP and fMRI data (Fig. 4.3a), with higher excitability corresponding to a lower H index, meaning that signal originated by E/I imbalance affected area are more contaminated by noise and difficult to predict. This result also suggests that the Hurst exponent could be a good index to map underlying between-group differences in the E/I ratio as assessed with rsfMRI. Importantly, to test the in vivo predictive value of our computational modeling, we used the chemo-fMRI approach presented in the previous chapter to increase neurophysiological excitation (CamkII-hM3Dq) or inhibition of local activity (hSyn-hM4Di).

The obtained findings were fully consistent with in-silico predictions, showing that increased neuronal excitability (produced by CamkII::hM3Dq stimulation) resulted in a decrease in H (Fig. 4.3b), a value that does not change significantly when local activity is instead silenced. Notably, when we looked at human rsfMRI data acquired in typically developing controls and male and female patients with ASD, we observed a significant sex-diagnosis interaction in mPFC area A32 (corresponding to the medial prefrontal cortex in rodents). This effect was dominated by a lower Hurst exponent (indicative of increased E/I ratio) in male but not female patients. Interestingly, we also found that this parameter was linearly correlated with camouflaging score in women. This trait reflects the observation that women with autism are sometimes better at hiding ('camouflaging') their difficulties when socializing or communicating than men with autism (L. Hull et al., 2020; Lai et al., 2017). Our results suggest that the better a woman is at camouflaging her autism, the more her brain activity in this region resembled that of non-autistic women (Fig. 4.4e-f).

From a more mechanistic standpoint, our results are important as they prove the feasibility of physiologically decoding rsfMRI signals via the establishments of translational links across species (i.e., rodents to humans), a critical aspect that can be leveraged to probe the predictive value of neurocomputational models and to mechanistically explain how regional perturbations affect the macroscale organization of the brain. This line of research represents a fundamental step towards a better understanding of human pathological phenotypes.

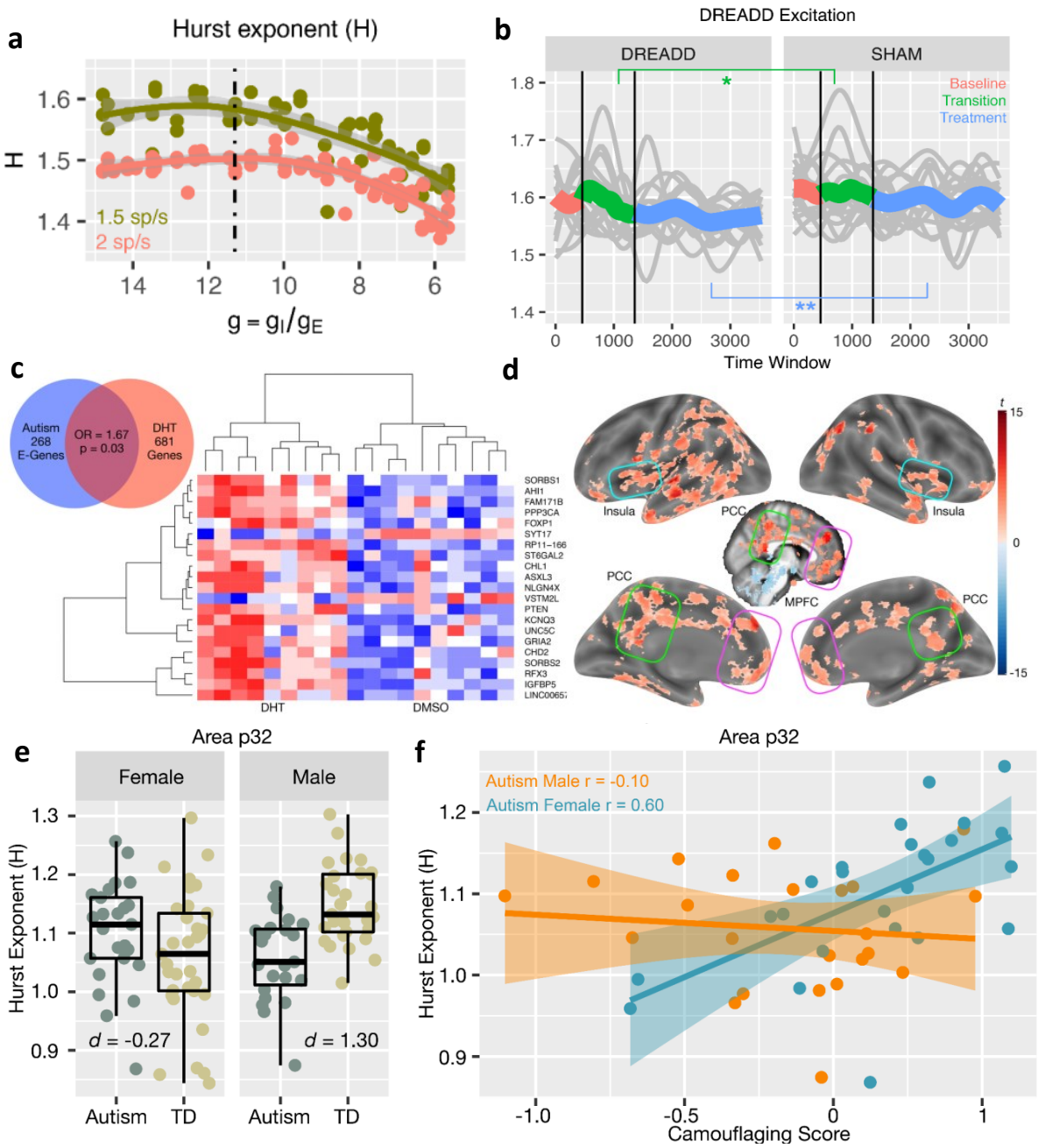

Figure 4.3 Intrinsic excitation-inhibition imbalance affects medial prefrontal cortex differently in autistic men versus women (a) *H values are plotted as a function of g for two different firing rates of thalamic input (1.5 and 2 spikes/second). The reference value of g (shown in previous studies to reproduce cortical data well) is represented by a dashed black line.* ***(b)*** *Changes in H in BOLD from prefrontal cortex (PFC) after real hM3Dq DREADD manipulation in mice. Individual gray lines indicate H for individual mice, while the colored lines indicate Baseline (pink), Transition (green), and Treatment (blue) periods of the experiment.* ***(c)*** *Venn diagram depicting the enrichment between autism-associated genes affecting excitatory neurons (Autism E-Genes) and DHT-sensitive genes. It also includes a heatmap of these genes whereby the color indicates z-normalized expression values. The column dendrogram clearly shows that all samples with DHT treatment are clustered separately from the control (DMSO) samples. Each row depicts the expression of a different gene.* ***(d)*** *t-statistic map from a whole-brain one-sample t-test on these DHT-sensitive and autism-associated genes in excitatory neurons. Results are thresholded at FDR q < 0.01.* ***(e)*** *H estimates from vMPFC (area p32) across males and females with and without autism.* ***(f)*** *shows the correlation between vMPFC H and behavioral camouflaging score in autistic males (orange) and females (blue). Figure and legend adapted from Trakoshis et al. (2020).*

4.4 Limitations and Future Directions

We covered some key limitations of our research in the discussion of our work in chapter 3. I will mention again here the fact that a key priority for this research is to probe the generalizability of our findings to other brain regions and neural substrates: are these relationships specific to the PFC (owing to its profuse innervation of arousal-related nuclei), or can they be generalized to other cortical regions? Recent work from Markicevic et al. (2018) showed that chemogenetic stimulation of sensory areas produced fMRI hypoconnectivity similar to that we mapped in the PFC, suggesting that these properties might possibly be extended to other areas. Further research is required to investigate these aspects. A second key area of high priority future investigations is research on the possible generalizability (or lack thereof) of our results to awake conditions. Our extrapolation of the H index across species (mouse, anesthesia; human awake) suggests the general principle we report here is likely to hold also in the awake resting brain. However, rigorous investigations are required to assess whether the described relationship is affected by arousal, and if so, how the underlying neuronal rhythms are affected. Finally, we are fully aware the possibility of physiologically decoding complex dysconnectivity patterns signals in clinical population is highly ambitious and possibly never fully attainable, owing to our poor understanding of the physiological cascade underlying fMRI connectivity, and the plethora of pathophysiological mechanisms that can confound and complicate the interpretation of rsfMRI signals in the diseased brain. Our research serves nonetheless as a first stepping stone towards the generation of physiologically meaningful models that can help generate clinically testable hypotheses about the origin and significance of brain dysconnectivity in brain disorders.

In summary, the integration of modern approaches for modulating brain activity in the mouse represents a robust platform that will guide us toward a better understanding of the neurological basis of brain-wide functional coupling in health and disease. One of the primary open questions of modern systems neuroscience consists in how whole-brain macro-scale phenomena are influenced by micro-scale activity. In this regard, the emerging evidence of consistent large-scale network mapping in physiologically accessible species such as the mouse is extremely promising. We think a bright future lies ahead for rsfMRI connectivity mapping in rodents owing to its power to bridge the explanatory gap between cellular/microscale neuro phenomena and large-scale neural dynamics. Specifically, our results show the power of chemo-fMRI (Giorgi et al., 2017) to enable a precise deconstruction and manipulation of steady-state network activity that can be critically used to physiologically decoded signatures of atypical connectivity. The findings presented in this thesis are

a striking illustration of this approach, showcasing a collection of novel (and somehow unexpected) insights that call into question the current understanding of functional connectivity. An exciting extension of this research platform is multi-site electrophysiological recordings to reveal the rhythms involved in guiding and shaping long-range functional dysconnectivity. Moreover, new awake rsfMRI protocols (Gutierrez-Barragan et al., 2022; Liang et al., 2015; Stenroos et al., 2018; Tu et al., 2020) will help probe the extension of our results to different brain states (i.e., anesthesia and awake conditions). Lastly, manipulating additional brain areas will probe the generalizability of our findings and might advance our understanding of the connectional atypicalities observed in ASD and other neuropsychiatric diseases.

Reference

Alstott, J., Breakspear, M., Hagmann, P., Cammoun, L., & Sporns, O. (2009). Modeling the impact of lesions in the human brain. *PLoS Computational Biology*, *5*(6), e1000408.

Antoine, M. W., Langberg, T., Schnepel, P., & Feldman, D. E. (2019). Increased Excitation-Inhibition Ratio Stabilizes Synapse and Circuit Excitability in Four Autism Mouse Models. *Neuron*, *101*(4), 648-661.e4. https://doi.org/10.1016/j.neuron.2018.12.026

Bargmann, C. I., & Marder, E. (2013). From the connectome to brain function. *Nature Methods*, *10*(6), 483–490. https://doi.org/10.1038/nmeth.2451

Beier, K. T., Kim, C. K., Hoerbelt, P., Hung, L. W., Heifets, B. D., DeLoach, K. E., Mosca, T. J., Neuner, S., Deisseroth, K., Luo, L., & Malenka, R. C. (2017). Rabies screen reveals GPe control of cocaine-triggered plasticity. *Nature*, *549*(7672), 345–350. https://doi.org/10.1038/nature23888

Belitski, A., Gretton, A., Magri, C., Murayama, Y., Montemurro, M. A., Logothetis, N. K., & Panzeri, S. (2008). Low-Frequency Local Field Potentials and Spikes in Primary Visual Cortex Convey Independent Visual Information. *Journal of Neuroscience*, *28*(22), 5696–5709. https://doi.org/10.1523/JNEUROSCI.0009-08.2008

Belmonte, M. K., Cook, E. H., Anderson, G. M., Rubenstein, J. L. R., Greenough, W. T., Beckel-Mitchener, A., Courchesne, E., Boulanger, L. M., Powell, S. B., Levitt, P. R., Perry, E. K., Jiang, Y. H., DeLorey, T. M., & Tierney, E. (2004). Autism as a disorder of neural information processing: directions for research and targets for therapy. *Molecular Psychiatry*, *9*(7), 646–663. https://doi.org/10.1038/sj.mp.4001499

Berens, P. (2009). CircStat: a MATLAB toolbox for circular statistics. *Journal of Statistical Software*, *31*(1), 1–21.

Bertero, A., Liska, A., Pagani, M., Parolisi, R., Masferrer, M. E., Gritti, M., Pedrazzoli, M., Galbusera, A., Sarica, A., Cerasa, A., Buffelli, M., Tonini, R., Buffo, A., Gross, C., Pasqualetti, M., & Gozzi, A. (2018). Autism-associated 16p11. 2 microdeletion impairs prefrontal functional connectivity in mouse and human. *Brain*, *141*(7), 2055–2065. https://doi.org/10.1093/brain/awy111

Besserve, M., Lowe, S. C., Logothetis, N. K., Schölkopf, B., & Panzeri, S. (2015). Shifts of gamma phase across primary visual cortical sites reflect dynamic stimulus-modulated information transfer. *PLoS Biology*, *13*(9), e1002257.

Biswal, B., Zerrin Yetkin, F., Haughton, V. M., & Hyde, J. S. (1995). Functional connectivity in the motor cortex of resting human brain using echo-planar MRI. *Magnetic Resonance in Medicine*, *34*(4), 537–541.

Bonaventura, J., Eldridge, M. A. G., Hu, F., Gomez, J. L., Sanchez-Soto, M., Abramyan, A. M., Lam, S., Boehm,

M. A., Ruiz, C., Farrell, M. R., Moreno, A., Galal Faress, I. M., Andersen, N., Lin, J. Y., Moaddel, R., Morris, P. J., Shi, L., Sibley, D. R., Mahler, S. V., … Michaelides, M. (2019). High-potency ligands for DREADD imaging and activation in rodents and monkeys. *Nature Communications*, *10*(1), 4627. https://doi.org/10.1038/s41467-019-12236-z

Bosman, C. A., Schoffelen, J.-M., Brunet, N., Oostenveld, R., Bastos, A. M., Womelsdorf, T., Rubehn, B., Stieglitz, T., De Weerd, P., & Fries, P. (2012). Attentional stimulus selection through selective synchronization between monkey visual areas. *Neuron*, *75*(5), 875–888.

Bossier, H., Roels, S. P., Seurinck, R., Banaschewski, T., Barker, G. J., Bokde, A. L. W., Quinlan, E. B., Desrivières, S., Flor, H., Grigis, A., Garavan, H., Gowland, P., Heinz, A., Ittermann, B., Martinot, J.-L., Artiges, E., Nees, F., Orfanos, D. P., Poustka, L., … Moerkerke, B. (2020). The empirical replicability of task-based fMRI as a function of sample size. *NeuroImage*, *212*, 116601. https://doi.org/https://doi.org/10.1016/j.neuroimage.2020.116601

Bowyer, S. M. (2016). Coherence a measure of the brain networks: past and present. *Neuropsychiatric Electrophysiology*, *2*(1), 1–12.

Brock, J., Brown, C., & Boucher, J. (2007). Disordered connectivity in the autistic brain: Challenges for the 'new psychophysiology.' *International Journal of Psychophysiology*, *63*(2), 164–172. https://doi.org/10.1016/J.IJPSYCHO.2006.03.012

Buckner, R. L., Andrews-Hanna, J. R., & Schacter, D. L. (2008). The Brain's Default Network. *Annals of the New York Academy of Sciences*, *1124*(1), 1–38. https://doi.org/10.1196/annals.1440.011

Busche, M. A., & Konnerth, A. (2016). Impairments of neural circuit function in Alzheimer's disease. *Philosophical Transactions of the Royal Society B: Biological Sciences*, *371*(1700), 20150429.

Buzsáki, G. (2006). *Rhythms of the Brain*. Oxford University Press. https://doi.org/10.1093/acprof:oso/9780195301069.001.0001

Buzsáki, G., Draguhn, A., & Buzsaki, G. (2004). Neuronal oscillations in cortical networks. *Science*, *304*(5679), 1926–1929. https://doi.org/10.1126/science.1099745

Campbell, E. J., & Marchant, N. J. (2018). The use of chemogenetics in behavioural neuroscience: receptor variants, targeting approaches and caveats. In *British Journal of Pharmacology*. https://doi.org/10.1111/bph.14146

Canitano, R. (2007). Epilepsy in autism spectrum disorders. *European Child & Adolescent Psychiatry*, *16*(1), 61–66. https://doi.org/10.1007/s00787-006-0563-2

Cardin, J. A., Carlén, M., Meletis, K., Knoblich, U., Zhang, F., Deisseroth, K., Tsai, L.-H., & Moore, C. I. (2009).

Driving fast-spiking cells induces gamma rhythm and controls sensory responses. *Nature*, *459*(7247), 663–667. https://doi.org/10.1038/nature08002

Carlén, M. (2017). What constitutes the prefrontal cortex? *Science*, *358*(6362), 478–482.

Chan, R. W., Leong, A. T. L., Ho, L. C., Gao, P. P., Wong, E. C., Dong, C. M., Wang, X., He, J., Chan, Y.-S., & Lim, L. W. (2017). Low-frequency hippocampal–cortical activity drives brain-wide resting-state functional MRI connectivity. *Proceedings of the National Academy of Sciences*, *114*(33), E6972–E6981.

Chao, H.-T., Chen, H., Samaco, R. C., Xue, M., Chahrour, M., Yoo, J., Neul, J. L., Gong, S., Lu, H.-C., Heintz, N., Ekker, M., Rubenstein, J. L. R., Noebels, J. L., Rosenmund, C., & Zoghbi, H. Y. (2010). Dysfunction in GABA signalling mediates autism-like stereotypies and Rett syndrome phenotypes. *Nature*, *468*(7321), 263–269. https://doi.org/10.1038/nature09582

Clinton, S. M., & Meador-Woodruff, J. H. (2004). Thalamic dysfunction in schizophrenia: neurochemical, neuropathological, and in vivo imaging abnormalities. *Schizophrenia Research*, *69*(2–3), 237–253.

Coletta, L., Pagani, M., Whitesell, J. D., Harris, J. A., Bernhardt, B., & Gozzi, A. (2020). Network structure of the mouse brain connectome with voxel resolution. *Science Advances*, *6*(51), eabb7187.

Corbetta, M., & Shulman, G. L. (2002). Control of goal-directed and stimulus-driven attention in the brain. *Nature Reviews Neuroscience*, *3*(3), 201–215. https://doi.org/10.1038/nrn755

Cutuli, D., Pagani, M., Caporali, P., Galbusera, A., Laricchiuta, D., Foti, F., Neri, C., Spalletta, G., Caltagirone, C., Petrosini, L., & Gozzi, A. (2016). Effects of omega-3 fatty acid supplementation on cognitive functions and neural substrates: A voxel-based morphometry study in aged mice. *Frontiers in Aging Neuroscience*, *8*(MAR), 1–14. https://doi.org/10.3389/fnagi.2016.00038

Dani, V. S., Chang, Q., Maffei, A., Turrigiano, G. G., Jaenisch, R., & Nelson, S. B. (2005). Reduced cortical activity due to a shift in the balance between excitation and inhibition in a mouse model of Rett syndrome. *Proceedings of the National Academy of Sciences of the United States of America*, *102*(35), 12560–12565. https://doi.org/10.1073/pnas.0506071102

Davenport, E. C., Szulc, B. R., Drew, J., Taylor, J., Morgan, T., Higgs, N. F., López-Doménech, G., & Kittler, J. T. (2019). Autism and Schizophrenia-Associated CYFIP1 Regulates the Balance of Synaptic Excitation and Inhibition. *Cell Reports*, *26*(8), 2037-2051.e6. https://doi.org/10.1016/j.celrep.2019.01.092

David, F., Schmiedt, J. T., Taylor, H. L., Orban, G., Di Giovanni, G., Uebele, V. N., Renger, J. J., Lambert, R. C., Leresche, N., & Crunelli, V. (2013). Essential thalamic contribution to slow waves of natural sleep. *Journal of Neuroscience*, *33*(50), 19599–19610.

Deco, G., Kringelbach, M. L., Jirsa, V. K., & Ritter, P. (2017). The dynamics of resting fluctuations in the brain:

metastability and its dynamical cortical core. *Scientific Reports*, *7*(1), 3095. https://doi.org/10.1038/s41598-017-03073-5

Deco, G., Ponce-Alvarez, A., Mantini, D., Romani, G. L., Hagmann, P., & Corbetta, M. (2013). Resting-state functional connectivity emerges from structurally and dynamically shaped slow linear fluctuations. *The Journal of Neuroscience : The Official Journal of the Society for Neuroscience*, *33*(27), 11239–11252. https://doi.org/10.1523/JNEUROSCI.1091-13.2013

DeFelipe, J., López-Cruz, P. L., Benavides-Piccione, R., Bielza, C., Larrañaga, P., Anderson, S., Burkhalter, A., Cauli, B., Fairén, A., Feldmeyer, D., Fishell, G., Fitzpatrick, D., Freund, T. F., González-Burgos, G., Hestrin, S., Hill, S., Hof, P. R., Huang, J., Jones, E. G., … Ascoli, G. A. (2013). New insights into the classification and nomenclature of cortical GABAergic interneurons. *Nature Reviews Neuroscience*, *14*(3), 202–216. https://doi.org/10.1038/nrn3444

Delattre, V., La Mendola, D., Meystre, J., Markram, H., & Markram, K. (2013). Nlgn4 knockout induces network hypo-excitability in juvenile mouse somatosensory cortex in vitro. *Scientific Reports*, *3*(1), 2897. https://doi.org/10.1038/srep02897

Di Martino, A., Yan, C.-G., Li, Q., Denio, E., Castellanos, F. X., Alaerts, K., Anderson, J. S., Assaf, M., Bookheimer, S. Y., Dapretto, M., Deen, B., Delmonte, S., Dinstein, I., Ertl-Wagner, B., Fair, D. A., Gallagher, L., Kennedy, D. P., Keown, C. L., Keysers, C., … Milham, M. P. (2014). The autism brain imaging data exchange: towards a large-scale evaluation of the intrinsic brain architecture in autism. *Molecular Psychiatry*, *19*(6), 659–667. https://doi.org/10.1038/mp.2013.78

Dubovik, S., Pignat, J.-M., Ptak, R., Aboulafia, T., Allet, L., Gillabert, N., Magnin, C., Albert, F., Momjian-Mayor, I., & Nahum, L. (2012). The behavioral significance of coherent resting-state oscillations after stroke. *Neuroimage*, *61*(1), 249–257.

Einevoll, G. T., Kayser, C., Logothetis, N. K., & Panzeri, S. (2013). Modelling and analysis of local field potentials for studying the function of cortical circuits. *Nature Reviews Neuroscience*, *14*(11), 770–785. https://doi.org/10.1038/nrn3599

Eldaief, M. C., Halko, M. A., Buckner, R. L., & Pascual-Leone, A. (2011). Transcranial magnetic stimulation modulates the brain's intrinsic activity in a frequency-dependent manner. *Proceedings of the National Academy of Sciences*, *108*(52), 21229–21234.

Farrell, M. S., & Roth, B. L. (2013). Pharmacosynthetics: reimagining the pharmacogenetic approach. *Brain Research*, *1511*, 6–20.

Ferrari, L., Turrini, G., Crestan, V., Bertani, S., Cristofori, P., Bifone, A., & Gozzi, A. (2012). A robust

experimental protocol for pharmacological fMRI in rats and mice. *Journal of Neuroscience Methods*, *204*(1), 9–18.

Fox, M. D., & Raichle, M. E. (2007). Spontaneous fluctuations in brain activity observed with functional magnetic resonance imaging. *Nature Reviews Neuroscience*, *8*(9), 700–711. https://doi.org/10.1038/nrn2201

Franks, N. P. (2008). General anaesthesia: from molecular targets to neuronal pathways of sleep and arousal. *Nature Reviews Neuroscience*, *9*(5), 370–386.

Fries, P. (2005). A mechanism for cognitive dynamics: Neuronal communication through neuronal coherence. *Trends in Cognitive Sciences*, *9*(10), 474–480. https://doi.org/10.1016/j.tics.2005.08.011

Friston, K. J. (2011). Functional and Effective Connectivity: A Review. *Brain Connectivity*, *1*(1), 13–36. https://doi.org/10.1089/brain.2011.0008

Friston, K. J., & Büchel, C. (2004). Functional Connectivity. In *Human Brain Function* (pp. 999–1018). Elsevier. https://doi.org/10.1016/B978-012264841-0/50051-2

Friston, K. J., & Frith, C. D. (1995). Schizophrenia: a disconnection syndrome. *Clin Neurosci*, *3*(2), 89–97.

Gao, R., Peterson, E. J., & Voytek, B. (2017). Inferring synaptic excitation/inhibition balance from field potentials. *NeuroImage*, *158*(June), 70–78. https://doi.org/10.1016/j.neuroimage.2017.06.078

Garrity, A. G., Pearlson, G. D., McKiernan, K., Lloyd, D., Kiehl, K. A., & Calhoun, V. D. (2007). Aberrant "default mode" functional connectivity in schizophrenia. *American Journal of Psychiatry*, *164*(3), 450–457.

Gent, T. C., Bandarabadi, M., Herrera, C. G., & Adamantidis, A. R. (2018). Thalamic dual control of sleep and wakefulness. *Nature Neuroscience*, *21*(7), 974–984. https://doi.org/10.1038/s41593-018-0164-7

Geschwind, D. H. (2009). Advances in Autism. *Annual Review of Medicine*, *60*(1), 367–380. https://doi.org/10.1146/annurev.med.60.053107.121225

Gibson, J. R., Bartley, A. F., Hays, S. A., & Huber, K. M. (2008). Imbalance of Neocortical Excitation and Inhibition and Altered UP States Reflect Network Hyperexcitability in the Mouse Model of Fragile X Syndrome. *Journal of Neurophysiology*, *100*(5), 2615–2626. https://doi.org/10.1152/jn.90752.2008

Gillberg, C., & Billstedt, E. (2000). Autism and Asperger syndrome: coexistence with other clinical disorders. *Acta Psychiatrica Scandinavica*, *102*(5), 321–330. https://doi.org/10.1034/j.1600-0447.2000.102005321.x

Giorgi, A., Migliarini, S., Galbusera, A., Maddaloni, G., Mereu, M., Margiani, G., Gritti, M., Landi, S., Trovato, F., Bertozzi, S. M., Armirotti, A., Ratto, G. M., De Luca, M. A., Tonini, R., Gozzi, A., & Pasqualetti, M.

(2017). Brain-wide Mapping of Endogenous Serotonergic Transmission via Chemogenetic fMRI. *Cell Reports*, *21*(4), 910–918. https://doi.org/10.1016/j.celrep.2017.09.087

Gomez, J. L., Bonaventura, J., Lesniak, W., Mathews, W. B., Sysa-Shah, P., Rodriguez, L. A., Ellis, R. J., Richie, C. T., Harvey, B. K., Dannals, R. F., Pomper, M. G., Bonci, A., & Michaelides, M. (2017). Chemogenetics revealed: DREADD occupancy and activation via converted clozapine. *Science*, *357*(6350), 503–507. https://doi.org/10.1126/science.aan2475

Goñi, J., Van Den Heuvel, M. P., Avena-Koenigsberger, A., De Mendizabal, N. V., Betzel, R. F., Griffa, A., Hagmann, P., Corominas-Murtra, B., Thiran, J.-P., & Sporns, O. (2014). Resting-brain functional connectivity predicted by analytic measures of network communication. *Proceedings of the National Academy of Sciences*, *111*(2), 833–838.

Gonzalez-Burgos, G., Cho, R. Y., & Lewis, D. A. (2015). Alterations in cortical network oscillations and parvalbumin neurons in schizophrenia. *Biological Psychiatry*, *77*(12), 1031–1040. https://doi.org/10.1016/j.biopsych.2015.03.010

Goulas, A., Majka, P., Rosa, M. G. P., & Hilgetag, C. C. (2019). A blueprint of mammalian cortical connectomes. *PLOS Biology*, *17*(3), e2005346. https://doi.org/10.1371/journal.pbio.2005346

Gozzi, A., Ceolin, L., Schwarz, A., Reese, T., Bertani, S., Crestan, V., & Bifone, A. (2007). A multimodality investigation of cerebral hemodynamics and autoregulation in pharmacological MRI. *Magnetic Resonance Imaging*, *25*(6), 826–833.

Gozzi, A., & Schwarz, A. J. (2016). Large-scale functional connectivity networks in the rodent brain. *NeuroImage*, *127*, 496–509. https://doi.org/10.1016/j.neuroimage.2015.12.017

Grandjean, J., Canella, C., Anckaerts, C., Ayrancı, G., Bougacha, S., Bienert, T., Buehlmann, D., Coletta, L., Gallino, D., & Gass, N. (2020). Common functional networks in the mouse brain revealed by multi-centre resting-state fMRI analysis. *Neuroimage*, *205*, 116278.

Grandjean, J., Zerbi, V., Balsters, J., Wenderoth, N., & Rudina, M. (2017). The structural basis of large-scale functional connectivity in the mouse. *The Journal of Neuroscience*, 0438–17. https://doi.org/10.1523/JNEUROSCI.0438-17.2017

Grayson, D. S., Bliss-Moreau, E., Machado, C. J., Bennett, J., Shen, K., Grant, K. A., Fair, D. A., & Amaral, D. G. (2016). The Rhesus Monkey Connectome Predicts Disrupted Functional Networks Resulting from Pharmacogenetic Inactivation of the Amygdala. *Neuron*, *91*(2), 453–466. https://doi.org/10.1016/j.neuron.2016.06.005

Gusnard, D. A., & Raichle, M. E. (2001). Searching for a baseline: functional imaging and the resting human

brain. *Nature Reviews Neuroscience*, *2*(10), 685–694.

Gutierrez-Barragan, D., Basson, M. A., Panzeri, S., & Gozzi, A. (2019). Infraslow state fluctuations govern spontaneous fMRI network dynamics. *Current Biology*, *29*(14), 2295–2306.

Gutierrez-Barragan, D., Singh, N. A., Alvino, F. G., Coletta, L., Rocchi, F., De Guzman, E., Galbusera, A., Uboldi, M., Panzeri, S., & Gozzi, A. (2022). Unique spatiotemporal fMRI dynamics in the awake mouse brain. *Current Biology*, 1–14. https://doi.org/10.1016/j.cub.2021.12.015

Hagmann, P., Cammoun, L., Gigandet, X., Meuli, R., Honey, C. J., Wedeen, V. J., & Sporns, O. (2008). Mapping the structural core of human cerebral cortex. *PLoS Biology*, *6*(7), e159.

Hall, S. S., Jiang, H., Reiss, A. L., & Greicius, M. D. (2013). Identifying Large-Scale Brain Networks in Fragile X Syndrome. *JAMA Psychiatry*, *70*(11), 1215. https://doi.org/10.1001/jamapsychiatry.2013.247

Harrington, A. J., Raissi, A., Rajkovich, K., Berto, S., Kumar, J., Molinaro, G., Raduazzo, J., Guo, Y., Loerwald, K., Konopka, G., Huber, K. M., & Cowan, C. W. (2016). MEF2C regulates cortical inhibitory and excitatory synapses and behaviors relevant to neurodevelopmental disorders. *ELife*, *5*. https://doi.org/10.7554/eLife.20059

Harris, K. D., & Shepherd, G. M. G. (2015). The neocortical circuit: themes and variations. *Nature Neuroscience*, *18*(2), 170–181. https://doi.org/10.1038/nn.3917

He, B. J., Snyder, A. Z., Zempel, J. M., Smyth, M. D., & Raichle, M. E. (2008). Electrophysiological correlates of the brain's intrinsic large-scale functional architecture. *Proceedings of the National Academy of Sciences*, *105*(41), 16039–16044.

Hillary, F. G., & Grafman, J. H. (2017). Injured brains and adaptive networks: the benefits and costs of hyperconnectivity. *Trends in Cognitive Sciences*, *21*(5), 385–401.

Holiga, Š., Hipp, J. F., Chatham, C. H., Garces, P., Spooren, W., D'Ardhuy, X. L., Bertolino, A., Bouquet, C., Buitelaar, J. K., Bours, C., Rausch, A., Oldehinkel, M., Bouvard, M., Amestoy, A., Caralp, M., Gueguen, S., Ly-Le Moal, M., Houenou, J., Beckmann, C. F., … Dukart, J. (2019). Patients with autism spectrum disorders display reproducible functional connectivity alterations. *Science Translational Medicine*, *11*(481), eaat9223. https://doi.org/10.1126/scitranslmed.aat9223

Honey, C. J., Sporns, O., Cammoun, L., Gigandet, X., Thiran, J.-P., Meuli, R., & Hagmann, P. (2009). Predicting human resting-state functional connectivity from structural connectivity. *Proceedings of the National Academy of Sciences*, *106*(6), 2035–2040.

Hu, D., & Zeng, L.-L. (2019). Introduction. In *Pattern Analysis of the Human Connectome* (pp. 1–16). Springer Singapore. https://doi.org/10.1007/978-981-32-9523-0_1

Huang, X.-Q., Lui, S., Deng, W., Chan, R. C. K., Wu, Q.-Z., Jiang, L.-J., Zhang, J.-R., Jia, Z.-Y., Li, X.-L., & Li, F. (2010). Localization of cerebral functional deficits in treatment-naive, first-episode schizophrenia using resting-state fMRI. *Neuroimage*, *49*(4), 2901–2906.

Hughes, S. W., Cope, D. W., Blethyn, K. L., & Crunelli, V. (2002). Cellular mechanisms of the slow (< 1 Hz) oscillation in thalamocortical neurons in vitro. *Neuron*, *33*(6), 947–958.

Hughes, S. W., Lőrincz, M. L., Parri, H. R., & Crunelli, V. (2011). Infraslow (<0.1Hz) oscillations in thalamic relay nuclei: basic mechanisms and significance to health and disease states. In *Progress in brain research* (Vol. 193, pp. 145–162). Elsevier. https://doi.org/10.1016/B978-0-444-53839-0.00010-7

Hull, L., Lai, M.-C., Baron-Cohen, S., Allison, C., Smith, P., Petrides, K., & Mandy, W. (2020). Gender differences in self-reported camouflaging in autistic and non-autistic adults. *Autism*, *24*(2), 352–363. https://doi.org/10.1177/1362361319864804

Hull, J. V., Jacokes, Z. J., Torgerson, C. M., Irimia, A., Van Horn, J. D., Aylward, E., Bernier, R., Bookheimer, S., Dapretto, M., Gaab, N., Geschwind, D., Jack, A., Nelson, C., Pelphrey, K., State, M., Ventola, P., & Webb, S. J. (2017). Resting-state functional connectivity in autism spectrum disorders: A review. *Frontiers in Psychiatry*, *7*(JAN). https://doi.org/10.3389/fpsyt.2016.00205

Hutchison, R. M., Mirsattari, S. M., Jones, C. K., Gati, J. S., & Leung, L. S. (2010). Functional networks in the anesthetized rat brain revealed by independent component analysis of resting-state FMRI. *Journal of Neurophysiology*, *103*(6), 3398–3406.

Huth, A. G., Nishimoto, S., Vu, A. T., & Gallant, J. L. (2012). A continuous semantic space describes the representation of thousands of object and action categories across the human brain. *Neuron*, *76*(6), 1210–1224.

Jendryka, M., Palchaudhuri, M., Ursu, D., van der Veen, B., Liss, B., Kätzel, D., Nissen, W., & Pekcec, A. (2019). Pharmacokinetic and pharmacodynamic actions of clozapine-N-oxide, clozapine, and compound 21 in DREADD-based chemogenetics in mice. *Scientific Reports*, *9*(1), 1–14. https://doi.org/10.1038/s41598-019-41088-2

Ju, D. W. (2022). *Neuroscience: Canadian 1st Edition Open Textbook* (and S. L. Georgia Bains, Ingrid Barany, Maksym Shcherbina (ed.)). 2022. http://neuroscience.openetext.utoronto.ca/

King, J. B., Prigge, M. B. D., King, C. K., Morgan, J., Weathersby, F., Fox, J. C., Dean, D. C., Freeman, A., Villaruz, J. A. M., Kane, K. L., Bigler, E. D., Alexander, A. L., Lange, N., Zielinski, B., Lainhart, J. E., & Anderson, J. S. (2019). Generalizability and reproducibility of functional connectivity in autism. *Molecular Autism*, *10*(1), 27. https://doi.org/10.1186/s13229-019-0273-5

Knox, J. E., Harris, K. D., Graddis, N., Whitesell, J. D., Zeng, H., Harris, J. A., Shea-Brown, E., & Mihalas, S. (2018). High-resolution data-driven model of the mouse connectome. *Network Neuroscience (Cambridge, Mass.)*, *3*(1), 217–236. https://doi.org/10.1162/netn_a_00066

Lai, M.-C., Lombardo, M. V, Ruigrok, A. N., Chakrabarti, B., Auyeung, B., Szatmari, P., Happé, F., & Baron-Cohen, S. (2017). Quantifying and exploring camouflaging in men and women with autism. *Autism*, *21*(6), 690–702. https://doi.org/10.1177/1362361316671012

Lee, S.-H., Broadwater, M. A., Ban, W., Wang, T.-W. W., Kim, H.-J., Dumas, J. S., Vetreno, R. P., Herman, M. A., Morrow, A. L., & Besheer, J. (2021). An isotropic EPI database and analytical pipelines for rat brain resting-state fMRI. *Neuroimage*, *243*, 118541.

Leichsenring, F., Leibing, E., Kruse, J., New, A. S., & Leweke, F. (2011). Borderline personality disorder. *The Lancet*, *377*(9759), 74–84.

Liang, Z., Watson, G. D. R., Alloway, K. D., Lee, G., Neuberger, T., & Zhang, N. (2015). Mapping the functional network of medial prefrontal cortex by combining optogenetics and fMRI in awake rats. *Neuroimage*, *117*, 114–123.

Lis, E., Greenfield, B., Henry, M., Guilé, J. M., & Dougherty, G. (2007). Neuroimaging and genetics of borderline personality disorder: a review. *Journal of Psychiatry & Neuroscience*, *32*(3), 162.

Liska, A., Galbusera, A., Schwarz, A. J., & Gozzi, A. (2015). Functional connectivity hubs of the mouse brain. *NeuroImage*, *115*, 281–291. https://doi.org/10.1016/j.neuroimage.2015.04.033

Liska, A., & Gozzi, A. (2016). Can mouse imaging studies bring order to autism connectivity chaos? *Frontiers in Neuroscience*, *10*, 484. https://doi.org/10.3389/fnins.2016.00484

Liu, X., De Zwart, J. A., Schölvinck, M. L., Chang, C., Frank, Q. Y., Leopold, D. A., & Duyn, J. H. (2018). Subcortical evidence for a contribution of arousal to fMRI studies of brain activity. *Nature Communications*, *9*(1), 1–10.

Logothetis, N. K. (2008). What we can do and what we cannot do with fMRI. *Nature*, *453*(7197), 869–878.

Lu, H., Wang, L., Rea, W. W., Brynildsen, J. K., Jaime, S., Zuo, Y., Stein, E. A., & Yang, Y. (2016). Low-but not high-frequency LFP correlates with spontaneous BOLD fluctuations in rat whisker barrel cortex. *Cerebral Cortex*, *26*(2), 683–694.

Lu, H., Zou, Q., Gu, H., Raichle, M. E., Stein, E. A., & Yang, Y. (2012). Rat brains also have a default mode network. *Proceedings of the National Academy of Sciences*, *109*(10), 3979–3984. https://doi.org/10.1073/pnas.1200506109

Lu, H., Zuo, Y., Gu, H., Waltz, J. A., Zhan, W., Scholl, C. A., Rea, W., Yang, Y., & Stein, E. A. (2007). Synchronized delta oscillations correlate with the resting-state functional MRI signal. *Proceedings of the National Academy of Sciences*, *104*(46), 18265–18269.

Lynall, M.-E., Bassett, D. S., Kerwin, R., McKenna, P. J., Kitzbichler, M., Muller, U., & Bullmore, E. (2010). Functional connectivity and brain networks in schizophrenia. *Journal of Neuroscience*, *30*(28), 9477–9487.

Manvich, D. F., Webster, K. A., Foster, S. L., Farrell, M. S., Ritchie, J. C., Porter, J. H., & Weinshenker, D. (2018). The DREADD agonist clozapine N-oxide (CNO) is reverse-metabolized to clozapine and produces clozapine-like interoceptive stimulus effects in rats and mice. *Scientific Reports*, *8*(1), 1–10. https://doi.org/10.1038/s41598-018-22116-z

Marín, O. (2012). Interneuron dysfunction in psychiatric disorders. *Nature Reviews Neuroscience*, *13*(2), 107–120. https://doi.org/10.1038/nrn3155

Markicevic, M., Fulcher, B. D., Lewis, C., Helmchen, F., Rudin, M., Zerbi, V., & Wenderoth, N. (2020). Cortical Excitation:Inhibition Imbalance Causes Abnormal Brain Network Dynamics as Observed in Neurodevelopmental Disorders. *Cerebral Cortex*, *30*(9), 4922–4937. https://doi.org/10.1093/cercor/bhaa084

Markicevic, M., Fulcher, B. D., Lewis, C., Helmchen, F., Rudin, M., Zerbi, V., Wenderoth, N., Marija, A., Fulcher, B. D., Lewis, C., Helmchen, F., & Rudin, M. (2018). Cortical excitation : inhibition imbalance causes network-specific functional hypoconnectivity : a DREADD-fMRI study. *BioRxiv*. https://doi.org/10.1101/492108

Mateo, C., Knutsen, P. M., Tsai, P. S., Shih, A. Y., & Kleinfeld, D. (2017). Entrainment of Arteriole Vasomotor Fluctuations by Neural Activity Is a Basis of Blood-Oxygenation-Level-Dependent "Resting-State" Connectivity. *Neuron*, *96*(4), 936-948.e3. https://doi.org/10.1016/j.neuron.2017.10.012

Milham, M., Petkov, C. I., Margulies, D. S., Schroeder, C. E., Basso, M. A., Belin, P., Fair, D. A., Fox, A., Kastner, S., Mars, R. B., Messinger, A., Poirier, C., Vanduffel, W., Van Essen, D. C., Alvand, A., Becker, Y., Ben Hamed, S., Benn, A., Bodin, C., … Zhou, Y. (2020). Accelerating the Evolution of Nonhuman Primate Neuroimaging. *Neuron*, *105*(4), 600–603. https://doi.org/https://doi.org/10.1016/j.neuron.2019.12.023

Mitchell, A. S. (2015). The mediodorsal thalamus as a higher order thalamic relay nucleus important for learning and decision-making. *Neuroscience & Biobehavioral Reviews*, *54*, 76–88.

Mitra, A., Kraft, A., Wright, P., Acland, B., Snyder, A. Z., Rosenthal, Z., Czerniewski, L., Bauer, A., Snyder, L., & Culver, J. (2018). Spontaneous infra-slow brain activity has unique spatiotemporal dynamics and

laminar structure. *Neuron*, *98*(2), 297–305.

Morris, H. M., Hashimoto, T., & Lewis, D. A. (2008). Alterations in somatostatin mRNA expression in the dorsolateral prefrontal cortex of subjects with schizophrenia or schizoaffective disorder. *Cerebral Cortex*, *18*(7), 1575–1587. https://doi.org/10.1093/cercor/bhm186

Munn, B. R., Müller, E. J., Wainstein, G., & Shine, J. M. (2021). The ascending arousal system shapes neural dynamics to mediate awareness of cognitive states. *Nature Communications*, *12*(1), 1–9.

Nagai, Y., Miyakawa, N., Takuwa, H., Hori, Y., Oyama, K., Ji, B., Takahashi, M., Huang, X. P., Slocum, S. T., DiBerto, J. F., Xiong, Y., Urushihata, T., Hirabayashi, T., Fujimoto, A., Mimura, K., English, J. G., Liu, J., Inoue, K. ichi, Kumata, K., … Minamimoto, T. (2020). Deschloroclozapine, a potent and selective chemogenetic actuator enables rapid neuronal and behavioral modulations in mice and monkeys. *Nature Neuroscience*, *23*(9), 1157–1167. https://doi.org/10.1038/s41593-020-0661-3

Nathanson, J. L., Yanagawa, Y., Obata, K., & Callaway, E. M. (2009). Preferential labeling of inhibitory and excitatory cortical neurons by endogenous tropism of adeno-associated virus and lentivirus vectors. *Neuroscience*, *161*(2), 441–450. https://doi.org/10.1016/j.neuroscience.2009.03.032

Neuner, I., Arrubla, J., Werner, C. J., Hitz, K., Boers, F., Kawohl, W., & Shah, N. J. (2014). The default mode network and EEG regional spectral power: a simultaneous fMRI-EEG study. *PLoS One*, *9*(2), e88214.

Nir, Y., Mukamel, R., Dinstein, I., Privman, E., Harel, M., Fisch, L., Gelbard-Sagiv, H., Kipervasser, S., Andelman, F., & Neufeld, M. Y. (2008). Interhemispheric correlations of slow spontaneous neuronal fluctuations revealed in human sensory cortex. *Nature Neuroscience*, *11*(9), 1100–1108.

O'Reilly, J. X., Croxson, P. L., Jbabdi, S., Sallet, J., Noonan, M. P., Mars, R. B., Browning, P. G. F., Wilson, C. R. E., Mitchell, A. S., & Miller, K. L. (2013). Causal effect of disconnection lesions on interhemispheric functional connectivity in rhesus monkeys. *Proceedings of the National Academy of Sciences*, *110*(34), 13982–13987.

Oh, S. W., Harris, J. A., Ng, L., Winslow, B., Cain, N., Mihalas, S., Wang, Q., Lau, C., Kuan, L., Henry, A. M., Mortrud, M. T., Ouellette, B., Nguyen, T. N., Sorensen, S. A., Slaughterbeck, C. R., Wakeman, W., Li, Y., Feng, D., Ho, A., … Zeng, H. (2014). A mesoscale connectome of the mouse brain. *Nature*, *508*(7495), 207–214. https://doi.org/10.1038/nature13186

Pagani, M., Barsotti, N., Bertero, A., Trakoshis, S., Ulysse, L., Locarno, A., Miseviciute, I., De Felice, A., Canella, C., & Supekar, K. (2021). mTOR-related synaptic pathology causes autism spectrum disorder-associated functional hyperconnectivity. *Nature Communications*, *12*(1), 1–15.

Pagani, M., Bertero, A., Liska, A., Galbusera, A., Sabbioni, M., Barsotti, N., Colenbier, N., Marinazzo, D.,

Scattoni, M. L., Pasqualetti, M., & Gozzi, A. (2019). Deletion of Autism Risk Gene Shank3 Disrupts Prefrontal Connectivity. *The Journal of Neuroscience*, *39*(27), 5299–5310. https://doi.org/10.1523/JNEUROSCI.2529-18.2019

Pan, W.-J. J., Thompson, G. J., Magnuson, M. E., Jaeger, D., & Keilholz, S. (2013). Infraslow LFP correlates to resting-state fMRI BOLD signals. *NeuroImage*, *74*, 288–297. https://doi.org/10.1016/j.neuroimage.2013.02.035

Pathania, M., Davenport, E. C., Muir, J., Sheehan, D. F., López-Doménech, G., & Kittler, J. T. (2014). The autism and schizophrenia associated gene CYFIP1 is critical for the maintenance of dendritic complexity and the stabilization of mature spines. *Translational Psychiatry*, *4*(3), e374–e374. https://doi.org/10.1038/tp.2014.16

Paxinos, G., & Franklin, K. B. J. (2004). The mouse brain in stereotaxic coordinates: compact. *Amsterdam, Boston: Elsevier Academic Press). Pazos, A., Cortes, R., and Palacios, JM (1985). Thyrotropin-Releasing Hormone Receptor Binding Sites: Autoradiographic Distribution in the Rat and Guinea Pig Brain. J. Neurochem*, *45*, 1448–1463.

Peeters, L. M., Hinz, R., Detrez, J. R., Missault, S., De Vos, W. H., Verhoye, M., Van der Linden, A., & Keliris, G. A. (2020). Chemogenetic silencing of neurons in the mouse anterior cingulate area modulates neuronal activity and functional connectivity. *Neuroimage*, *220*, 117088.

Ponce-Alvarez, A., Deco, G., Hagmann, P., Romani, G. L., Mantini, D., & Corbetta, M. (2015). Resting-state temporal synchronization networks emerge from connectivity topology and heterogeneity. *PLoS Computational Biology*, *11*(2), e1004100.

Power, J. D., Schlaggar, B. L., & Petersen, S. E. (2014). Studying brain organization via spontaneous fMRI signal. *Neuron*, *84*(4), 681–696.

Pusil, S., López, M. E., Cuesta, P., Bruna, R., Pereda, E., & Maestu, F. (2019). Hypersynchronization in mild cognitive impairment: the 'X'model. *Brain*, *142*(12), 3936–3950.

Quiroga, R. Q., Nadasdy, Z., & Ben-Shaul, Y. (2004). Unsupervised spike detection and sorting with wavelets and superparamagnetic clustering. *Neural Computation*, *16*(8), 1661–1687.

Raichle, M. E. (2015). The brain's default mode network. *Annual Review of Neuroscience*, *38*, 433–447.

Raichle, M. E., MacLeod, A. M., Snyder, A. Z., Powers, W. J., Gusnard, D. A., & Shulman, G. L. (2001). A default mode of brain function. *Proceedings of the National Academy of Sciences*, *98*(2), 676–682.

Ranasinghe, K. G., Cha, J., Iaccarino, L., Hinkley, L. B., Beagle, A. J., Pham, J., Jagust, W. J., Miller, B. L., Rankin, K. P., & Rabinovici, G. D. (2020). Neurophysiological signatures in Alzheimer's disease are distinctly

associated with TAU, amyloid-β accumulation, and cognitive decline. *Science Translational Medicine*, *12*(534).

Reimann, H. M., & Niendorf, T. (2020). The (Un)Conscious Mouse as a Model for Human Brain Functions: Key Principles of Anesthesia and Their Impact on Translational Neuroimaging. *Frontiers in Systems Neuroscience*, *14*, 8. https://doi.org/10.3389/fnsys.2020.00008

Rilling, J. K., Barks, S. K., Parr, L. A., Preuss, T. M., Faber, T. L., Pagnoni, G., Bremner, J. D., & Votaw, J. R. (2007). A comparison of resting-state brain activity in humans and chimpanzees. *Proceedings of the National Academy of Sciences*, *104*(43), 17146–17151. https://doi.org/10.1073/pnas.0705132104

Roth, B. L. (2016). DREADDs for Neuroscientists. *Neuron*, *89*(4), 683–694. https://doi.org/10.1016/j.neuron.2016.01.040

Rubenstein, J. L. R., & Merzenich, M. M. (2003). Model of autism: increased ratio of excitation/inhibition in key neural systems. *Genes, Brain and Behavior*, *2*(5), 255–267. https://doi.org/10.1034/j.1601-183X.2003.00037.x

Rudy, B., Fishell, G., Lee, S., & Hjerling-Leffler, J. (2011). Three groups of interneurons account for nearly 100% of neocortical GABAergic neurons. *Developmental Neurobiology*, *71*(1), 45–61. https://doi.org/10.1002/dneu.20853

Safaai, H., Neves, R., Eschenko, O., Logothetis, N. K., & Panzeri, S. (2015). Modeling the effect of locus coeruleus firing on cortical state dynamics and single-trial sensory processing. *Proceedings of the National Academy of Sciences*, *112*(41), 12834–12839.

Satterstrom, F. K., Kosmicki, J. A., Wang, J., Breen, M. S., De Rubeis, S., An, J.-Y., Peng, M., Collins, R., Grove, J., Klei, L., Stevens, C., Reichert, J., Mulhern, M. S., Artomov, M., Gerges, S., Sheppard, B., Xu, X., Bhaduri, A., Norman, U., … Walters, R. K. (2020). Large-Scale Exome Sequencing Study Implicates Both Developmental and Functional Changes in the Neurobiology of Autism. *Cell*, *180*(3), 568-584.e23. https://doi.org/10.1016/j.cell.2019.12.036

Schleifer, C., Lin, A., Kushan, L., Ji, J. L., Yang, G., Bearden, C. E., & Anticevic, A. (2019). Dissociable disruptions in thalamic and hippocampal resting-state functional connectivity in youth with 22q11. 2 deletions. *Journal of Neuroscience*, *39*(7), 1301–1319.

Schmidt, B., Duin, A. A., & Redish, A. D. (2019). Disrupting the medial prefrontal cortex alters hippocampal sequences during deliberative decision making. *Journal of Neurophysiology*, *121*(6), 1981–2000.

Schwarz, A. J., Gass, N., Sartorius, A., Risterucci, C., Spedding, M., Schenker, E., Meyer-Lindenberg, A., & Weber-Fahr, W. (2013). Anti-correlated cortical networks of intrinsic connectivity in the rat brain. *Brain*

Connectivity, *3*(5), 503–511.

Schwarz, A. J., Gozzi, A., Chessa, A., & Bifone, A. (2012). Voxel scale complex networks of functional connectivity in the rat brain: neurochemical state dependence of global and local topological properties. *Computational and Mathematical Methods in Medicine*, *2012*.

Scott-Van Zeeland, A. A., Abrahams, B. S., Alvarez-Retuerto, A. I., Sonnenblick, L. I., Rudie, J. D., Ghahremani, D., Mumford, J. A., Poldrack, R. A., Dapretto, M., Geschwind, D. H., & Bookheimer, S. Y. (2010). Altered Functional Connectivity in Frontal Lobe Circuits Is Associated with Variation in the Autism Risk Gene CNTNAP2. *Science Translational Medicine*, *2*(56), 56ra80-56ra80. https://doi.org/10.1126/scitranslmed.3001344

Selimbeyoglu, A., Kim, C. K., Inoue, M., Lee, S. Y., Hong, A. S. O. O., Kauvar, I., Ramakrishnan, C., Fenno, L. E., Davidson, T. J., Wright, M., & Deisseroth, K. (2017). Modulation of prefrontal cortex excitation/inhibition balance rescues social behavior in CNTNAP2 -deficient mice. *Science Translational Medicine*, *9*(401), eaah6733. https://doi.org/10.1126/scitranslmed.aah6733

Sforazzini, F., Bertero, A., Dodero, L., David, G., Galbusera, A., Scattoni, M. L., Pasqualetti, M., & Gozzi, A. (2016). Altered functional connectivity networks in acallosal and socially impaired BTBR mice. *Brain Structure and Function*, *221*(2), 941–954. https://doi.org/10.1007/s00429-014-0948-9

Sforazzini, F., Schwarz, A. J., Galbusera, A., Bifone, A., & Gozzi, A. (2014). Distributed BOLD and CBV-weighted resting-state networks in the mouse brain. *NeuroImage*, *87*, 403–415. https://doi.org/10.1016/j.neuroimage.2013.09.050

Siegel, J. S., Ramsey, L. E., Snyder, A. Z., Metcalf, N. V, Chacko, R. V, Weinberger, K., Baldassarre, A., Hacker, C. D., Shulman, G. L., & Corbetta, M. (2016). Disruptions of network connectivity predict impairment in multiple behavioral domains after stroke. *Proceedings of the National Academy of Sciences*, *113*(30), E4367–E4376.

Sohal, V. S., Zhang, F., Yizhar, O., & Deisseroth, K. (2009). Parvalbumin neurons and gamma rhythms enhance cortical circuit performance. *Nature*, *459*(7247), 698–702. https://doi.org/10.1038/nature07991

Stachniak, T. J., Ghosh, A., & Sternson, S. M. (2014). Chemogenetic Synaptic Silencing of Neural Circuits Localizes a Hypothalamus→Midbrain Pathway for Feeding Behavior. *Neuron*, *82*(4), 797–808. https://doi.org/10.1016/j.neuron.2014.04.008

Stafford, J. M., Jarrett, B. R., Miranda-Dominguez, O., Mills, B. D., Cain, N., Mihalas, S., Lahvis, G. P., Lattal, K. M., Mitchell, S. H., & David, S. V. (2014). Large-scale topology and the default mode network in the mouse connectome. *Proceedings of the National Academy of Sciences*, *111*(52), 18745–18750.

Stenroos, P., Paasonen, J., Salo, R. A., Jokivarsi, K., Shatillo, A., Tanila, H., & Gröhn, O. (2018). Awake Rat Brain Functional Magnetic Resonance Imaging Using Standard Radio Frequency Coils and a 3D Printed Restraint Kit . In *Frontiers in Neuroscience* (Vol. 12). https://www.frontiersin.org/article/10.3389/fnins.2018.00548

Sternson, S. M., & Roth, B. L. (2014). Chemogenetic Tools to Interrogate Brain Functions. *Annual Review of Neuroscience*, *37*(1), 387–407. https://doi.org/10.1146/annurev-neuro-071013-014048

Strens, L. H. A., Oliviero, A., Bloem, B. R., Gerschlager, W., Rothwell, J. C., & Brown, P. (2002). The effects of subthreshold 1 Hz repetitive TMS on cortico-cortical and interhemispheric coherence. *Clinical Neurophysiology*, *113*(8), 1279–1285.

Suárez, L. E., Markello, R. D., Betzel, R. F., & Misic, B. (2020). Linking structure and function in macroscale brain networks. *Trends in Cognitive Sciences*, *24*(4), 302–315.

Supekar, K., Uddin, L. Q., Khouzam, A., Phillips, J., Gaillard, W. D., Kenworthy, L. E., Yerys, B. E., Vaidya, C. J., & Menon, V. (2013). Brain Hyperconnectivity in Children with Autism and its Links to Social Deficits. *Cell Reports*, *5*(3), 738–747. https://doi.org/10.1016/j.celrep.2013.10.001

Tasic, B., Menon, V., Nguyen, T. N., Kim, T. K., Jarsky, T., Yao, Z., Levi, B., Gray, L. T., Sorensen, S. A., Dolbeare, T., Bertagnolli, D., Goldy, J., Shapovalova, N., Parry, S., Lee, C., Smith, K., Bernard, A., Madisen, L., Sunkin, S. M., … Zeng, H. (2016). Adult mouse cortical cell taxonomy revealed by single cell transcriptomics. *Nature Neuroscience*, *19*(2), 335–346. https://doi.org/10.1038/nn.4216

Trakoshis, S., Rocchi, F., Canella, C., You, W., Chakrabarti, B., Ruigrok, A. N. V. V, Bullmore, E. T., Suckling, J., Markicevic, M., Zerbi, V., Martínez-Cañada, P., Rocchi, F., Canella, C., You, W., Chakrabarti, B., Ruigrok, A. N. V. V, Bullmore, E. T., Suckling, J., Markicevic, M., … Lombardo, M. V. (2020). Intrinsic excitation-inhibition imbalance affects medial prefrontal cortex differently in autistic men versus women. *ELife*, *9*, 1–31. https://doi.org/10.7554/eLife.55684

Tremblay, R., Lee, S., & Rudy, B. (2016). GABAergic Interneurons in the Neocortex: From Cellular Properties to Circuits. *Neuron*, *91*(2), 260–292. https://doi.org/10.1016/j.neuron.2016.06.033

Tu, W., Ma, Z., Ma, Y., Dopfel, D., & Zhang, N. (2020). Suppressing Anterior Cingulate Cortex Modulates Default Mode Network and Behavior in Awake Rats. *Cerebral Cortex*, *31*(January), 312–323. https://doi.org/10.1093/cercor/bhaa227

Turchi, J., Chang, C., Frank, Q. Y., Russ, B. E., David, K. Y., Cortes, C. R., Monosov, I. E., Duyn, J. H., Leopold, D. A., Ye, F. Q., Russ, B. E., Yu, D. K., Cortes, C. R., Monosov, I. E., Duyn, J. H., & Leopold, D. A. (2018). The Basal Forebrain Regulates Global Resting-State fMRI Fluctuations. *Neuron*, *97*(4), 940-952.e4.

https://doi.org/10.1016/j.neuron.2018.01.032

Tyszka, J. M., Kennedy, D. P., Adolphs, R., & Paul, L. K. (2011). Intact bilateral resting-state networks in the absence of the corpus callosum. *Journal of Neuroscience*, *31*(42), 15154–15162.

Uddin, L. Q., Clare Kelly, A. M., Biswal, B. B., Xavier Castellanos, F., & Milham, M. P. (2009). Functional connectivity of default mode network components: correlation, anticorrelation, and causality. *Human Brain Mapping*, *30*(2), 625–637.

Urban-Ciecko, J., & Barth, A. L. (2016). Somatostatin-expressing neurons in cortical networks. *Nature Reviews Neuroscience*, *17*(7), 401–409. https://doi.org/10.1038/nrn.2016.53

Van Den Heuvel, M. P., Hulshoff Pol, H. E., & Pol, H. E. H. (2010). Exploring the brain network: a review on resting-state fMRI functional connectivity. *European Neuropsychopharmacology*, *20*(8), 519–534. https://doi.org/10.1016/J.EURONEURO.2010.03.008

Van Kerkoerle, T., Self, M. W., Dagnino, B., Gariel-Mathis, M.-A., Poort, J., Van Der Togt, C., & Roelfsema, P. R. (2014). Alpha and gamma oscillations characterize feedback and feedforward processing in monkey visual cortex. *Proceedings of the National Academy of Sciences*, *111*(40), 14332–14341.

Vasa, R. A., Mostofsky, S. H., & Ewen, J. B. (2016). The Disrupted Connectivity Hypothesis of Autism Spectrum Disorders: Time for the Next Phase in Research. *Biological Psychiatry: Cognitive Neuroscience and Neuroimaging*, *1*(3), 245–252. https://doi.org/10.1016/j.bpsc.2016.02.003

Vassilvitskii, S., & Arthur, D. (2006). k-means++: The advantages of careful seeding. *Proceedings of the Eighteenth Annual ACM-SIAM Symposium on Discrete Algorithms*, 1027–1035.

Vincent, J. L., Patel, G. H., Fox, M. D., Snyder, A. Z., Baker, J. T., Van Essen, D. C., Zempel, J. M., Snyder, L. H., Corbetta, M., & Raichle, M. E. (2007). Intrinsic functional architecture in the anaesthetized monkey brain. *Nature*, *447*(7140), 83–86. https://doi.org/10.1038/nature05758

Vogt, B. A., & Paxinos, G. (2014). Cytoarchitecture of mouse and rat cingulate cortex with human homologies. *Brain Structure and Function*, *219*(1), 185–192. https://doi.org/10.1007/s00429-012-0493-3

Wang, Liang, Saalmann, Y. B., Pinsk, M. A., Arcaro, M. J., & Kastner, S. (2012). Electrophysiological low-frequency coherence and cross-frequency coupling contribute to BOLD connectivity. *Neuron*, *76*(5), 1010–1020.

Wang, Lin, Hermens, D. F., Hickie, I. B., & Lagopoulos, J. (2012). A systematic review of resting-state functional-MRI studies in major depression. *Journal of Affective Disorders*, *142*(1–3), 6–12.

Wang, X., Zhang, C., Szábo, G., & Sun, Q.-Q. (2013). Distribution of CaMKIIα expression in the brain in vivo, studied by CaMKIIα-GFP mice. *Brain Research*, *1518*(18), 9–25. https://doi.org/10.1016/j.brainres.2013.04.042

Wang, Z., Chen, L. M., Négyessy, L., Friedman, R. M., Mishra, A., Gore, J. C., & Roe, A. W. (2013). The relationship of anatomical and functional connectivity to resting-state connectivity in primate somatosensory cortex. *Neuron*, *78*(6), 1116–1126.

Watakabe, A., Ohtsuka, M., Kinoshita, M., Takaji, M., Isa, K., Mizukami, H., Ozawa, K., Isa, T., & Yamamori, T. (2015). Comparative analyses of adeno-associated viral vector serotypes 1, 2, 5, 8 and 9 in marmoset, mouse and macaque cerebral cortex. *Neuroscience Research*, *93*, 144–157. https://doi.org/10.1016/j.neures.2014.09.002

Watanabe, T., Hanajima, R., Shirota, Y., Ohminami, S., Tsutsumi, R., Terao, Y., Ugawa, Y., Hirose, S., Miyashita, Y., & Konishi, S. (2014). Bidirectional effects on interhemispheric resting-state functional connectivity induced by excitatory and inhibitory repetitive transcranial magnetic stimulation. *Human Brain Mapping*, *35*(5), 1896–1905.

Wei, M., Qin, J., Yan, R., Li, H., Yao, Z., & Lu, Q. (2013). Identifying major depressive disorder using Hurst exponent of resting-state brain networks. *Psychiatry Research: Neuroimaging*, *214*(3), 306–312. https://doi.org/https://doi.org/10.1016/j.pscychresns.2013.09.008

Welch, P. (1967). The use of fast Fourier transform for the estimation of power spectra: a method based on time averaging over short, modified periodograms. *IEEE Transactions on Audio and Electroacoustics*, *15*(2), 70–73.

Whitesell, J. D., Liska, A., Coletta, L., Hirokawa, K. E., Bohn, P., Williford, A., Groblewski, P. A., Graddis, N., Kuan, L., Knox, J. E., Ho, A., Wakeman, W., Nicovich, P. R., Nguyen, T. N., van Velthoven, C. T. J., Garren, E., Fong, O., Naeemi, M., Henry, A. M., … Harris, J. A. (2021). Regional, Layer, and Cell-Type-Specific Connectivity of the Mouse Default Mode Network. *Neuron*, *109*(3), 545-559.e8. https://doi.org/10.1016/j.neuron.2020.11.011

Wiegert, J. S., Mahn, M., Prigge, M., Printz, Y., & Yizhar, O. (2017). Silencing Neurons: Tools, Applications, and Experimental Constraints. *Neuron*, *95*(3), 504–529. https://doi.org/10.1016/j.neuron.2017.06.050

Wu, G.-R., Liao, W., Stramaglia, S., Ding, J.-R., Chen, H., & Marinazzo, D. (2013). A blind deconvolution approach to recover effective connectivity brain networks from resting state fMRI data. *Medical Image Analysis*, *17*(3), 365–374.

Xue, M., Atallah, B. V., & Scanziani, M. (2014). Equalizing excitation-inhibition ratios across visual cortical

neurons. *Nature*, *511*(7511), 596–600. https://doi.org/10.1038/nature13321

Yeo, B. T. T., Krienen, F. M., Sepulcre, J., Sabuncu, M. R., Lashkari, D., Hollinshead, M., Roffman, J. L., Smoller, J. W., Zöllei, L., Polimeni, J. R., Fischl, B., Liu, H., & Buckner, R. L. (2011). The organization of the human cerebral cortex estimated by intrinsic functional connectivity. *Journal of Neurophysiology*, *106*(3), 1125–1165. https://doi.org/10.1152/jn.00338.2011

Yizhar, O., Fenno, L. E., Prigge, M., Schneider, F., Davidson, T. J., O'Shea, D. J., Sohal, V. S., Goshen, I., Finkelstein, J., Paz, J. T., Stehfest, K., Fudim, R., Ramakrishnan, C., Huguenard, J. R., Hegemann, P., & Deisseroth, K. (2011). Neocortical excitation/inhibition balance in information processing and social dysfunction. *Nature*, *477*(7363), 171–178. https://doi.org/10.1038/nature10360

Zeisel, A., Muñoz-Manchado, A. B., Codeluppi, S., Lönnerberg, P., La Manno, G., Juréus, A., Marques, S., Munguba, H., He, L., Betsholtz, C., Rolny, C., Castelo-Branco, G., Hjerling-Leffler, J., & Linnarsson, S. (2015). Brain structure. Cell types in the mouse cortex and hippocampus revealed by single-cell RNA-seq. *Science (New York, N.Y.)*, *347*(6226), 1138–1142. https://doi.org/10.1126/science.aaa1934

Zerbi, V., Pagani, M., Markicevic, M., Matteoli, M., Pozzi, D., Fagiolini, M., Bozzi, Y., Galbusera, A., Scattoni, M. L., Provenzano, G., Banerjee, A., Helmchen, F., Basson, M. A., Ellegood, J., Lerch, J. P., Rudin, M., Gozzi, A., & Wenderoth, N. (2021). Brain mapping across 16 autism mouse models reveals a spectrum of functional connectivity subtypes. *Molecular Psychiatry*, *June*. https://doi.org/10.1038/s41380-021-01245-4

Zhao, W., Luo, L., Li, Q., & Kendrick, K. M. (2013). What can psychiatric disorders tell us about neural processing of the self? *Frontiers in Human Neuroscience*, *7*, 485.

Zhu, H., & Roth, B. L. (2015). DREADD: a chemogenetic GPCR signaling platform. *The International Journal of Neuropsychopharmacology / Official Scientific Journal of the Collegium Internationale Neuropsychopharmacologicum (CINP)*, *18*(1), 1–6. https://doi.org/10.1093/ijnp/pyu007

Zikopoulos, B., & Barbas, H. (2013). Altered neural connectivity in excitatory and inhibitory cortical circuits in autism. *Frontiers in Human Neuroscience*, *7*(September), 1–24. https://doi.org/10.3389/fnhum.2013.00609

Appendix I

Title: Intrinsic excitation-inhibition imbalance affects medial prefrontal cortex differently in autistic men versus women

Authors: Stavros Trakoshis[1,2]*, Pablo Martínez-Cañada[3,4]*, Federico Rocchi[5], Carola Canella[5], Wonsang You[6], Bhismadev Chakrabarti[7,8], Amber N. V. Ruigrok[7], Edward T. Bullmore[9,10], John Suckling[10], Marija Markicevic[11,12], Valerio Zerbi[11,12], MRC AIMS Consortium†, Simon Baron-Cohen[7,9], Alessandro Gozzi[5]**, Meng-Chuan Lai[7,13,14,15,16]**, Stefano Panzeri[3]**, & Michael V. Lombardo[1,7]**

Affiliations:

1 Laboratory for Autism and Neurodevelopmental Disorders, Center for Neuroscience and Cognitive Systems @UniTn, Istituto Italiano di Tecnologia, Corso Bettini, 31, 38068 Rovereto, Italy

2 Department of Psychology, University of Cyprus, Nicosia, Cyprus

3 Neural Computation Laboratory, Center for Neuroscience and Cognitive Systems @UniTn, Istituto Italiano di Tecnologia, Corso Bettini, 31, 38068 Rovereto, Italy

4 Optical Approaches to Brain Function Laboratory, Department of Neuroscience and Brain Technologies, Istituto Italiano di Tecnologia, Via Morego 30, 16163 Genova, Italy

5 Functional Neuroimaging Laboratory, Center for Neuroscience and Cognitive Systems @UniTn, Istituto Italiano di Tecnologia, Corso Bettini 31, 38068 Rovereto, Italy

6 Artificial Intelligence and Image Processing Laboratory, Department of Information and Communications Engineering, Sun Moon University, South Korea

7 Autism Research Centre, Department of Psychiatry, University of Cambridge, Cambridge, United Kingdom

8 Centre for Integrative Neuroscience and Neurodynamics, School of Psychology and Clinical Language Sciences, University of Reading, Reading, United Kingdom

9 Cambridgeshire and Peterborough National Health Service Foundation Trust, Cambridge, United Kingdom

10 Brain Mapping Unit, Department of Psychiatry, University of Cambridge, Cambridge, United Kingdom

11 Neural Control of Movement Lab, D-HEST, ETH Zurich, Auguste-Piccard-Hof 1, 8093 Zurich, Switzerland

12 Neuroscience Center Zurich, University and ETH Zurich, Winterthurerstrasse 190, 8057 Zurich, Switzerland

13 The Margaret and Wallace McCain Centre for Child, Youth & Family Mental Health, Azrieli Adult Neurodevelopmental Centre, and Campbell Family Mental Health Research Institute, Centre for Addiction and Mental Health, Toronto, Canada

14 Department of Psychiatry and Autism Research Unit, The Hospital for Sick Children, Toronto, Canada

15 Department of Psychiatry, Faculty of Medicine, University of Toronto, Toronto, Canada

16 Department of Psychiatry, National Taiwan University Hospital and College of Medicine, Taipei, Taiwan

* Equal first author contributions

** Equal senior author contributions

Corresponding Author: Michael V. Lombardo (michael.lombardo@iit.it)

† MRC AIMS Consortium Author List (Alphabetical Order)

Anthony J. Bailey (Oxford), Simon Baron-Cohen (Cambridge), Patrick F Bolton (IoPPN), Edward T. Bullmore (Cambridge), Sarah Carrington (Oxford), Marco Catani (IoPPN), Bhismadev Chakrabarti (Cambridge), Michael C. Craig (IoPPN), Eileen M. Daly (IoPPN), Sean C. L. Deoni (IoPPN), Christine Ecker (IoPPN), Francesca Happé (IoPPN), Julian Henty (Cambridge), Peter Jezzard (Oxford), Patrick Johnston (IoPPN), Derek K. Jones (IoPPN), Meng-Chuan Lai (Cambridge), Michael V. Lombardo (Cambridge), Anya Madden (IoPPN), Diane Mullins (IoPPN), Clodagh M. Murphy (IoPPN), Declan G. M. Murphy (IoPPN), Greg Pasco (Cambridge), Amber N. V. Ruigrok (Cambridge), Susan A. Sadek (Cambridge), Debbie Spain (IoPPN), Rose Stewart (Oxford), John Suckling (Cambridge), Sally J. Wheelwright (Cambridge) and Steven C. Williams (IoPPN).

Abstract

Excitation-inhibition (E:I) imbalance is theorized as an important pathophysiological mechanism in autism. Autism affects males more frequently than females and sex-related mechanisms (e.g., X-linked genes, androgen hormones) can influence E:I balance. This suggests that E:I imbalance may affect autism differently in males versus females. With a combination of *in-silico* modeling and *in-vivo* chemogenetic manipulations in mice, we first show that a time-series metric estimated from fMRI BOLD signal, the Hurst exponent (H), can be an index for underlying change in the synaptic E:I ratio. In autism we find that H is reduced, indicating increased excitation, in the medial prefrontal cortex (MPFC) of autistic males but not females. Increasingly intact MPFC H is also associated with heightened ability to behaviorally camouflage social-communicative difficulties, but only in autistic females. This work suggests that H in BOLD can index synaptic E:I ratio and that E:I imbalance affects autistic males and females differently.

Keywords: autism; heterogeneity; excitation; inhibition; fMRI; Hurst exponent; DREADD; sex/gender; camouflaging

Excitation-inhibition (E:I) balance in the brain has been hypothesized to be atypical in many neuropsychiatric conditions[1,2], including autism. Rubenstein and Merzenich originally suggested that some types of autism may be explained by an E:I imbalance that may lead to hyper-excitability in cortical circuitry and potentially enhanced levels of neuronal noise[1]. However, coming to a better understanding of how E:I balance is affected across a heterogeneous mixture of autistic individuals has proven to be challenging because of the limited availability of robust E:I biomarkers that are non-invasive and applicable in humans and which can be measured on a large scale. A majority of the literature about E:I balance in autism extends from investigations of prominent single gene mutations associated with autism and the animal model research around these genes[2,3]. This leaves a significant gap in evaluating the E:I theory on a larger majority of the autistic population. While no one theory can fully explain all individuals with an autism diagnosis[4,5], the E:I imbalance theory may have utility for understanding subtypes of autistic individuals[6–8].

Sex/gender may be an important stratifier of relevance for highlighting E:I imbalance subtypes[9,10]. Many highly penetrant autism-associated genes are located on the sex chromosomes (e.g., *FMR1*, *MECP2*, *NLGN3*, *GABRA3*, *ARX*, *SYN1*) and are known to lead to pathophysiology implicating E:I dysregulation[1,11,12]. Other genes playing important roles in the balance between excitation and inhibition in the brain (e.g., *MEF2C, GRIK2, GRIA1, SCN3A, SCN9A, NPTX2*) are highly sensitive to androgens in human neuronal stem cells and are highly expressed in 'social brain' circuitry such as the default mode network, and in particular, the medial prefrontal cortex (MPFC)[13]. Optogenetic stimulation to enhance excitation in mouse MPFC also results in changes in social behavior[14,15]. These results hint that sex-relevant biological mechanisms affect E:I balance and that key social brain regions such as MPFC may be of particular importance for explaining how E:I imbalance affects social behavior. Sex/gender heterogeneity also leads to differing clinical presentations and compensatory mechanisms in autism that may depend on E:I balance in MPFC. It is known that many cognitively able adult autistic women engage in camouflaging behaviors that tend to compensate or mask their social-communicative difficulties moreso than autistic men[16–18]. Prior work has shown that whereas autistic males show reduced ventral MPFC (vMPFC) self-representation response, autistic females show intact vMPFC self-representation. Furthermore, the degree to which vMPFC shows intact self-representation response in autistic females is associated with enhanced ability to camouflage[19]. If E:I imbalance asymmetrically affects vMPFC function in males versus females, this could help explain differential camouflaging in adult autistic females.

To better understand sex-specific E:I imbalance in autism we need better neuroimaging biomarkers that index underlying synaptic E:I mechanisms and which can be deployed on a large-scale for in-vivo investigation in deeply phenotyped cohorts. Here we pursue the idea that spectral properties of neural time-series data (e.g., local field potentials (LFP) or blood oxygen level dependent (BOLD) signal) could be used to isolate such biomarkers. It has been long known that LFP and resting state fMRI (rsfMRI) data exhibits rich spectral properties, with power decreasing as function of frequency[20–24]. Models of neural networks have reported that the E:I ratio has profound effects on the spectral shape of electrophysiological activity[25–27]. Recent work with simplified models has proposed that the exponent of the 1/f spectral power law, an index closely related to H, reflects the extent of E:I imbalance[28]. This suggest that neurophysiologically heightened E:I ratio generates flatter 1/f slope in LFP data and this could drive H (as measured in BOLD) to be decreased. In past work we have shown that a metric related to 1/f slope, the Hurst exponent (H), is atypically decreased in rsfMRI data of adult autistic males, particularly for social brain areas like MPFC[29]. H is statistically

relevant for the concept of 'neural noise' since lower levels of H can be interpreted as closer to what would be expected of a completely noisy random signal (e.g., white noise produces an H = 0.5). Related to H and long-memory characteristics of the rsfMRI time-series, prior work has also shown case-control differences in the intrinsic neural timescale in autism (e.g., magnitude of temporal autocorrelation)[30]. However, these prior studies examine primarily male-dominated samples and thus cannot shed insight into sex-related heterogeneity in autism.

In this work we aim to better understand how E:I imbalance may differentially affect autistic males and females. To achieve this aim, we first took a bottom-up approach by using *in-silico* (i.e. computational) models of local neuronal microcircuitry to make predictions about how H and 1/f slope in local field potentials (LFP) and rsfMRI data may behave when there are underlying changes in E:I balance. Importantly, our approach takes a major step forward from prior work[28] by utilizing a model that includes interactions within and between excitatory and inhibitory neuronal populations. Next, our *in-silico* predictions are then tested *in-vivo* with a combination of rsfMRI and experimental manipulations in mice that either increase neurophysiological excitation or that silence the local activity in the network. Chemogenetic (i.e. designer receptors exclusively activated by designer drugs; DREADD) or optogenetic manipulations are optimally suited to these purposes, owing to the possibility of enabling remote control of neuronal excitability with cell-type and regional specificity[14,31]. Manipulations of neuronal activity like these in animals are key for two reasons. First, they allow for experimental *in-vivo* confirmation of *in-silico* predictions. Second, such work is a key translational link across species (i.e. rodents to humans), given the common use of neuroimaging readouts from rsfMRI[32]. At the genomic level we then examine what cell types could possibly underlie sex-related heterogeneity in E:I imbalance. Finally, we then turn to the human rsfMRI data to show how E:I imbalance may differ amongst autistic males and females and how such mechanisms may explain individual differences in camouflaging behavior.

Results

Analysis of E:I balance in simulated LFPs from a recurrent network model

In a bottom-up fashion, we first worked to identify potential biomarkers of E:I imbalance from neural time-series data such as local field potentials (LFPs). Motivating our *in-silico* modeling of E:I effects on LFP and BOLD data, we note prior work by Gao and colleagues[28]. This prior work simulated LFP time-series from non-interacting excitatory and inhibitory neuronal populations (Figure 1 – figure supplement 1A) and showed that spectral properties such as the 1/f slope flatten with increasing E:I ratio (Figure 1 – figure supplement 1B). Given the relationship between 1/f slope and H[33], we show within this modeling approach that as E:I ratio increases, H decreases (Figure 1 – figure supplement 1C). However, a limitation of this prior work is that it does not include interactions between excitatory and inhibitory populations nor does it allow for recurrent connections within such populations.

To address these limitations, we developed a more biologically plausible recurrent network model of interacting excitatory and inhibitory integrate-and-fire neuronal populations that receive

external inputs (both a sensory driven thalamic input and a sensory unrelated intracortical input) (Figure 1A; see Methods for more details). From this model, we computed the network's LFP as the sum of absolute values of all synaptic currents. The absolute value is taken because AMPA synapses are usually apical and GABA synapse are peri-somatic and thus their dipoles sum with the same sign along dendrites[26,34,35]. We computed LFP summing presynaptic currents from both external inputs and recurrent interactions, as real LFPs capture both sources of synaptic activity[36]. We have extensively validated this method of computing LFPs from integrate-and-fire networks in previous work on both real cortical data and simulations with networks of realistically-shaped 3D neurons and shown that it works better than when using alternatives such as the sum of simulated membrane potentials, the signed sum of synaptic currents or a time integration of the spike rate[26,37]. In this *in-silico* network, we manipulated the E:I ratio by independently varying the strengths of the inhibitory (g_I) and excitatory (g_E) synaptic conductances. We called *g* the relative ratio between inhibitory and excitatory conductances ($g = g_I/g_E$). We report simulation results for two levels of strength of thalamic input (υ_0 = 1.5 spikes/second and υ_0 = 2 spikes/second), and we verified that our results hold qualitatively for a wider range of input levels (1.5 to 4 spikes/second).

Figures 1B-C show examples of LFP time-series and power spectral densities (PSDs) for two values of g, one within an excitation-dominated regime (g = 5.6) and the other within an inhibition-dominated regime (g = 14.8). The spectral profiles (Figure 1C) display two different regions of frequencies with different spectral properties: a region of steeper negative 1/f slopes at higher frequencies (> 30 Hz) and a region of shallower (small negative and sometimes positive) slopes at low frequencies (< 30 Hz). Thus, we calculated slopes for the low- and high-frequency regions with piecewise regressions of log power predicted by log frequency. Slopes from the low-frequency (Figure 1D) and high-frequency region (Figure 1E) increase when g is reduced (i.e. E:I ratio augmented). This means that lower values of g correspond to faster spectra with relatively more power at higher frequencies. Changes in slopes are more prominent in the excitation-dominated region where g is smaller (that is, E:I ratio is shifted in favor of E) than the reference value (g = 11.3), which has been shown to be a plausible reference value that reproduces cortical power spectra well[26,34,37–40]. An increase in g beyond this reference value (shifting the E:I balance towards stronger inhibition) had a weaker effect on slopes. Similar results were obtained when quantifying 1/f slope using the FOOOF algorithm[41] (Figure 1 – figure supplement 2), indicating that slopes are not biased by the particular piecewise linear fit procedure. Next, we computed H from the same simulated LFPs. As expected, H decreases with decreasing g (i.e. increasing E:I ratio), but only when g is below the baseline reference value (Figure 1F). These results clearly indicate that, in a biologically plausible computational model of local cortical microcircuitry including recurrent connections between excitatory and inhibitory neuronal populations, changes in synaptic E:I ratio are reflected by and thus could be inferred from the overall LFP readout of 1/f slope or H.

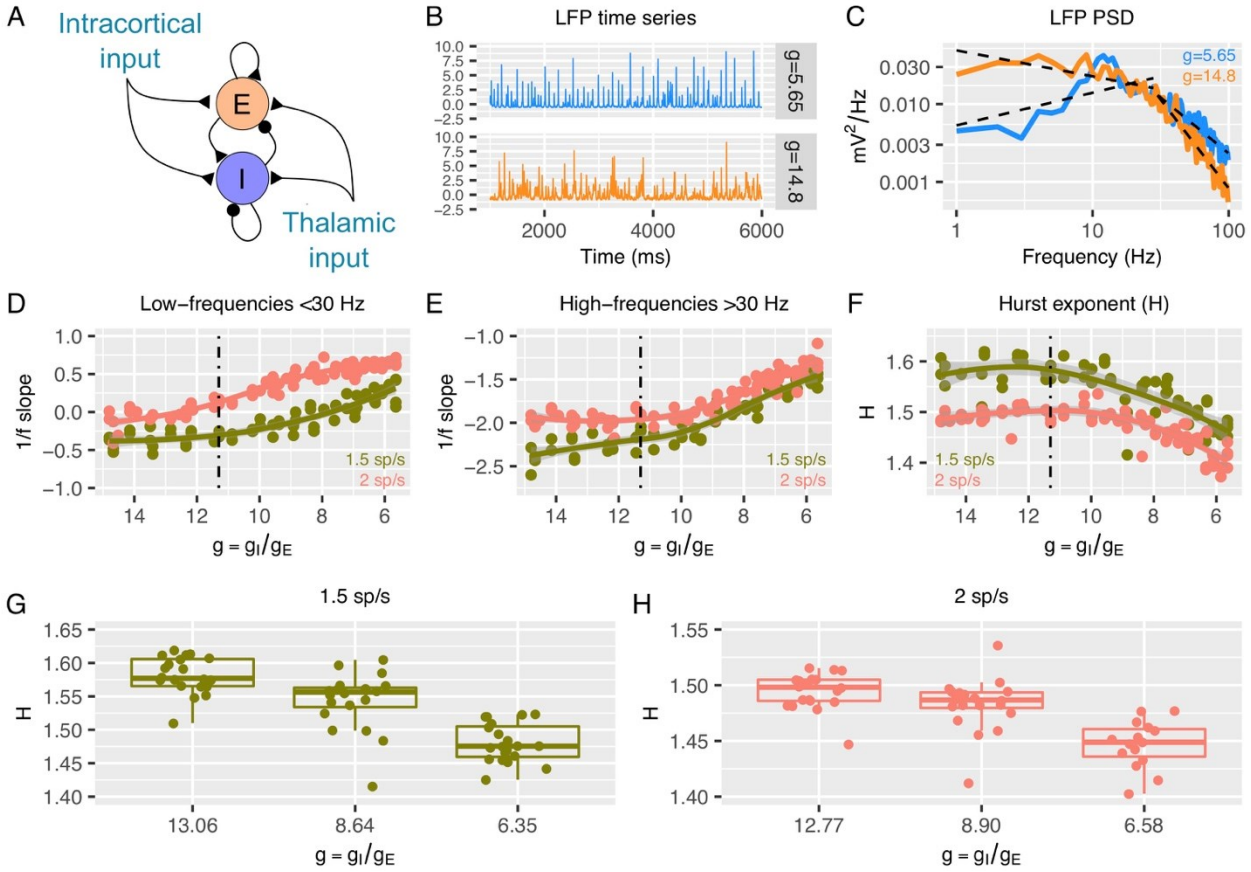

Figure 1: Predictions from a recurrent network model of how the low- and high-frequency slopes of the LFP power spectrum and H change with the variation in relative ratio of inhibitory and excitatory synaptic conductances. *Panel A shows a sketch of the point-neuron network that includes recurrent connections between two types of populations: excitatory cells (E) and inhibitory cells (I). Each population receives two types of external inputs: intracortical activity and thalamic stimulation. Panels B and C show examples of normalized LFP times series and their corresponding PSDs generated for two different ratios between inhibitory and excitatory conductances ($g = g_I/g_E$). The low- and high-frequency slopes of the piecewise regression lines that fit the log-log plot of the LFP PSDs are computed over two different frequency ranges (1-30 Hz for the low-frequency slope and 30 - 100 Hz for the high-frequency slope). The relationship between low-frequency slopes (panel D), high-frequency slopes (panel E) and H values (panel F) are plotted as a function of g for two different firing rates of thalamic input (1.5 and 2 spikes/second). The reference value of g (which has shown in previous studies to reproduce cortical data well) is represented by a dashed black line. In panel G and H, we show H values in 3 different groups of g (high, medium and low g), with the same number of samples in each group.*

Simulated BOLD signal tracks with changes in E:I ratio and correlates selectively with LFP power bands

Given that E:I ratio in LFP data is related to 1/f slope and H, we next asked whether simulated fMRI BOLD signal from the recurrent model would also show similar relationships. To answer this question, we first had to simulate BOLD data from the LFP data generated from the recurrent model. Our approach to simulating BOLD (see Methods and Figure 2 – figure supplement 1 for how BOLD was simulated from LFP), captures several key characteristics about the empirical relationship between LFP and BOLD. Studies with simultaneous LFP and BOLD measured in animals have shown

that although BOLD signal correlates with both LFPs and spikes, it correlates more strongly with the LFP than with spikes[42–46]. Further studies with simultaneous LFP and BOLD measured in non-human primates[42,43,47] have considered the relationship between frequency-resolved LFPs and BOLD and indicate that LFP power shows time-lagged correlations with the time course of BOLD signal and that different frequency bands vary in how they correlate with measured BOLD signal. In particular, gamma band frequencies tend to show the strongest correlation between LFP power and BOLD signal. Frequency dependency of the EEG-BOLD relationship, with prominent predictive power of the gamma band, is also reported in humans[48]. Remarkably, these empirical observations are recapitulated with simulated LFP and BOLD data from the recurrent model. Figure 2A shows time-lagged correlations between time-dependent LFP power and BOLD. Figure 2B shows that all considered LFP frequency bands (e.g., alpha, beta, gamma) correlate with BOLD, but with the gamma band showing the strongest correlations. Thus, our method for simulating BOLD from recurrent model LFP data retains key empirical relationships observed between real LFP power and BOLD. Simulating BOLD with a simple hemodynamic response function (HRF) convolution of the LFP would have not respected the patterns of correlations between LFP power and BOLD observed in empirical data (i.e. the relative increase in correlation between the gamma band and BOLD with respect to other bands; Figure 2 – figure supplement 2).

With simulated BOLD from the recurrent model, we next computed H on these data to understand if E:I ratio in the recurrent model is associated with changes in H in BOLD. Strikingly, H in BOLD shows the same dependency on g as observed in LFP data (Figure 2C-D) - H in BOLD decreases as E:I ratio is shifted toward higher excitation by lowering the value of g with respect to the reference value. Although H in LFP and BOLD showed similar associations with respect to changes in g, it is notable that the range of H in BOLD is shifted towards smaller values (Figure 2C-D) than H in LFP (Figure 1G-H). We also verified that the dependency of H in BOLD on g was largely independent of the details of how BOLD is simulated from LFP. While the results shown in Figure 2 are computed with an HRF that reproduces the correlation function measured between the BOLD signal and the gamma band of LFP[43], it is notable that these results remained similar when using the canonical HRF instead (Figure 2 – figure supplement 2). Removing the high pass filter from simulation of BOLD response did alter the relative values of correlation between LFP power and BOLD across frequency bands, making the BOLD response more in disagreement with experimental data, but did not change the relationship of decreasing H with decreasing g (Figure 2 – figure supplement 2), suggesting that our conclusions are robust to the details of the model of the LFP to BOLD relationship. In sum, the inferences from the recurrent network model suggest that H in LFP and BOLD data can be utilized as a marker to track changes in underlying synaptic E:I mechanisms.

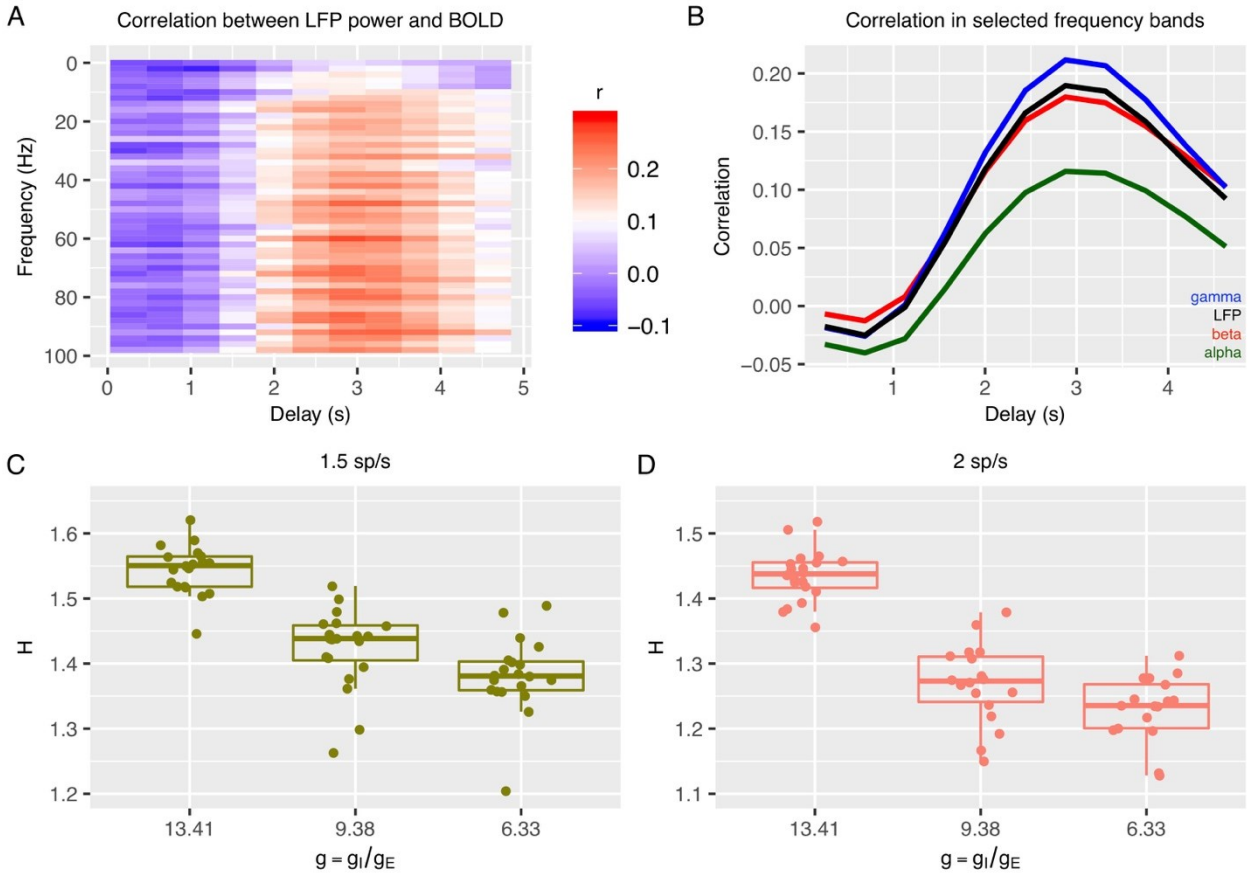

Figure 2: Relationship between E:I ratio from the recurrent model and H measured in simulated BOLD response. *Panel A shows time-lagged Pearson correlations between LFP power across a range of different frequencies and the BOLD signal. Panel B shows the correlation between LFP power and the BOLD signal in selected frequency bands. The following four LFP bands are considered: alpha (8 - 12 Hz), beta (15 - 30 Hz), gamma (40 - 100 Hz) and the total LFP power (0 - 100 Hz). The relationship between E:I ratio (g) and H in simulated BOLD is shown in panels C and D two different firing rates of thalamic input (1.5 and 2 spikes/second).*

Modeling the effects of chemogenetic manipulations within the recurrent network model

We next investigated manipulations of parameters within the recurrent model that approximate the effects of empirical chemogenetic DREADD manipulations in neurons. These simulations are useful to both gain a better understanding of the empirical BOLD measures under DREADD manipulations presented in the next section, and to better characterize the specificity of the origin of changes in 1/f slopes and H with the E:I ratio. Given that as shown above, in our models changes of H in BOLD mirror those in LFPs, here we present changes in model LFP spectra when simulating these DREADD manipulations.

We first studied the specific effect of solely increasing excitation within the recurrent network. This can be achieved experimentally by using the drug clozapine-N-oxide (CNO) on the DREADD receptor hM3Dq to increase the excitability of excitatory cells only[49]. We simulated this kind of increase of excitability of pyramidal cells in the recurrent network model by lowering their voltage

threshold (V_{th}) for spike initiation. Progressively lowering V_{th} from -52 to -53 mV resulted in more positive low-frequency and flatter high-frequency 1/f slopes (Figure 3 – figure supplement 1A) and also caused decreases in H (Figure 3A). For H, increasing V_{th} (i.e. decreasing excitability) from -52 to -51 mV resulted in little change in H. These results predict that specific increases of excitation, as in the application of the hM3Dq DREADD to enhance excitability of pyramidal neurons, should reduce steepness of the high-frequency slopes and lead to a decrease in H. These results also confirm our above findings that in recurrent networks in which excitatory and inhibitory neurons interact, increases in excitability are easier to detect from changes in 1/f slope or H than decreases in excitation.

To study whether the changes in 1/f slopes and H are specific to modulations in excitability of only excitatory neurons, we modeled the combined effect of silencing both excitatory and inhibitory neuronal populations. This silencing of both excitatory and inhibitory neurons can be obtained experimentally by application of the hM4Di DREADD (see next Section). In the recurrent network model, we simulated this silencing of both excitatory and inhibitory cells by decreasing the resting potential, E_L, in both excitatory and inhibitory neurons. Decreasing E_L from the baseline value of -70 to -75 mV produced varied effects in 1/f slopes (Figure 3 – figure supplement 1B) and resulted in a slight increase of H (Figure 3B). Note that a moderate increase in H with higher input (Figure 3B) was also found when comparing two very different levels of input. Given that a possible non-local action of hM4Di might lead to less excitatory input to the considered area coming from the silencing of nearby regions, this suggests that our conclusion should still hold even in the presence of some non-local DREADD effects. In general, the effects of simulating hM4Di DREADD were far less prominent than those reported above when simulating enhanced excitation specifically (Figure 3A and Figure 3 – figure supplement 1A). These results predict overall a very small effect of the hM4Di DREADD on H and 1/f slopes. These results also imply that decreases in H are more likely to result from specific increases in excitation rather than from non-specific decreases of excitability across both excitatory and inhibitory neuronal populations.

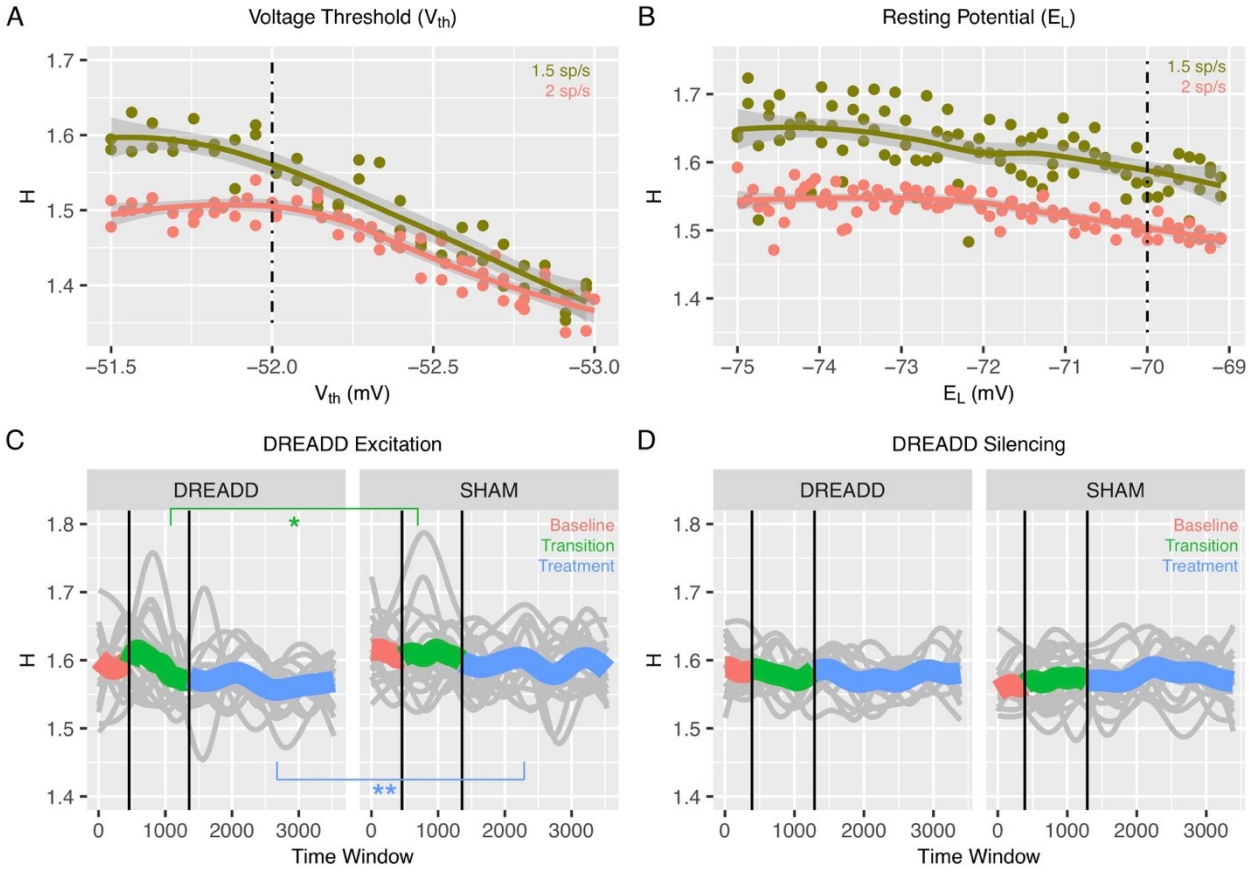

Figure 3: Changes to H after chemogenetic DREADD manipulations to enhance excitability or silence excitatory and inhibitory neurons. *Panel A shows how H changes after the voltage threshold for spike initiation in excitatory neurons (V_{th}) is reduced in the recurrent model, thereby enhancing excitability as would be achieved with hM3Dq DREADD manipulation. Panel B shows how H changes after decreasing the resting potential of excitatory and inhibitory neurons (E_L), as would be achieved with hM4Di DREADD manipulation. The voltage threshold for spike initiation in excitatory neurons (V_{th}) is reduced in the recurrent model, thereby silencing both excitatory and inhibitory neurons as would be achieved with hM4Di DREADD manipulation. Panel C shows changes in H in BOLD from prefrontal cortex (PFC) after real hM3Dq DREADD manipulation in mice, while panel D shows changes in PFC BOLD H after hM4Di DREADD manipulation in mice. In panels C and D, individual gray lines indicate H for individual mice, while the colored lines indicate Baseline (pink), Transition (green), and Treatment (blue) periods of the experiment. During the Baseline period H is measured before the drug or SHAM injection is implemented. The Transition phase is the period after injection but before the period where the drug has maximal effect. The Treatment phase occurs when the drug begins to exert its maximal effect. The green star indicates a Condition*Time interaction ($p<0.05$) in the Transition phase, whereas the blue stars indicate a main effect of Condition within the Treatment phase ($p < 0.005$).*

Changes in H in BOLD after chemogenetic manipulation to enhance excitability of excitatory neurons in mice

All of the results thus far report results from our *in-silico* model of recurrent neuronal networks and their readouts as simulated LFP or BOLD data. The *in-silico* modeling of BOLD data suggests that if E:I ratio is increased via enhanced excitability of excitatory neurons, then H should

decrease. To empirically test this prediction *in-vivo*, we measured rsfMRI BOLD signal in prefrontal cortex (PFC) of mice under conditions where a chemogenetic manipulation (hM3Dq DREADD)[49] is used to enhance excitability of pyramidal neurons. Here we used a sliding window analysis to assess dynamic changes in H over the course of 3 different phases of the experiment – 1) a 'Baseline' phase where the CNO drug or a SHAM injection had not yet occurred, 2) a 'Transition' phase directly following CNO or SHAM injection, and 3) a 'Treatment' phase, whereby CNO has its maximal effect. We find that H is modulated over time by the DREADD manipulation (condition*time*treatment phase interaction $F = 349.03$, $p < 0.0001$). During the Baseline phase of rsfMRI scanning before the DREADD-actuator CNO was injected, H under DREADD or a SHAM control conditions are not affected (condition main effect $F = 0.82$, $p = 0.37$; condition*time interaction $F = 0.36$, $p = 0.54$). However, during the Transition phase of the experiment where the CNO begins to have its effects, we find a condition*time interaction ($F = 4.94$, $p = 0.0262$), whereby H drops over time at a steeper rate during the DREADD condition compared to the SHAM condition (green line in Figure 3C). Finally, during the Treatment phase of the experiment, where the drug exerts its maximal effect, there is a significant main effect of condition ($F = 12.92$, $p = 0.0011$) and no condition*time interaction ($F = 0.66$, $p = 0.4182$) (blue line in Figure 3C) (Table 1). This effect is explained by H being reduced in the DREADD vs SHAM condition. These *in-vivo* results are directly in line with the *in-silico* prediction that enhancing E:I ratio via enhancing the excitability of excitatory neurons results in a decrease in H (i.e. Figure 1F-H, Figure 2C-D, and Figure 3A).

Chemogenetically silencing both excitatory and inhibitory neurons has no effect on H in BOLD

While the above results show that specific enhancement of excitability in excitatory neurons results in a decrease in BOLD H, it is an important negative control contrast to investigate whether non-specifically reducing the excitability of both excitatory and inhibitory neuronal populations might also affect H. This is an important negative control since if H were to change in a similar direction after this manipulation, it would make interpretations about decrease in H being due to increased E:I ratio via excitation problematic. The *in-silico* simulation of this manipulation (Figure 3B) would predict that H would not be changed much, and that if a change in H were to occur, it would be a slight increase rather than a decrease in H. By expressing the inhibitory hM4Di DREADD[50] under the control of a pan-neuronal promoter, we chemogenetically silenced both excitatory and inhibitory neurons in PFC of mice and re-ran the same rsfMRI neuroimaging protocol as before. While a significant 3-way interaction between condition, time, and treatment phase was present ($F = 85.8$, $p < 0.0001$), there were no strong main effects of condition or condition*time interactions in any of the baseline, transition, or treatment phases of the experiment (see Table 2 and Figure 3D). Overall, these results along with the recurrent model simulation of hM4Di DREADD (Figure 3B) bolster strength of the interpretation that enhanced excitation drives decreasing H in BOLD and that H in BOLD would not change appreciably in a situation such as pan-neuronal silencing of both excitatory and inhibitory neurons.

Consistent with the idea that heightened excitation leads to flattening of the 1/f slope and reductions in H, we also computed a measure of the fractional amplitude of low frequency fluctuations (fALFF)[51]. Given the effect of flattening 1/f slope, we expected that fALFF would show reductions due to the DREADD excitation manipulation but would show no effect for the DREADD silencing manipulation. These expectations were confirmed, as DREADD excitation results in a large

drop in fALFF, which shows a stark drop off midway through the transition phase and stays markedly lower throughout the treatment phase when the drug has its maximal effects. In contrast, similar effects do not occur for the DREADD silencing manipulation (see Figure 3 – figure supplement 2).

Autism-associated genes in excitatory neuronal cell types in the human brain are enriched for genes that are differentially expressed by androgen hormones

The *in-silico* and *in-vivo* animal model findings thus far suggest that excitation affects metrics computed on neural time-series data such as 1/f slope and H. Applied to the idea of sex-related heterogeneity in E:I imbalance in autism, these results make the prediction that excitatory neuronal cell types would be the central cell type affecting such neuroimaging phenotypes in a sex-specific manner. To test this hypothesis about sex-specific effects on excitatory neuronal cell types, we examined whether known autism-associated genes that affect excitatory neuronal cell types[52,53] are highly overlapping with differentially expressed genes in human neuronal stem cells when treated with a potent androgen hormone, dihydrotestosterone (DHT)[13,54]. Genes differentially expressed by DHT are highly prominent within the gene set of autism-associated genes that affect excitatory neurons (OR = 1.67, p = 0.03), with most of the overlapping genes being those whereby DHT upregulates expression (Figure 4A). By contrast, genes associated with autism that affect inhibitory neuronal cell types or other non-neuronal cells (e.g., microglia, astrocytes, oligdendrocytes) are not enriched for DHT differentially expressed genes (inhibitory neurons: OR = 1.51, p = 0.12; microglia: OR = 0.78, p = 0.78; astrocytes or oligodendrocytes: OR = 1.11, p = 0.49). This result suggests that autism-associated genes specifically affecting excitatory neuronal cell types are also susceptible to the male-specific influence of androgen hormones in human neuronal stem cells.

We next additionally examined how such DHT-sensitive and autism-associated excitatory neuron genes spatially express in the adult human brain. This analysis would help shed insight on which brain areas might be more affected by such sex-specific effects in autism. A one-sample t-test of gene maps from the Allen Institute Human Brain Atlas[55] shows that this subset of DHT-sensitive and autism-associated excitatory neuron genes are highly expressed in MPFC, PCC, insula, and intraparietal sulcus, amongst other areas (Figure 4B-C).

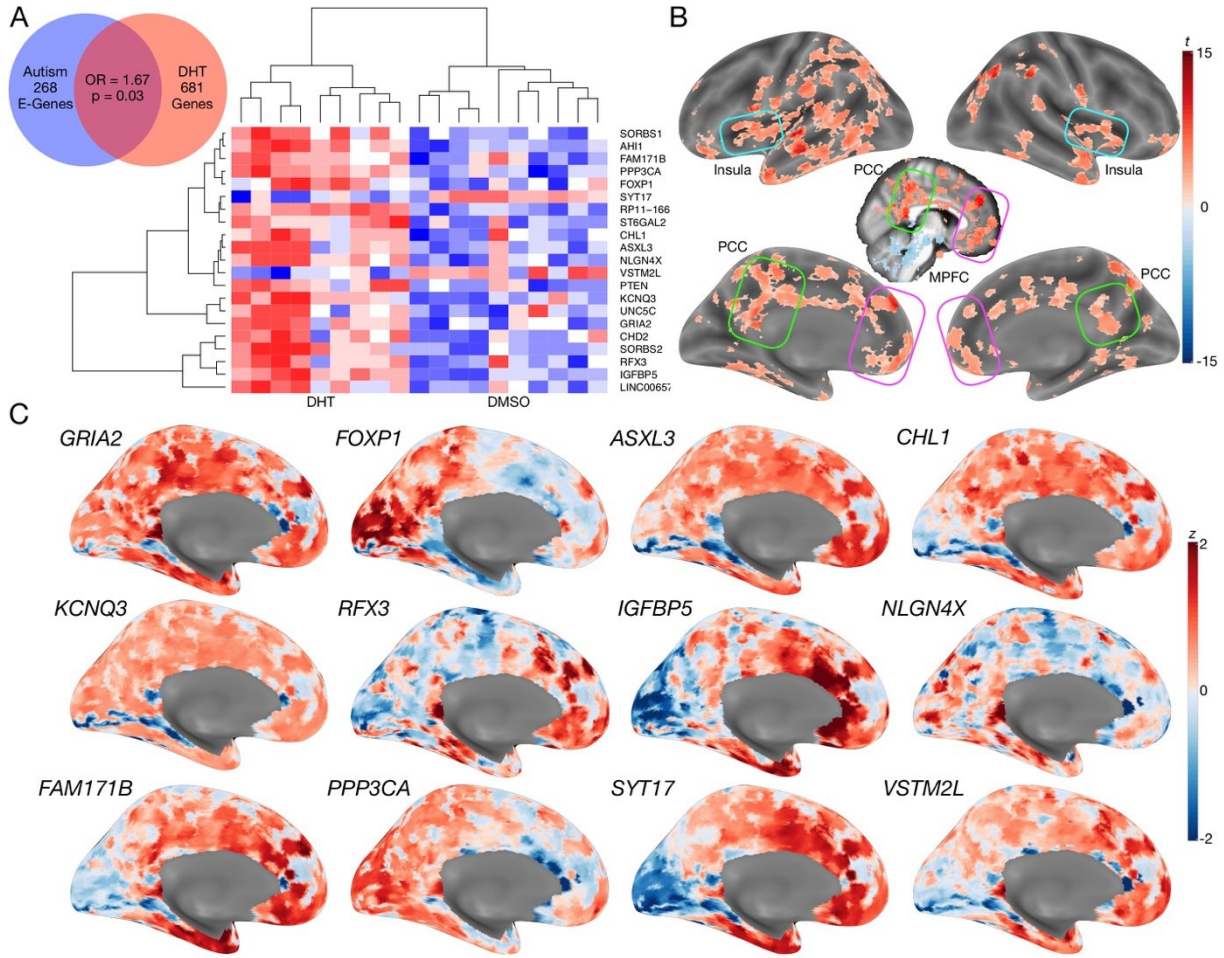

Figure 4: Autism-associated genes within excitatory neuronal cell types are enriched for genes differentially expressed by androgen hormones. *Panel A shows a Venn diagram depicting the enrichment between autism-associated genes affected excitatory neurons and DHT-sensitive genes. Panel A also includes a heatmap of these genes whereby the color indicates z-normalized expression values. The column dendrogram clearly shows that all samples with DHT treatment are clustered separately from the control (DMSO) samples. Each row depicts the expression of a different gene. Panel B shows a t-statistic map from a whole-brain one-sample t-test on these DHT-sensitive and autism-associated genes in excitatory neurons. Results are thresholded at FDR q<0.01. Panel C shows spatial gene expression profiles on a representative surface rendering of the medial wall of the cortex for specific genes shown in panel B. Each map shows expression as z-scores with the color scaling set to a range of -2<z<2.*

H is on-average reduced in adult autistic men but not women

We next move to application of this work to human rsfMRI data in autistic men and women. If E:I ratio is affected by sex-related mechanisms[13], we predict that H would be differentially affected in autistic males versus females and manifest as sex-by-diagnosis interactions in a 2x2 factorial design (Sex: Male vs Female; Diagnosis: Autism vs Typically-Developing (TD)). More specifically, the directionality of our predictions from the *in-silico* and *in-vivo* results in Figures 1-3 are that if H reflects E:I ratio, there should be decreased H (due to enhanced E) specifically in autistic males but not autistic females. Mass-univariate analysis uncovered one region in ventromedial prefrontal cortex (vMPFC),

region p32, with a sex-by-diagnosis interaction passing FDR q<0.05 (*F(5,104)* = 15.13, *p* = 0.0001, *partial* η^2 = 0.12) (Figure 5A). In line with directionality of our predictions, this interaction effect is driven by a large TD>Autism effect in males (*Cohen's d* = 1.30) and a small Autism>TD effect in females (*Cohen's d* = -0.27) (Figure 5B). A similar sex-by-diagnosis interaction appeared when using another metric such as the intrinsic neural timescale[30] (Figure 5 – figure supplement 1) and when H was first calculated at each voxel and then averaged across voxels (Figure 5 – figure supplement 2). While the main effects of diagnosis and sex are not the primary contrast for this study, we report that no significant regions survived FDR q<0.05 for the main effects of diagnosis. However, 61% of brain regions showed an on-average male>female sex difference (Figure 5 – figure supplement 1), which is in keeping with results from other work on sex differences in H[46].

In contrast to mass univariate analysis, we also used partial least squares (PLS) analysis as a multivariate alternative to uncover distributed neural systems that express the sex-by-diagnosis interaction. PLS analysis identified one neural system expressing the same sex-by-diagnosis interaction (*d* = 2.04, *p* = 0.036) and included default mode network (DMN) areas such as MPFC and posterior cingulate cortex/precuneus (PCC) (Figure 5 – figure supplement 1), and other non-DMN areas such as insula, lateral prefrontal cortex, somatosensory and motor cortices, intraparietal sulcus, amongst others (Figure 5C). Many of these regions detected by the PLS analysis were subthreshold of FDR q<0.05 in the mass-univariate analysis, but do show heightened effect sizes in keeping with this sex-by-diagnosis interaction pattern (e.g., white and light blue areas in the unthresholded map shown in Figure 5A). Detection of these regions in a mass-univariate analysis may require a larger sample size to enhance statistical power. Given that many of these PLS-identified regions of a sex-by-diagnosis interaction appear similar to those that appear in the gene expression map in Figure 4B of DHT-sensitive and autism-associated excitatory genes, we assessed how much each HCP-MMP parcellated regions overlap with the map in Figure 4B. PLS-identified regions in vMPFC (e.g., areas p32 and 10r) overlap by about 73-75%. Areas within the insula (e.g., Pol1, Pol2, MI) overlap by around 59-69%. Parietal areas in PCC (e.g., v23ab, d23ab) and intraparietal sulcus (LIPd) overlap by around 73-85% (Figure 5D).

Correlation between vMPFC H and camouflaging in autistic women but not men

In prior task-fMRI work we found a similar sex-by-diagnosis interaction in vMPFC self-representation response and a female-specific brain-behavioral correlation with camouflaging ability[19]. Given that adult autistic females engage more in camouflaging on-average[16–18], we next asked whether vMPFC H would be related to camouflaging in a sex-specific manner. In autistic females, increased camouflaging was strongly associated with increased H in vMPFC (*r* = 0.60, *p* = 0.001). However, no significant association was apparent in autistic males (*r* = -0.10, *p* = 0.63). The strength of this brain-behavioral correlation significantly differed between autistic males and females (*z* = 2.58, *p* = 0.009) (Figure 5E). This result suggests that progressively more intact vMPFC H in autistic females, which are likely reflective of more intact E:I balance, is associated with better ability to camouflage social-communicative difficulties. Beyond this hypothesis-driven comparison of the relationship between H and camouflaging in vMPFC, we also ran correlations with ADI-R, ADOS and AQ scores. ADOS social-communication (SC) was negatively correlated with vMPFC H in autistic females (r = -0.51, p = 0.008) indicating higher H with lower SC severity. This relationship was not present in autistic males (r = -0.04, p = 0.83). However, the difference between these correlations

was not statistically significant (z = 1.70, p = 0.08). ADI-R subdomains, ADOS RRB, and AQ correlations were not statistically significant.

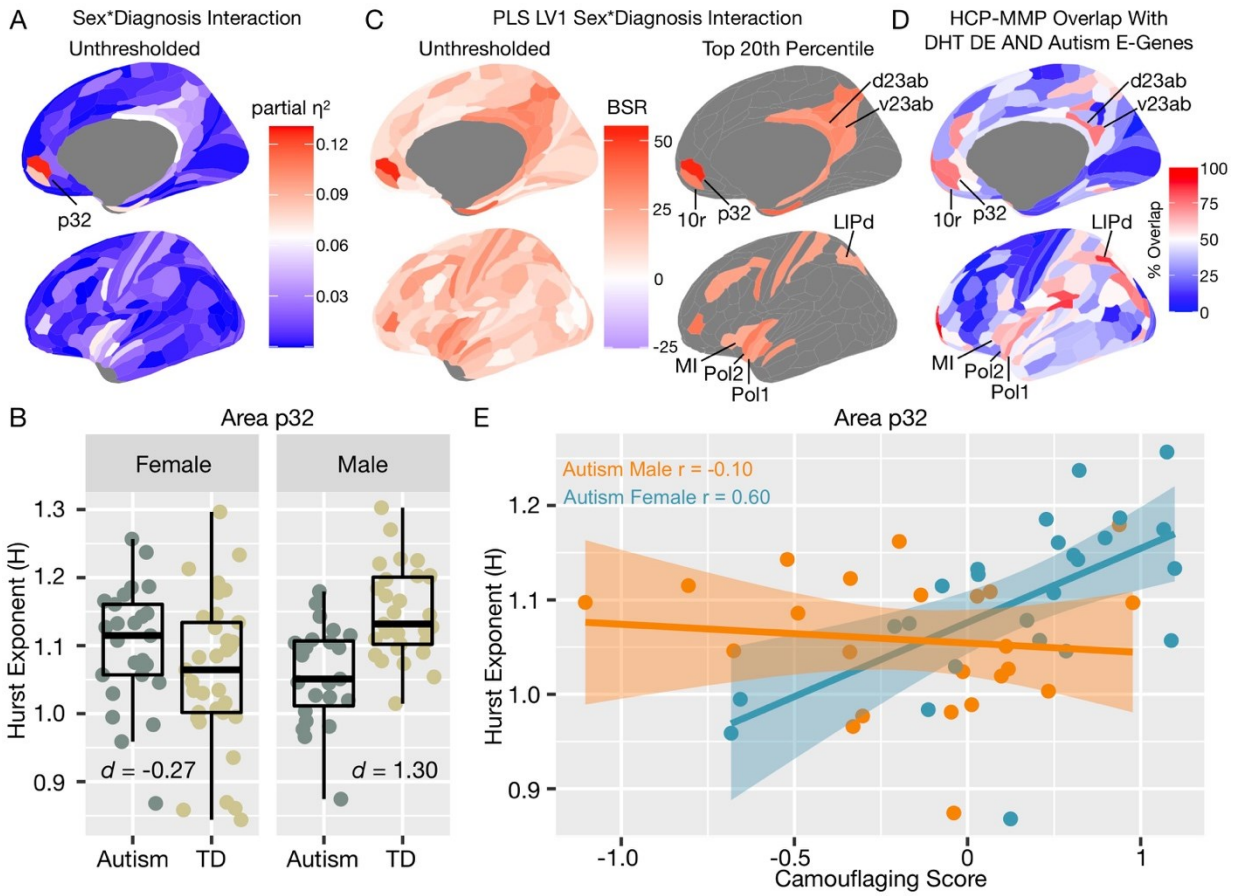

Figure 5: Autism rsfMRI sex-by-diagnosis interaction results. *Panel A shows unthresholded and thresholded with FDR q<0.05 mass-univariate results for the sex-by-diagnosis interaction contrast. Panel B shows H estimates from vMPFC (area p32) across males and females with and without autism. Panel C shows partial least squares (PLS) results unthresholded and thresholded to show the top 20% of brain regions ranked by bootstrap ratio (BSR). Panel D shows the percentage of voxels within each HCP-MMP parcellation region that overlap with the DHT-sensitive AND Autism E-Genes map shown in Figure 4B. Panel E shows correlation between vMPFC H and behavioral camouflaging score in autistic males (orange) and females (blue).*

Discussion

In this work we set out to better understand how intrinsic E:I imbalance affects the autistic brain in a sex-specific manner. Evidence from animal models of rare genetic variants associated with autism have typically been used as the primary evidence for the E:I imbalance theory[1,2]. However, these variants affect only a small percentage of the autism population. Thus, it is unclear how E:I imbalance might affect the majority of heterogeneous individuals within the total autism population. To bridge this gap we need multi-level methods that can be applied to understand the 'living biology' behind actual human individuals[56], such as *in-vivo* neuroimaging data and metrics applied to such

time-series data that are linked to actual underlying neural E:I mechanisms[57]. Bridging this gap will help us identify mechanistic targets that explain neural and behavioral variability across a much larger portion of individuals in the autism population.

Based on earlier work[28], we reasoned that metrics such as 1/f slope and H in neural time-series data would be relevant as an *in-vivo* neuroimaging marker of E:I mechanisms. Prior work suggested this relationship via a model that considers inhibition and excitation as separate entities[28]. However, excitation and inhibition in the brain are inseparably linked. Results about the relationship between spectral shape and E:I balance obtained with our model of recurrent excitation and inhibition are largely compatible with those obtained with an earlier model of uncoupled excitation and inhibition[28]. The uncoupled model predicts a linear increase of the slope value (i.e. flatter, less negative slopes) as E:I ratio increases. This is because in the uncoupled model changing the E:I ratio modifies only the ratio of the contribution to the LFP spectra of excitatory (faster time constant) and inhibitory (slower time constant) synaptic currents, leading to a linear relationship between slopes and E:I. In contrast, we found that the relationship between E:I and the spectral slope flattens out for high values of I. This, in our view, may in part arise from the fact that, as shown in studies of recurrent network models[25], higher recurrent inhibition leads to higher peak frequency of gamma oscillations (i.e. an increase of power at higher frequencies) thus partly counteracting the low-pass filtering effect of inhibitory currents in the uncoupled model. We plan to investigate in future studies how these opposing effects interact in a wider range of configurations and to use these results to gain a better understanding of the relationship between E:I ratio and LFP spectral shape.

Furthermore, prior work[28] considered only 1/f slopes in simulated LFP data and did not explore the effect of the transformation between LFP neural activity to BOLD. Our simulations address these problems and significantly extends prior work[28] on the relationship between E:I imbalance and changes in spectral properties of neural signals. We showed that when excitation and inhibition interact in a recurrent network model, flatter 1/f slopes and decreases in H are specific markers of increases in E:I ratio. We also showed that in simulated BOLD signal, H and E:I ratio are associated in a manner similar to the relationships observed with LFP data. Taken together, these results predict that changes in H in neural time-series data can be interpreted as a shift in synaptic E:I ratio that permeates through in LFP or BOLD readouts.

Our simple model to generate BOLD from frequency-resolved LFPs reflect several features of the empirical LFP-BOLD relationship - namely the presence of a particularly strong gamma-BOLD relationship and the fact that a better prediction of the BOLD is obtained from the frequency-resolved LFP than from the wideband LFP. However, a limitation of our simple model is that, in its present form, it cannot capture the negative relationship between the power of some low-frequency LFP bands and the BOLD amplitude that has been reported in some studies[47,48,58,59]. Modelling the low frequency LFP to BOLD relationship in greater detail would require significant extensions of our neural model, as lower frequency oscillations are thought to arise from more complex cortico-cortical and thalamocortical loops than those that can be captured by our simple model of a local recurrent circuit with only two classes of neurons and no spatial structure[60,61]. An important topic for further modelling work will be to understand how biomarkers of more complex neural feedback loops can be extracted from LFP or BOLD spectral signatures.

The power of our *in-silico* modeling approach is that it provides explicit predictions of what to expect in real BOLD data when synaptic E:I imbalance occurs. Remarkably, these *in-silico* predictions are confirmed *in-vivo* with rsfMRI BOLD data in halothane-sedated mice after experimental chemogenetic manipulations that specifically enhance neural excitation. Intriguingly, and consistent with *in-silico* predictions, manipulations that silence both excitatory and inhibitory neuronal populations do not have a strong effect on H in BOLD. These results are in line with optogenetic studies showing that specifically enhancing excitation in MPFC seems to have the biggest effects on social behavior in mice[14]. The present work clearly shows that enhancement of excitation results in measurable changes in BOLD readouts as decreases in H. This insight allows us to leverage H as an *in-vivo* rsfMRI biomarker that has strong relevance back to synaptic E:I imbalance. Future extensions of our research might involve refined modelling and the use of chemogenetic manipulations in awake conditions, hence minimizing the possible confounding contribution of anesthesia on baseline E:I balance.

With regards to how sex-related heterogeneity in E:I imbalance might manifest in autism, we utilized genomics data and found that autism-associated genes that affect excitatory neuronal cell types are enriched for genes that are differentially expressed by DHT in human neuronal stem cells. This inference extends prior work implicating excitatory neuron cell types in autism-relevant biology[52,53,62,63] by linking genomic mechanisms in these cell types to the male-specific influence of androgen hormones. Importantly, other cell types such as inhibitory neurons do not express autism-associated genes that are also influenced by DHT. Additionally, the DHT-sensitive and autism-associated excitatory genes tend to spatially express in the human adult brain in regions such as MPFC, PCC, insula, and intraparietal sulcus, which have been shown to be affected in autism across a range of task-related and rsfMRI studies[19,64–68], and which overlap with areas discovered by the PLS analysis to express a sex-by-diagnosis interaction (Figure 5D).

Moving to human rsfMRI data on adult patients with autism, we utilized H as a neuroimaging biomarker of E:I imbalance. Specifically, we examined whether H differs between adult males and females with and without autism. Mass-univariate analysis highlighted one region in vMPFC which showed a sex-by-diagnosis interaction - that is, H was specifically reduced in adult autistic males, but not in autistic females. Reduced H in autistic males is compatible with the inference of elevated E:I ratio potentially driven by enhanced excitation. The observed effect in vMPFC may also be consistent with a 'gender-incoherence' pattern (i.e. towards reversal of typical sex differences in autism)[69]. However, sex-specific normative ranges would need to be better established before interpreting effects in autism as being reversals of normative sex differences. More work with much larger general population-based datasets is needed to establish whether there are robust normative sex differences in H and to describe the normative ranges of H may take for each brain region, sex, and across age. Such work would also help with normative modeling[70] approaches that would enable identification of which autistic individuals highly deviate from sex-specific norms.

Multivariate PLS analysis extended the mass univariate results by showing that a distributed neural system structurally and functionally connected to vMPFC, such as default mode network (DMN) areas like PCC[71,72], as well as intraparietal sulcus and insular cortex[66], also expressed a similar

but more subtle sex-by-diagnosis interaction. Interestingly, these regions highlighted by the PLS analysis are remarkably similar to the map of brain regions where autism-associated excitatory and DHT-sensitive genes highly express (Figure 4B-C, Figure 5D). Therefore, important social brain circuitry such as the DMN, and other integrative hubs of the salience network (e.g., insula) that connect DMN to other important large-scale networks[66] may be asymmetrically affected by heightened E:I ratio in autistic males more than autistic females.

These human rsfMRI results are not only compatible with the *in-silico* predictions and the *in-vivo* mouse rsfMRI data presented here, but are also compatible with several prior lines of work. Our prior work highlighted that DMN functional connectivity in typically developing adolescent males, but not females, is affected by heightened levels of fetal testosterone and this network was heavily comprised of MPFC and PCC[13]. In the same work, we showed that a cortical midline DMN subsystem comprising MPFC and PCC highly expresses several genes relevant for excitatory postsynaptic potentials (e.g., *MEF2C, GRIK2, GRIA1, SCN3A, SCN9A, NPTX2*). The current findings linking autism-associated genes in excitatory neuron cell types (Figure 4) allow for more precise inferences about the importance of excitatory cell types over and above other inhibitory cell types. This is important given that evidence regarding inhibitory neuronal cell types and their role in E:I imbalance in autism is more mixed[73,74]. Importantly, the expression of these genes in human neuronal stem cells are elevated after exposure to the potent androgen DHT[13]. Thus, one potential explanation for the male-specific reduction of H in vMPFC could have to do with early developmental and androgen-sensitive upregulation of genes that play central roles in excitatory neuron cell types, and thus ultimately affecting downstream E:I imbalance. Such effects may be less critical in human females and may serve an important basis for sex-differential human brain development[75]. These effects may also help explain why qualitative sex differences emerge in autism[10,76].

rsfMRI H in autistic adults was also relevant in a sex-specific manner to a clinical behavioral phenomenon known as 'camouflaging'. Camouflaging relates to a set of compensatory or masking strategies/mechanisms that allow individuals to cope with their social-communicative difficulties in everyday social situations[16,17,77]. It is known that cognitively able adult autistic females tend to engage in more camouflaging behavior than males[16–18] and the extent to which individual females engage in camouflaging is linked to vMPFC function[19]. One of the most important known functions of vMPFC has to do with self-representation[68] and simulating others based on information about the self[78]. In prior task-related fMRI work we found a similar sex-by-diagnosis interaction effect whereby males are more impaired in vMPFC self-representation response than their female autistic counterparts. Furthermore, increased magnitude of vMPFC self-representation neural response correlates with increased camouflaging ability, but only in adult autistic females[19]. Strikingly, here we find a similar sex-by-diagnosis interaction effect in vMPFC H as well as a female-specific correlation with camouflaging - as vMPFC H increases, indicative of a more normative or intact level of E:I balance, camouflaging also increases. This converging set of results suggests that intrinsic mechanisms such as E:I balance may be atypical only in cognitively able autistic males at vMPFC. More intact E:I balance in the vMPFC of autistic females may enable better vMPFC-related function (e.g., self-representation) and thus potentially better enable these individuals to camouflage social-communicative difficulties and cope in social situations. Future work changing E:I balance in vMPFC may provide a useful avenue for ameliorating daily life social-communication adaptation and coping difficulties in autistic males and enable them to optimally engage in compensatory processes such as camouflaging to the similar extent as autistic females. It may also be fruitful to examine how intact E:I balance in vMPFC of

females may be an expression of protective factors that are hypothesized to buffer risk for autism in females[79,80].

This work may also be of broader relevance for investigating sex-specific E:I imbalance that affects other early-onset neurodevelopmental disorders with a similar male-bias as autism[81]. For instance, conditions like ADHD affect males more frequently than females and also show some similarities in affecting behavioral regulation and associated neural correlates[82]. Furthermore, gene sets associated with excitatory and inhibitory neurotransmitters are linked to hyperactivity/impulsivity severity in ADHD, suggesting that E:I-relevant mechanisms may be perturbed[83]. It will be important for future work to test how specific sex-specific E:I imbalance is to autism versus other related sex-biased neurodevelopmental disorders. Similarly, future work should investigate how H may change over development. Prior work has shown that H and other related measures such as 1/f slope can change with normative and pathological aging in both rsfMRI and EEG data[21,84,85]. Imperative to this work will be the establishment of age and sex-specific norms for H in much larger datasets. Age and sex-specific norms will enable more work to better uncover how these biomarkers may be affected in neurodevelopmental disorders or disorders relevant to neurodegeneration. Such work combined with normative modeling approaches[70] may help uncover how experiential and environmental effects further affect such metrics.

In conclusion, we show that spectral properties of neural time-series data, such as H and 1/f slope, can be utilized in neuroimaging readouts like LFP and BOLD as a biomarker for underlying E:I-relevant mechanisms. *In-silico* predictions from simulated LFP and BOLD data were confirmed *in-vivo* with rsfMRI BOLD data where excitation was enhanced through chemogenetic manipulation. Finally, in application to humans, we show that H in rsfMRI data is reduced in vMPFC and other DMN areas of adult autistic males, but not females. Reduced H is indicative of enhanced excitation and thus points to sex-specific dysregulation of E:I balance in social brain networks of autistic males. This male-specific dysregulation of E:I balance may be linked to sex-differential early developmental events such as androgen-upregulation of gene expression for genes that play important roles in excitatory neurons[13]. The intact levels of H in females may help facilitate elevated levels of compensation known as camouflaging to cope with daily social-communicative difficulties. This important female-specific brain-behavioral correlation may also be key for future interventions targeting E:I mechanisms and MPFC-related brain networks to enable better coping with daily social-communicative difficulties. More generally, this work extends the relevance of the E:I imbalance theory of autism beyond evidence from autism-associated rare genetic variants and specify a larger portion of the autism population whereby these E:I mechanisms may be of critical importance.

Methods

Human Participants

All procedures contributing to this work comply with the ethical standards of the relevant national and institutional committees on human experimentation and with the Helsinki Declaration of 1975, as revised in 2008. All human participants' informed consent was obtained in accord with procedures approved by the Suffolk Local Research Ethics Committee. Adult native English speakers (n=136, age range = 18-49 years) with normal/corrected-to-normal vision participated: n=33 typically developing (TD) males, n=34 autistic males, n=34 TD females and n=34 autistic females (Table 3). They all reported cis-gender identity based on a single item inquiring their birth-assigned sex and another on their identified gender. Groups were not statistically different on age or full-scale IQ (FIQ) on the Wechsler Abbreviated Scales of Intelligence (WASI) (Table 3). Exclusion criteria for all participants included a history of or current psychotic disorders, substance-use disorders, severe head injury, genetic disorders associated with autism (e.g. fragile X syndrome and tuberous sclerosis), intellectual disability (i.e. Full-scale IQ (FIQ) < 70), or other medical conditions significantly affecting brain function (e.g. epilepsy).

The inclusion criterion for both male and female autistic participants was a formal clinical diagnosis of International Statistical Classification of Diseases and Related Health Problems 10th Revision (ICD-10) childhood autism or Asperger's syndrome, or Diagnostic and Statistical Manual of Mental Disorders (4th ed., text rev.; DSM-IV-TR) autistic disorder or Asperger's disorder, as assessed by a psychiatrist or clinical psychologist in the National Health Service, UK. Since all participants were adults, we further considered available information of developmental history to include only those with clinically evident childhood autistic symptoms, for example, from information collected using the Autism Diagnostic Interview–Revised (ADI-R)[86] where possible, or from the participants' clinical diagnosis letters shared with the research team to determine eligibility. We used this clinically based criterion for inclusion for the purpose of sampling autistic individuals currently diagnosed by specialists in mental health services in the daily practice and to align with best clinical practice as recommended by the UK National Institute for Health and Clinical Excellence (NICE) guideline[87]. For assessing levels of autism characteristics, we administered the Autism Spectrum Quotient (AQ)[88], module 4 of the Autism Diagnostic Observation Schedule (ADOS)[89], and ADI-R[86] where possible, before the fMRI session. Autistic male and female groups were not significantly different on any ADI-R subdomain scores or Reading the Mind in the Eyes Test (RMET)[90] performance (Table 3).

We further used criteria for inclusion based on characteristics about data quality (see next paragraphs for data preprocessing). In particular, we excluded participants where the number of volumes was not acquired due to scanner hardware issues (n=1), the preprocessing pipeline could not adequately preprocess the data (e.g., bad registrations; n=5). Participants were also excluded if their head motion exceed a mean framewise displacement (meanFD)[91] of >0.4mm (n=8). For the remaining subjects we further visually inspected plots of framewise displacement (FD) and DVARS[91] traces to determine whether the wavelet despiking step sufficiently attenuated artefact-related variability that would leave DVARS spikes. Here we made a qualitative and consensus judgement amongst authors (S.T. and M.V.L) to exclude individuals (n=9) whereby there were numerous FD

spikes above 0.5mm or numerous DVARS spikes leftover after wavelet despiking was applied. Other exclusions included any VIQ or PIQ <70 (n=1) and co-morbid agenesis of the corpus callosum (n=1). The final sample sizes included in all further analyses was n=29 TD males, n=23 autistic males, n=33 TD females, and n=25 autistic females. The final groups used in all analyses did not statistically differ on age (diagnosis main effect: $F(3,106)$ = 0.03, p = 0.85; sex main effect: $F(3,106)$ = 0.14, p = 0.70; sex-by-diagnosis interaction: $F(3,106)$ = 0.25, p = 0.61) or FIQ (diagnosis main effect: $F(3,106)$ = 3.38, p = 0.07; sex main effect: $F(3,106)$ = 0.48, p = 0.48; sex-by-diagnosis interaction: $F(3,106)$ = 2.24, p = 0.13) (see Table 3).

Human fMRI data acquisition

Imaging was performed on a 3T GE Signa Scanner at the Cambridge Magnetic Resonance Imaging and Spectroscopy Unit. Participants were asked to lie quietly in the scanner awake with eyes closed for 13 minutes and 39 seconds during sequential acquisition of 625 whole-brain T2*-weighted echo planar image volumes with the following parameters: relaxation time = 1302 ms; echo time = 30 ms; flip angle = 70°; matrix size = 64 x 64; field of view = 24 cm; 22 anterior commissure-posterior commissure aligned slices per image volume; 4 mm axial slice thickness; 1 mm slice gap. The first five time-points were discarded to allow for T2-stabilization. During analysis of the Hurst exponent (H) for BOLD time-series, due to the discrete wavelet transform using volumes in power of 2, only the first 512 volumes (2^9) were utilized. A high-resolution spoiled gradient anatomical image was acquired for each participant for registration purposes.

Human fMRI data analysis

Preprocessing of the resting state data was split into two components; core preprocessing and denoising. Core preprocessing was implemented with AFNI[92] (http://afni.nimh.nih.gov/) using the tool speedypp.py (http://bit.ly/23u2vZp)[93]. This core preprocessing pipeline included the following steps: (i) slice acquisition correction using heptic (7th order) Lagrange polynomial interpolation; (ii) rigid-body head movement correction to the first frame of data, using quintic (5th order) polynomial interpolation to estimate the realignment parameters (3 displacements and 3 rotations); (iii) obliquity transform to the structural image; (iv) affine co-registration to the skull-stripped structural image using a gray matter mask; (v) nonlinear warping to MNI space (MNI152 template) with AFNI 3dQwarp; (v) spatial smoothing (6 mm FWHM); and (vi) a within-run intensity normalization to a whole-brain median of 1000. Core preprocessing was followed by denoising steps to further remove motion-related and other artifacts. Denoising steps included: (viii) wavelet time series despiking ('wavelet denoising'); (ix) confound signal regression including the 6 motion parameters estimated in (ii), their first order temporal derivatives, and ventricular cerebrospinal fluid (CSF) signal (referred to as 13-parameter regression). The wavelet denoising method has been shown to mitigate substantial spatial and temporal heterogeneity in motion-related artifact that manifests linearly or non-linearly and can do so without the need for data scrubbing[94]. Data scrubbing (i.e. volume censoring) cannot be used in our time-series-based analyses here as such a procedure breaks up the temporal structure of the time-series in such a way that invalidates estimation of the Hurst exponent (H) that examine long-memory characteristics. Wavelet denoising is implemented with the Brain Wavelet toolbox (http://www.brainwavelet.org). The 13-parameter regression of motion and

CSF signals was achieved using AFNI 3dBandpass with the –ort argument. To further characterize motion and its impact on the data, we computed FD and DVARS[91]. Between-group comparisons showed that all groups were similar with respect to head motion as measured by meanFD with no diagnosis ($F(3,106)$ = 1.77, p = 0.18) or sex ($F(3,106)$ = 0.51, p = 0.47) main effects or sex-by-diagnosis interaction ($F(3,106)$ = 1.10, p = 0.29). All groups showed average meanFD of less than 0.2 mm (see Table 3).

Mean time-series for each of the 180 parcels within the Human Connectome Project Multimodal Parcellation (HCP-MMP)[95] were extracted from the final preprocessed data, to estimate H. The estimation of H utilizes a discrete wavelet transform and a model of the time-series as fractionally integrated processes (FIP) and is estimated using maximum likelihood estimation. This method utilizing the FIP model for estimating H differs from our prior work[29], which used a model of fractional Gaussian noise (fGn). fGn is one type of process subsumed under the FIP model. However, the fGn model has the limitation of assuming that the BOLD time-series is stationary and also limits the upper bound of H at 1. In practice, we have seen that the upper bound of H=1 from the fGn model results in ceiling effects for many brain regions and subjects. Thus, to remove the assumption of stationarity and upper bound of H=1, the FIP model offers more flexibility and potentially added sensitivity due to better estimation of between-subject variability when estimates are near or exceed H=1. When H>1 the time-series is considered non-stationary and has long memory characteristics (e.g., is fractal). H is computed using the *nonfractal* MATLAB toolbox written by one of the co-authors (WY) (https://github.com/wonsang/nonfractal). The specific function utilized is bfn_mfin_ml.m function with the 'filter' argument set to 'haar' and the 'ub' and 'lb' arguments set to [1.5,10] and [-0.5,0], respectively.

After H was estimated for each of the 180 HCP-MMP parcels, we used a general linear model to test for sex-by-diagnosis interactions as well as main effects of Sex and Diagnosis in H. These models also incorporated meanFD and FIQ as covariates of no interest. Multiple comparison correction was achieved using an FDR q<0.05 threshold. Visualization of effect sizes for figures was achieved using the *ggseg* library in R (https://github.com/LCBC-UiO/ggseg).

In addition to mass-univariate analysis, we also utilized multivariate partial least squares (PLS) analysis[96] to highlight distributed neural systems that capture the effect of a sex-by-diagnosis interaction. This analysis was implemented with code from the *plsgui* MATLAB toolbox (http://www.rotman-baycrest.on.ca/pls/). A matrix with participants along the rows and all 180 HCP-MMP parcels along with columns was input as the primary neuroimaging matrix for PLS. We also inserted a vector describing the sex-by-diagnosis contrast as the matrix to relate to the neuroimaging matrix. This vector describing the sex-by-diagnosis interaction was computed by matrix multiplication of the contrast vector of [1, -1, -1, 1] to a design matrix that was set up with columns defining TD males, autism males, TD females, and autism females, respectively. The PLS analysis was run with 10,000 permutations to compute p-values for each latent-variable (LV) pair and 10,000 bootstrap resamples in order to compute bootstrap ratios (BSR) to identify brain regions of importance for each LV pair. To isolate specific brain regions of importance for a statistically significant LV, we selected the top 20th percentile of brain regions ranked by BSR.

Relationships between H and camouflaging were conducted within autistic males and females separately. Pearson's correlations were used to estimate the strength of the relationship and groups were compared on the strength of the relationship using Fisher's r-to-z transform as implemented with the paired.r function in the *psych* library in R.

Behavioral index of camouflaging

Camouflaging (consciously or unconsciously compensating for and/or masking difficulties in social–interpersonal situations) was operationalized as prior work[16,19]: the discrepancy between extrinsic behavioral presentation in social–interpersonal contexts and the person's intrinsic status. We used both the AQ score and RMET correct score as reflecting intrinsic status (i.e. self-rated dispositional traits and performance-based socio-cognitive/mentalizing capability), and the ADOS Social-Communication total score as reflecting extrinsic behavioral presentation. The three scores were first standardized (S_{ADOS}, S_{AQ} and S_{RMET}) within our sample of autistic men and women by mean-centering (to the whole autism sample in this study) and scaling (i.e. divided by the maximum possible score of each) to generate uniformly scaled measures that can be arithmetically manipulated. The first estimate of camouflaging was quantified as the difference between self-rated autistic traits and extrinsic behaviors ($CF1 = S_{AQ} - S_{ADOS}$), and the second estimate between mentalizing ability and extrinsic behaviors ($CF2 = -S_{RMET} - S_{ADOS}$). Then, using principal component analysis, the first principal component score of CF1 and CF2 (accounting for 86% of the total variance) was taken as a single, parsimonious measure of camouflaging for all subsequent analyses. This method was utilized in order to be consistent with prior work which computed the camouflaging metric in an identical fashion[16,19]. This measure should be interpreted by relative values (i.e. higher scores indicate more camouflaging) rather than absolute values. This operationalization only allows for estimating camouflaging in autistic individuals in our cohort, as it partly derives from the ADOS score which was not available in TD participants. This approach remains informative, as qualitative studies suggest that camouflaging in autism can be different from similar phenomenon (e.g. impression management) in TD individuals[97,98].

In-vivo chemogenetic manipulation of excitation in mouse prefrontal cortex

All *in-vivo* studies in mice were conducted in accordance with the Italian law (DL 116, 1992 Ministero della Sanità, Roma) and the recommendations in the Guide for the Care and Use of Laboratory Animals of the National Institutes of Health. Animal research protocols were also reviewed and consented to by the animal care committee of the Istituto Italiano di Tecnologia. The Italian Ministry of Health specifically approved the protocol of this study, authorization no. 852/17 to A.G. All surgical procedures were performed under anesthesia.

Six to eight week-old adult male C57Bl6/J mice (Jackson Laboratories; Bar Harbor, ME, USA) were anesthetized with isoflurane (isoflurane 4%) and head-fixed in a mouse stereotaxic apparatus (isoflurane 2%, Stoelting). Viral injections were performed with a Hamilton syringe mounted on Nanoliter Syringe Pump with controller (KD Scientific), at a speed of 0.05 l/min, followed by a 5–10 min waiting period, to avoid backflow of viral solution and unspecific labeling. Viral suspensions were injected bilaterally in PFC using the following

coordinates, expressed in millimeter from bregma: 1.7 from anterior to posterior, 0.3 lateral, −1.7 deep. The inhibitory DREADD hM4Di was transduced using an AAV8-hSyn-hM4D(Gi)-mCherry construct. Control animals were injected with a control AAV8-hSyn-GFP virus (www.addgene.com). These viral suspensions were injected using a 0.3 µL injection volume in n=15 hM4Di DREADD and n=19 SHAM mice, respectively. The excitatory DREADD hM3Dq was transduced using an AAV8-CamkII-hM3D (Gq)-mCherry construct. Control animals for this experiment were injected with a control AAV8-hSyn-GFP construct. This set of injection were carried out using a 1µL injection volume in n=17 hM3Dq DREADD and n=19 SHAM mice, respectively. We waited at least 3 weeks to allow for maximal viral expression.

Mouse rsfMRI data acquisition

The animal preparation protocol for mouse rsfMRI scanning was previously described in detail[99]. Briefly, mice were anesthetized with isoflurane (5% induction), intubated and artificially ventilated (2% maintenance). Then isoflurane was discontinued and substituted with halothane (0.75%), a sedative that preserves cerebral blood flow auto-regulation and neurovascular coupling[100]. Functional data acquisition commenced 30 min after isoflurane cessation. CNO (2 mg/kg for hM4Di and 0.5 mg/kg for hM3Dq) was administered i.v. after 15 minutes from the beginning of the acquisition both in virally transduced animals and in sham mice.

Mouse rsfMRI data analysis

Raw mouse rsfMRI data was preprocessed as described in previous work[101,102]. Briefly, the initial 120 volumes of the time-series were removed to allow for T1 and gradient equilibration effects. Data were then despiked, motion corrected and spatially registered to a common reference template. Motion traces of head realignment parameters (3 translations + 3 rotations) and mean ventricular signal (corresponding to the averaged BOLD signal within a reference ventricular mask) were used as nuisance covariates and regressed out from each time course. All rsfMRI time-series also underwent band-pass filtering to a frequency window of 0.01–0.1 Hz and spatial smoothing with a full width at half maximum of 0.6 mm.

The experimental design of the study allowed for computation of H during time-windows in the rsfMRI scan before drug injection (i.e. 'Baseline'), a transition phase where the drug begins having its effect (i.e. 'Transition'), and a treatment phase when the drug is thought to have its optimal effect (i.e. 'Treatment'). Analysis of condition, treatment phase, time, and all interactions between such factors was achieved using a sliding window analysis. Each window was 512 volumes in length and the sliding step was 1 volume. H is computed at each window and results in an H time-series. The H time-series is used as the dependent variable in a linear mixed effect model (i.e. using the *lme* function within the *nlme* library in R) with fixed effects of condition, time, treatment phase, and all 2-way and 3-way interactions between such factors as well as a factor accounting for scan day. Random effects in the model included time within mouse as well as treatment phase within mouse, all modeled with random intercepts and slopes. This omnibus model was utilized to examine a 3-way interaction between condition, time, and treatment phase. If this interaction was present, we then split the data by the 3 levels of the treatment phase (e.g., Baseline, Transition, and Treatment), in order to examine the main effect of condition or the condition*time interaction. Plots of the data indicate each mouse (grey lines in Figure 3) as well as group trajectories for each phase, with all trajectories estimated with a generalized additive model smoother applied to individual mice and group trajectories.

In-silico recurrent network modeling of LFP and BOLD data

The recurrent network model we use represents a standard cortical circuit incorporating integrate-and-fire excitatory and inhibitory spiking neurons that interact through recurrent connections and receive external inputs (both a sensory driven thalamic input and a sensory unrelated intracortical input, see Figure 1A). The network structure and parameters of the recurrent network model are the same ones used in Cavallari et al.,[40] with conductance-based synapses (for full details see[40]). The network is composed of 5000 neurons, of which 4000 are excitatory (i.e. they form AMPA-like excitatory synapses with other neurons) and 1000 inhibitory (forming GABA-like synapses). Neurons are randomly connected with a connection probability between each pair of neurons of 0.2. Both populations receive two different types of external Poisson inputs: a constant-rate thalamic input and an intracortical input generated by an Ornstein-Uhlenbeck (OU) process with zero mean. A description of the baseline reference parameters used in simulations is given in Table 4. The LFP is computed as the sum of absolute values of AMPA and GABA postsynaptic currents on excitatory cells[26,37]. This simple estimation of LFPs was shown to capture more than 90% of variance of both experimental data recorded from cortical field potentials and of simulated data from a complex three-dimensional model of the dipoles generated by cortical neurons[26,37,39]. We changed the E:I ratio by independently varying the strengths of the inhibitory (g_I) and excitatory (g_E) synaptic conductances. We called g the relative ratio between inhibitory and excitatory conductances ($g = g_I/g_E$). We present results of simulations for two levels of strength of thalamic input (υ_0 = 1.5 spikes/second and υ_0 = 2 spikes/second), and we verified that our results hold qualitatively for a wider range of input levels (1.5 to 4 spikes/second).

For the simulations used to compute H and 1/f slope of LFPs, we simulated a 10-second stretch of network activity from which we extracted a 10-second LFP time series used to compute H and 1/f slopes for each individual value of g (Figure 1B). To estimate power spectral density (PSD) we computed the Fast Fourier Transform with the Welch's method, dividing the data into ten overlapping segments with 50% overlap. 1/f slopes were computed with least-squares regressions predicting log power with log frequency. A piece-wise regression was applied to fit two line segments to the PSD – one segment to a low frequency region from 1-30 Hz and a second segment to a high-frequency region from 30-100 Hz.

As a basis for our model translating BOLD from LFP data, we note that prior studies with simultaneous electrophysiological and fMRI recordings in non-human primates have established that BOLD signal amplitude is more closely correlated with LFP than with any other type of neuronal events, such as spikes[42,43]. Similarly, simultaneous electroencephalogram (EEG)/fMRI studies in humans have found that the BOLD correlates with the EEG[48,103], which in turns correlates strongly with the LFP[104]. Importantly, the BOLD amplitude at any given time has been found to correlate preferentially with the power of high frequency bands. In particular, the BOLD amplitude correlates strongly with the gamma (40 - 100 Hz) band. However, the power distribution across frequency bands carries complementary information about the BOLD signal, meaning that each band contributes to the prediction of BOLD and predicting the BOLD signal directly from a wide band (i.e. the whole LFP spectrum) leads to poorer predictions of BOLD[42,43,47,48,105,106]. To account for these empirical

observations, we have developed a model of BOLD signal that integrates contributions from different bands with a preferential contribution from high frequency bands.

To compute the simulated BOLD through the convolutions of the simulated LFPs, we needed to generate longer time series than the initial 10 seconds simulated for LFPs. However, it was unfeasible to simulated very long BOLD time-series due to limitations on computational resources. We thus created, from the LFP data used for evaluations of individual g values, aggregated LFP time-series corresponding to different intervals of g (rather than individual values of g), as follows. The set of 10-second LFP time series was divided into 3 equi-populated groups of g: g < 7.5, 7.5 < g < 11 and g > 11. A concatenated LFP time series was created for each group by randomly concatenating 20 LFP traces, which provided 200-second LFP signals. Low frequencies of the concatenated data were log-log linearly extrapolated based on the low-frequency slopes obtained in LFP log-log linear piecewise fitting. To account for statistical variability, the process of concatenating data was repeated 20 times for each group of g, randomly changing the order in which the individual LFP traces were combined within the group.

Once concatenated LFP time-series data was simulated, we compute the simulated BOLD time-series as the LFP data convolved not only with a hemodynamic response function (HRF), as in standard network models[35,107,108], but also with a high-pass filter (HPF) that gives more predictive power to higher LFP frequencies (Figure 2 – figure supplement 1B). We have tested different parameters of the HPF, checking that changing the parameters produce qualitatively similar results and a monotonic correspondence between H of simulated LFP and H of simulated BOLD, and we opted for a HPF with a cutoff frequency (the frequency where the response is lowered by 3 dB) of 12.5 Hz and with a peak response at 20 Hz. The effect of the HPF was to attenuate low frequencies of the BOLD power distribution, partly compensating the low-frequency enhancement of HRFs, and to shift the peak frequency of BOLD power to 0.03 Hz, a value much closer to the peak frequency found in our real BOLD data and in most BOLD studies[109,110] with respect to the one that would have been obtained without convolution (see Figure 2 – figure supplement 1).

To simulate BOLD response from the LFP data generated from the recurrent model, within the frequency domain we multiplied the LFP spectrum with spectra of the high-pass filter (HPF) and the hemodynamic response function (HRF), as follows:

$$FFT(BOLD) = FFT(LFP)FFT(HPF)[FFT(HRF) + \eta]$$

Where FFT is the fast Fourier transform operation and η is a constant white noise term. This noise term summarizes neurovascular relationship at frequencies not observable because they are faster than the BOLD acquisition frequencies. We assumed that the amplitude of η was very small and we assigned small values to this noise term. We checked that the exact value of amplitude of η, or the spectral profile of this noise term (for example, simulating 1/f noise instead of white noise), did not alter the monotonic relationship between the simulated H of BOLD and LFP. Finally, the simulated BOLD time-series data was produced by applying the inverse Fourier transform of

$FFT(BOLD)$ and then downsampling the resulting signal to a lower sampling rate, similar to that used in BOLD experiments (e.g., 0.5 Hz). The HRF used for simulating BOLD was the HRF from Magri et al.,[43], but similar results were obtained when using a canonical HRF (see Figure 2 – figure supplement 2).

Analyses examining enrichment of autism-associated genes in different cell types with genes differentially expressed by androgen hormones

To test hypotheses regarding cell types that may be affected by androgen influence, we examined genes linked to autism via rare de novo protein truncating variants that are enriched for expression in specific cell types[52]. Of the 102 genes reported by Satterstrom et al., we split these lists by enrichments in early excitatory neurons (C3), MGE derived cortical interneurons (C16), microglia (C19), and astrocytes or oligodendrocyte precursor cells (C4). In addition to high risk mutations linked to autism, we additionally used a list of genes differentially expressed (DE) in different cell types within post-mortem prefrontal and anterior cingulate cortex tissue of autistic patients[53]. These DE gene lists were split into cell types, and we examined DE genes in any excitatory neuronal cell class (L2/3, L4/ L5/6), inhibitory cell classes (IN-PV, IN-SST, IN-VIP, IN-SV2C), microglia, astrocytes (AST-PP, AST-FB), and oligodendrocytes.

To test the question of whether cell type autism-associated gene lists were enriched for genes known to be differentially expressed by DHT, we used a previous DE gene list from an RNA-seq dataset of DHT administration to human neuronal stem cells was utilized for these tests[13]. Custom code was utilized to compute enrichment odds ratios and hypergeometric p-values for each enrichment test with different cell type autism-associated lists. The background total for these tests was the total number of genes considered in the original DHT-administration dataset (13,284).

To test how the DHT-sensitive and autism-associated genes in excitatory neurons are expressed across the human adult brain, we used whole-brain maps of expression for each gene in MNI space from the Allen Institute Human Brain Atlas[55]. Maps for each gene were downloaded from the Neurosynth website (https://neurosynth.org/genes/) and then submitted to a one-sample t-test in SPM12, with a threshold of FDR q<0.01.

Data and code availability

Tidy data and analysis code are available at https://github.com/IIT-LAND/ei_hurst. Source code of the recurrent network model is available at https://github.com/pablomc88/EEG_proxy_from_network_point_neurons. Raw RNA-seq data used to identify genes differentially expressed by DHT can be found in Gene Expression Omnibus (GSE86457). Data for the Allen Institute Human Brain Atlas can be found here: https://human.brain-map.org. Mapping of this data to MNI space can be found at the Neurosynth website (https://neurosynth.org/genes/).

Acknowledgments

The Medical Research Council Autism Imaging Multicentre Study Consortium (MRC AIMS Consortium) is a UK collaboration between the Institute of Psychiatry, Psychology & Neuroscience (IoPPN) at King's College London, the Autism Research Centre, University of Cambridge and the Autism Research Group, University of Oxford. The Consortium members are in alphabetical order: Anthony J Bailey (Oxford), Simon Baron-Cohen (Cambridge), Patrick F Bolton (IoPPN), Edward T Bullmore (Cambridge), Sarah Carrington (Oxford), Marco Catani (IoPPN), Bhismadev Chakrabarti (Cambridge), Michael C Craig (IoPPN), Eileen M Daly (IoPPN), Sean CL Deoni (IoPPN), Christine Ecker (IoPPN), Francesca Happé (IoPPN), Julian Henty (Cambridge), Peter Jezzard (Oxford), Patrick Johnston (IoPPN), Derek K Jones (IoPPN), Meng-Chuan Lai (Cambridge), Michael V Lombardo (Cambridge), Anya Madden (IoPPN), Diane Mullins (IoPPN), Clodagh M Murphy (IoPPN), Declan GM Murphy (IoPPN), Greg Pasco (Cambridge), Amber NV Ruigrok (Cambridge), Susan A Sadek (Cambridge), Debbie Spain (IoPPN), Rose Stewart (Oxford), John Suckling (Cambridge), Sally J Wheelwright (Cambridge) and Steven C Williams (IoPPN).

Funding

The authors disclosed receipt of the following financial support for the research, authorship and/or publication of this article: The project was supported by the UK Medical Research Council (grant number: GO 400061) and European Autism Interventions – a Multicentre Study for Developing New Medications (EU-AIMS); EU-AIMS has received support from the Innovative Medicines Initiative Joint Undertaking under grant agreement no. 115300, resources of which are composed of financial contribution from the European Union's Seventh Framework Programme (FP7/2007-2013) and EFPIA companies' in-kind contribution. During the period of this work, M.-C.L. was supported by the Ontario Brain Institute via the Province of Ontario Neurodevelopmental Disorders Network (IDS-I l-02), the Slifka-Ritvo Award for Innovation in Autism Research from the International Society for Autism Research and the Alan B. Slifka Foundation, the Academic Scholars Award from the Department of Psychiatry, University of Toronto, the O'Brien Scholars Program in the Child and Youth Mental Health Collaborative at the Centre for Addiction and Mental Health (CAMH) and The Hospital for Sick Children, the Slaight Family Child and Youth Mental Health Innovation Fund from CAMH Foundation, and the Canadian Institutes of Health Research; M.V.L. was supported by a European Research Council (ERC) Starting Grant (ERC-2017-STG; AUTISMS; no. 755816); SP was funded by a SFARI explorer grant (Grant no. 602849), by the NIH Brain Initiative (Grants No. R01 NS108410 and No. U19 NS107464), and by the CARITRO Foundation; A. G. was supported by a European Research Council (ERC) Starting Grant (ERC-2018-STG; DISCONN; no. 802371), the Brain and Behavior Research Foundation (NARSAD; Independent Investigator Grant; no. 25861), the Simons Foundation (SFARI 400101), the NIH (1R21MH116473-01A1) and by Telethon foundation; S. B.-C. was funded by the Autism Research Trust, the Wellcome Trust, the Templeton World Charitable Foundation, and the NIHR Biomedical Research Centre in Cambridge, during the period of this work. S. B.-C. also received funding from the Innovative Medicines Initiative 2 Joint Undertaking (JU) under grant agreement No 777394. The JU receives support from the European Union's Horizon 2020 research and innovation programme and EFPIA and AUTISM SPEAKS, Autistica, SFARI. S. B.-C. is also supported by the National Institute for Health Research (NIHR) Collaboration for Leadership in Applied Health Research and Care East of England at Cambridgeshire and Peterborough NHS Foundation Trust. The views expressed are

those of the author(s) and not necessarily those of the NHS, NIHR or Department of Health and Social Care.

Declaration of Interests

E.T.B. is employed half-time by the University of Cambridge and half-time at GlaxoSmithKline plc (GSK); he holds stock in GSK. All other authors have no conflict of interests to declare.

References

1. Rubenstein, J. L. R. & Merzenich, M. M. Model of autism: increased ratio of excitation/inhibition in key neural systems. *Genes Brain Behav.* **2**, 255–267 (2003).
2. Sohal, V. S. & Rubenstein, J. L. R. Excitation-inhibition balance as a framework for investigating mechanisms in neuropsychiatric disorders. *Mol. Psychiatry* **24**, 1248–1257 (2019).
3. Nelson, S. B. & Valakh, V. Excitatory/Inhibitory Balance and Circuit Homeostasis in Autism Spectrum Disorders. *Neuron* **87**, 684–698 (2015).
4. Happé, F., Ronald, A. & Plomin, R. Time to give up on a single explanation for autism. *Nat. Neurosci.* **9**, 1218–1220 (2006).
5. Lombardo, M. V., Lai, M.-C. & Baron-Cohen, S. Big data approaches to decomposing heterogeneity across the autism spectrum. *Mol. Psychiatry* **24**, 1435–1450 (2019).
6. Lombardo, M. V. *et al.* Different functional neural substrates for good and poor language outcome in autism. *Neuron* **86**, 567–577 (2015).
7. Lombardo, M. V. *et al.* Large-scale associations between the leukocyte transcriptome and BOLD responses to speech differ in autism early language outcome subtypes. *Nat. Neurosci.* **21**, 1680–1688 (2018).
8. Lombardo, M. V. *et al.* Default mode-visual network hypoconnectivity in an autism subtype with pronounced social visual engagement difficulties. *Elife* **8**, (2019).
9. Lai, M.-C., Lombardo, M. V., Auyeung, B., Chakrabarti, B. & Baron-Cohen, S. Sex/gender differences and autism: setting the scene for future research. *J Am Acad Child Adolesc Psychiatry* **54**, 11–24 (2015).
10. Lai, M.-C. *et al.* Imaging sex/gender and autism in the brain: Etiological implications. *J. Neurosci. Res.* **95**, 380–397 (2017).
11. Lee, E., Lee, J. & Kim, E. Excitation/Inhibition Imbalance in Animal Models of Autism Spectrum Disorders. *Biol. Psychiatry* **81**, 838–847 (2017).
12. Bozzi, Y., Provenzano, G. & Casarosa, S. Neurobiological bases of autism-epilepsy comorbidity: a focus on excitation/inhibition imbalance. *Eur. J. Neurosci.* **47**, 534–548 (2018).
13. Lombardo, M. V. *et al.* Sex-specific impact of prenatal androgens on social brain default mode subsystems. *Mol. Psychiatry* (2018) doi:10.1038/s41380-018-0198-y.
14. Yizhar, O. *et al.* Neocortical excitation/inhibition balance in information processing and social dysfunction. *Nature* **477**, 171–178 (2011).
15. Selimbeyoglu, A. *et al.* Modulation of prefrontal cortex excitation/inhibition balance rescues social behavior in CNTNAP2-deficient mice. *Sci Transl Med* **9**, (2017).
16. Lai, M.-C. *et al.* Quantifying and exploring camouflaging in men and women with autism. *Autism* **21**, 690–702 (2017).
17. Hull, L. *et al.* Gender differences in self-reported camouflaging in autistic and non-autistic adults. *Autism* 1362361319864804 (2019) doi:10.1177/1362361319864804.
18. Schuck, R. K., Flores, R. E. & Fung, L. K. Brief Report: Sex/Gender Differences in Symptomology and Camouflaging in Adults with Autism Spectrum Disorder. *J Autism Dev Disord* **49**, 2597–2604 (2019).
19. Lai, M.-C. *et al.* Neural self-representation in autistic women and association with 'compensatory camouflaging'. *Autism* **23**, 1210–1223 (2019).

20. Bullmore, E. *et al.* Colored noise and computational inference in neurophysiological (fMRI) time series analysis: Resampling methods in time and wavelet domains. *Human Brain Mapping* **12**, 61–78 (2001).
21. Maxim, V. *et al.* Fractional Gaussian noise, functional MRI and Alzheimer's disease. *Neuroimage* **25**, 141–158 (2005).
22. He, B. J. Scale-free properties of the functional magnetic resonance imaging signal during rest and task. *J. Neurosci.* **31**, 13786–13795 (2011).
23. Bédard, C., Kröger, H. & Destexhe, A. Does the 1/f frequency scaling of brain signals reflect self-organized critical states? *Phys. Rev. Lett.* **97**, 118102 (2006).
24. He, B. J. Scale-free brain activity: past, present, and future. *Trends Cogn. Sci. (Regul. Ed.)* **18**, 480–487 (2014).
25. Brunel, N. & Wang, X.-J. What Determines the Frequency of Fast Network Oscillations With Irregular Neural Discharges? I. Synaptic Dynamics and Excitation-Inhibition Balance. *Journal of Neurophysiology* **90**, 415–430 (2003).
26. Mazzoni, A., Panzeri, S., Logothetis, N. K. & Brunel, N. Encoding of naturalistic stimuli by local field potential spectra in networks of excitatory and inhibitory neurons. *PLoS Comput. Biol.* **4**, e1000239 (2008).
27. Lombardi, F., Herrmann, H. J. & de Arcangelis, L. Balance of excitation and inhibition determines 1/f power spectrum in neuronal networks. *Chaos* **27**, 047402 (2017).
28. Gao, R., Peterson, E. J. & Voytek, B. Inferring synaptic excitation/inhibition balance from field potentials. *Neuroimage* **158**, 70–78 (2017).
29. Lai, M.-C. *et al.* A shift to randomness of brain oscillations in people with autism. *Biol. Psychiatry* **68**, 1092–1099 (2010).
30. Watanabe, T., Rees, G. & Masuda, N. Atypical intrinsic neural timescale in autism. *eLife* **8**, e42256 (2019).
31. Ferenczi, E. A. *et al.* Prefrontal cortical regulation of brainwide circuit dynamics and reward-related behavior. *Science* **351**, aac9698–aac9698 (2016).
32. Balsters, J. H., Zerbi, V., Sallet, J., Wenderoth, N. & Mars, R. B. Primate homologs of mouse cortico-striatal circuits. *eLife* **9**, e53680 (2020).
33. Stadnitski, T. Measuring fractality. *Front Physiol* **3**, 127 (2012).
34. Mazzoni, A., Whittingstall, K., Brunel, N., Logothetis, N. K. & Panzeri, S. Understanding the relationships between spike rate and delta/gamma frequency bands of LFPs and EEGs using a local cortical network model. *Neuroimage* **52**, 956–972 (2010).
35. Deco, G., Rolls, E. T. & Horwitz, B. 'What' and 'where' in visual working memory: a computational neurodynamical perspective for integrating FMRI and single-neuron data. *J Cogn Neurosci* **16**, 683–701 (2004).
36. Logothetis, N. K. What we can do and what we cannot do with fMRI. *Nature* **453**, 869–878 (2008).
37. Mazzoni, A. *et al.* Computing the Local Field Potential (LFP) from Integrate-and-Fire Network Models. *PLoS Comput. Biol.* **11**, e1004584 (2015).
38. Mazzoni, A., Brunel, N., Cavallari, S., Logothetis, N. K. & Panzeri, S. Cortical dynamics during naturalistic sensory stimulations: experiments and models. *J. Physiol. Paris* **105**, 2–15 (2011).
39. Barbieri, F., Mazzoni, A., Logothetis, N. K., Panzeri, S. & Brunel, N. Stimulus dependence of local field potential spectra: experiment versus theory. *J. Neurosci.* **34**, 14589–14605 (2014).
40. Cavallari, S., Panzeri, S. & Mazzoni, A. Comparison of the dynamics of neural interactions between current-based and conductance-based integrate-and-fire recurrent networks. *Front Neural Circuits* **8**, 12 (2014).
41. Haller, M. *et al. Parameterizing neural power spectra*. http://biorxiv.org/lookup/doi/10.1101/299859 (2018) doi:10.1101/299859.

42. Logothetis, N. K., Pauls, J., Augath, M., Trinath, T. & Oeltermann, A. Neurophysiological investigation of the basis of the fMRI signal. *Nature* **412**, 150–157 (2001).
43. Magri, C., Schridde, U., Murayama, Y., Panzeri, S. & Logothetis, N. K. The amplitude and timing of the BOLD signal reflects the relationship between local field potential power at different frequencies. *J. Neurosci.* **32**, 1395–1407 (2012).
44. Rauch, A., Rainer, G. & Logothetis, N. K. The effect of a serotonin-induced dissociation between spiking and perisynaptic activity on BOLD functional MRI. *Proc. Natl. Acad. Sci. U.S.A.* **105**, 6759–6764 (2008).
45. Viswanathan, A. & Freeman, R. D. Neurometabolic coupling in cerebral cortex reflects synaptic more than spiking activity. *Nat. Neurosci.* **10**, 1308–1312 (2007).
46. Lauritzen, M. & Gold, L. Brain Function and Neurophysiological Correlates of Signals Used in Functional Neuroimaging. *J. Neurosci.* **23**, 3972–3980 (2003).
47. Schölvinck, M. L., Maier, A., Ye, F. Q., Duyn, J. H. & Leopold, D. A. Neural basis of global resting-state fMRI activity. *Proc. Natl. Acad. Sci. U.S.A.* **107**, 10238–10243 (2010).
48. Scheeringa, R. *et al.* Neuronal dynamics underlying high- and low-frequency EEG oscillations contribute independently to the human BOLD signal. *Neuron* **69**, 572–583 (2011).
49. Alexander, G. M. *et al.* Remote control of neuronal activity in transgenic mice expressing evolved G protein-coupled receptors. *Neuron* **63**, 27–39 (2009).
50. Stachniak, T. J., Ghosh, A. & Sternson, S. M. Chemogenetic synaptic silencing of neural circuits localizes a hypothalamus→midbrain pathway for feeding behavior. *Neuron* **82**, 797–808 (2014).
51. Zou, Q.-H. *et al.* An improved approach to detection of amplitude of low-frequency fluctuation (ALFF) for resting-state fMRI: fractional ALFF. *J. Neurosci. Methods* **172**, 137–141 (2008).
52. Satterstrom, F. K. *et al.* Large-Scale Exome Sequencing Study Implicates Both Developmental and Functional Changes in the Neurobiology of Autism. *Cell* (2020) doi:10.1016/j.cell.2019.12.036.
53. Velmeshev, D. *et al.* Single-cell genomics identifies cell type–specific molecular changes in autism. *Science* **364**, 685–689 (2019).
54. Quartier, A. *et al.* Genes and Pathways Regulated by Androgens in Human Neural Cells, Potential Candidates for the Male Excess in Autism Spectrum Disorder. *Biological Psychiatry* **84**, 239–252 (2018).
55. Hawrylycz, M. J. *et al.* An anatomically comprehensive atlas of the adult human brain transcriptome. *Nature* **489**, 391–399 (2012).
56. Courchesne, E. *et al.* The ASD Living Biology: from cell proliferation to clinical phenotype. *Mol. Psychiatry* **24**, 88–107 (2019).
57. Markicevic, M. *et al.* Cortical Excitation:Inhibition Imbalance Causes Abnormal Brain Network Dynamics as Observed in Neurodevelopmental Disorders. *Cerebral Cortex* bhaa084 (2020) doi:10.1093/cercor/bhaa084.
58. Mukamel, R. Coupling Between Neuronal Firing, Field Potentials, and fMRI in Human Auditory Cortex. *Science* **309**, 951–954 (2005).
59. Niessing, J. Hemodynamic Signals Correlate Tightly with Synchronized Gamma Oscillations. *Science* **309**, 948–951 (2005).
60. Scheeringa, R. & Fries, P. Cortical layers, rhythms and BOLD signals. *NeuroImage* **197**, 689–698 (2019).
61. Zucca, S., Pasquale, V., Lagomarsino de Leon Roig, P., Panzeri, S. & Fellin, T. Thalamic Drive of Cortical Parvalbumin-Positive Interneurons during Down States in Anesthetized Mice. *Current Biology* **29**, 1481-1490.e6 (2019).
62. Willsey, A. J. *et al.* Coexpression networks implicate human midfetal deep cortical projection neurons in the pathogenesis of autism. *Cell* **155**, 997–1007 (2013).

63. Parikshak, N. N. *et al.* Integrative functional genomic analyses implicate specific molecular pathways and circuits in autism. *Cell* **155**, 1008–1021 (2013).
64. Di Martino, A. *et al.* Functional brain correlates of social and nonsocial processes in autism spectrum disorders: an activation likelihood estimation meta-analysis. *Biol. Psychiatry* **65**, 63–74 (2009).
65. Di Martino, A. *et al.* The autism brain imaging data exchange: towards a large-scale evaluation of the intrinsic brain architecture in autism. *Mol Psychiatry* **19**, 659–667 (2014).
66. Uddin, L. Q. & Menon, V. The anterior insula in autism: under-connected and under-examined. *Neurosci Biobehav Rev* **33**, 1198–1203 (2009).
67. Padmanabhan, A., Lynch, C. J., Schaer, M. & Menon, V. The Default Mode Network in Autism. *Biol Psychiatry Cogn Neurosci Neuroimaging* **2**, 476–486 (2017).
68. Lombardo, M. V. *et al.* Atypical neural self-representation in autism. *Brain* **133**, 611–624 (2010).
69. Bejerot, S. *et al.* The extreme male brain revisited: gender coherence in adults with autism spectrum disorder. *Br J Psychiatry* **201**, 116–123 (2012).
70. Bethlehem, R. A. I., Seidlitz, J., Romero-Garcia, R., Dumas, G. & Lombardo, M. V. *Normative age modelling of cortical thickness in autistic males*. http://biorxiv.org/lookup/doi/10.1101/252593 (2018) doi:10.1101/252593.
71. Buckner, R. L. & DiNicola, L. M. The brain's default network: updated anatomy, physiology and evolving insights. *Nat. Rev. Neurosci.* **20**, 593–608 (2019).
72. Yeo, B. T. T. *et al.* The organization of the human cerebral cortex estimated by intrinsic functional connectivity. *J. Neurophysiol.* **106**, 1125–1165 (2011).
73. Horder, J. *et al.* GABAA receptor availability is not altered in adults with autism spectrum disorder or in mouse models. *Sci Transl Med* **10**, (2018).
74. Coghlan, S. *et al.* GABA system dysfunction in autism and related disorders: From synapse to symptoms. *Neuroscience & Biobehavioral Reviews* **36**, 2044–2055 (2012).
75. Kaczkurkin, A. N., Raznahan, A. & Satterthwaite, T. D. Sex differences in the developing brain: insights from multimodal neuroimaging. *Neuropsychopharmacology* **44**, 71–85 (2019).
76. Bedford, S. A. *et al.* Large-scale analyses of the relationship between sex, age and intelligence quotient heterogeneity and cortical morphometry in autism spectrum disorder. *Mol. Psychiatry* (2019) doi:10.1038/s41380-019-0420-6.
77. Livingston, L. A., Shah, P. & Happé, F. Compensatory strategies below the behavioural surface in autism: a qualitative study. *Lancet Psychiatry* **6**, 766–777 (2019).
78. Mitchell, J. P., Macrae, C. N. & Banaji, M. R. Dissociable medial prefrontal contributions to judgments of similar and dissimilar others. *Neuron* **50**, 655–663 (2006).
79. Robinson, E. B., Lichtenstein, P., Anckarsäter, H., Happé, F. & Ronald, A. Examining and interpreting the female protective effect against autistic behavior. *Proc. Natl. Acad. Sci. U.S.A.* **110**, 5258–5262 (2013).
80. Werling, D. M. The role of sex-differential biology in risk for autism spectrum disorder. *Biol Sex Differ* **7**, 58 (2016).
81. Rutter, M., Caspi, A. & Moffitt, T. E. Using sex differences in psychopathology to study causal mechanisms: unifying issues and research strategies. *J Child Psychol Psychiatry* **44**, 1092–1115 (2003).
82. Chantiluke, K. *et al.* Inverse fluoxetine effects on inhibitory brain activation in non-comorbid boys with ADHD and with ASD. *Psychopharmacology (Berl.)* **232**, 2071–2082 (2015).
83. Naaijen, J. *et al.* Glutamatergic and GABAergic gene sets in attention-deficit/hyperactivity disorder: association to overlapping traits in ADHD and autism. *Transl Psychiatry* **7**, e999 (2017).

84. Wink, A. M., Bernard, F., Salvador, R., Bullmore, E. & Suckling, J. Age and cholinergic effects on hemodynamics and functional coherence of human hippocampus. *Neurobiol. Aging* **27**, 1395–1404 (2006).
85. Voytek, B. *et al.* Age-Related Changes in 1/f Neural Electrophysiological Noise. *J. Neurosci.* **35**, 13257–13265 (2015).
86. Lord, C., Rutter, M. & Le Couteur, A. Autism Diagnostic Interview-Revised: a revised version of a diagnostic interview for caregivers of individuals with possible pervasive developmental disorders. *J Autism Dev Disord* **24**, 659–685 (1994).
87. Pilling, S., Baron-Cohen, S., Megnin-Viggars, O., Lee, R. & Taylor, C. Recognition, referral, diagnosis, and management of adults with autism: summary of NICE guidance. *BMJ* **344**, (2012).
88. Baron-Cohen, S., Wheelwright, S., Skinner, R., Martin, J. & Clubley, E. The autism-spectrum quotient (AQ): evidence from Asperger syndrome/high-functioning autism, males and females, scientists and mathematicians. *J Autism Dev Disord* **31**, 5–17 (2001).
89. Lord, C. *et al.* The autism diagnostic observation schedule-generic: a standard measure of social and communication deficits associated with the spectrum of autism. *J Autism Dev Disord* **30**, 205–223 (2000).
90. Baron-Cohen, S., Wheelwright, S., Hill, J., Raste, Y. & Plumb, I. The 'Reading the Mind in the Eyes' Test revised version: a study with normal adults, and adults with Asperger syndrome or high-functioning autism. *J Child Psychol Psychiatry* **42**, 241–251 (2001).
91. Power, J. D., Barnes, K. A., Snyder, A. Z., Schlaggar, B. L. & Petersen, S. E. Spurious but systematic correlations in functional connectivity MRI networks arise from subject motion. *Neuroimage* **59**, 2142–2154 (2012).
92. Cox, R. W. AFNI: software for analysis and visualization of functional magnetic resonance neuroimages. *Comput. Biomed. Res.* **29**, 162–173 (1996).
93. Kundu, P., Inati, S. J., Evans, J. W., Luh, W.-M. & Bandettini, P. A. Differentiating BOLD and non-BOLD signals in fMRI time series using multi-echo EPI. *Neuroimage* **60**, 1759–1770 (2012).
94. Patel, A. X. *et al.* A wavelet method for modeling and despiking motion artifacts from resting-state fMRI time series. *Neuroimage* **95**, 287–304 (2014).
95. Glasser, M. F. *et al.* A multi-modal parcellation of human cerebral cortex. *Nature* **536**, 171–178 (2016).
96. Krishnan, A., Williams, L. J., McIntosh, A. R. & Abdi, H. Partial Least Squares (PLS) methods for neuroimaging: a tutorial and review. *Neuroimage* **56**, 455–475 (2011).
97. Bargiela, S., Steward, R. & Mandy, W. The Experiences of Late-diagnosed Women with Autism Spectrum Conditions: An Investigation of the Female Autism Phenotype. *J Autism Dev Disord* **46**, 3281–3294 (2016).
98. Hull, L. *et al.* 'Putting on My Best Normal': Social Camouflaging in Adults with Autism Spectrum Conditions. *J Autism Dev Disord* **47**, 2519–2534 (2017).
99. Bertero, A. *et al.* Autism-associated 16p11.2 microdeletion impairs prefrontal functional connectivity in mouse and human. *Brain* **141**, 2055–2065 (2018).
100. Gozzi, A. *et al.* A multimodality investigation of cerebral hemodynamics and autoregulation in pharmacological MRI. *Magnetic Resonance Imaging* **25**, 826–833 (2007).
101. Gutierrez-Barragan, D., Basson, M. A., Panzeri, S. & Gozzi, A. Infraslow State Fluctuations Govern Spontaneous fMRI Network Dynamics. *Curr. Biol.* **29**, 2295-2306.e5 (2019).
102. Liska, A., Galbusera, A., Schwarz, A. J. & Gozzi, A. Functional connectivity hubs of the mouse brain. *Neuroimage* **115**, 281–291 (2015).
103. Scheeringa, R. *et al.* Trial-by-trial coupling between EEG and BOLD identifies networks related to alpha and theta EEG power increases during working memory maintenance. *Neuroimage* **44**, 1224–1238 (2009).

104. Whittingstall, K. & Logothetis, N. K. Frequency-band coupling in surface EEG reflects spiking activity in monkey visual cortex. *Neuron* **64**, 281–289 (2009).
105. Goense, J. B. M. & Logothetis, N. K. Neurophysiology of the BOLD fMRI signal in awake monkeys. *Curr. Biol.* **18**, 631–640 (2008).
106. Kilner, J. M., Mattout, J., Henson, R. & Friston, K. J. Hemodynamic correlates of EEG: a heuristic. *Neuroimage* **28**, 280–286 (2005).
107. Wijeakumar, S., Ambrose, J. P., Spencer, J. P. & Curtu, R. Model-based functional neuroimaging using dynamic neural fields: An integrative cognitive neuroscience approach. *J Math Psychol* **76**, 212–235 (2017).
108. Buss, A. T., Wifall, T., Hazeltine, E. & Spencer, J. P. Integrating the behavioral and neural dynamics of response selection in a dual-task paradigm: a dynamic neural field model of Dux et al. (2009). *J Cogn Neurosci* **26**, 334–351 (2014).
109. Alcauter, S. *et al.* Frequency of spontaneous BOLD signal shifts during infancy and correlates with cognitive performance. *Dev Cogn Neurosci* **12**, 40–50 (2015).
110. Allen, E. A. *et al.* A baseline for the multivariate comparison of resting-state networks. *Front Syst Neurosci* **5**, 2 (2011).

Tables

	Time	Condition (DREADD - SHAM)	Time x Condition
Baseline	*0.82 (0.372)*	*0.81 (0.369)*	*0.36 (0.549)*
Transition	*5.65 (0.017)**	*3.25 (0.081)*	4.94 (0.026)*
Treatment	*0.61 (0.433)*	*12.92 (0.001)***	*0.66 (0.418)*

Table 1: Results from DREADD excitation manipulation. *F-statistics (p-values in parentheses) for main effects of time, condition, and time*condition interaction for each of the 3 phases of the experiment (Baseline, Transition, Treatment). * = p<0.05, ** = p<0.001.*

	Time	Condition (DREADD - SHAM)	Time x Condition
Baseline	*0.02 (0.876)*	*4.01 (0.054)*	*1.02 (0.137)*
Transition	*0.04* (0.838)	*0.35 (0.561)*	1.36 (0.243)
Treatment	*0.40 (0.533)*	*0.20* (0.673)	*0.10 (0.786)*

Table 2: Results from DREADD silencing manipulation. *F-statistics (p-values in parentheses) for main effects of time, condition, and time*condition interaction for each of the 3 phases of the experiment (Baseline, Transition, Treatment). * = p<0.05, ** = p<0.001.*

	TD males (N=29)	Autistic males (N=23)	TD females (N=33)	Autistic females (N = 25)	Sex	Diagnosis	Sex* Diagnosis
Age	28.00 (6.42)	27.13 (7.14)	26.99 (5.34)	27.35 (6.79)	0.14 (0.70)	0.03 (0.85)	0.25 (0.61)
VIQ	110.62 (11.53)	114.70 (13.04)	120.30 (10.06)	114.08 (12.79)	5.33 (0.02)	0.38 (0.53)	5.18 (0.02)
PIQ	120.00 (10.21)	114.57 (15.70)	117.39 (9.27)	110.88 (17.43)	1.49 (0.22)	5.55 (0.02)	0.04 (0.83)
FIQ	116.97 (10.69)	116.39 (14.15)	121.45 (8.33)	114.16 (13.82)	0.48 (0.48)	3.38 (0.06)	2.24 (0.13)
Camouflaging Score	-	-0.16 (0.38)	-	0.15 (0.34)	9.06 (0.004)	-	-
AQ	15.28 (6.99)	32.70(8.47)	11.97 (4.93)	38.44 (6.34)	0.26 (0.61)	300.59 (2.2e-16)	12.48 (0.0006)
ADI-R Reciprocal-Social-Interaction	-	17.26 (4.77)	-	16.56 (4.52)	0.27 (0.60)	-	-
ADI-R Communication	-	14.83 (3.50)	-	13.40 (3.96)	1.73 (0.19)	-	-
ADI-R RRB	-	5.17 (2.35)	-	4.24 (1.61)	2.61 (0.11)	-	-
ADOS Communication	-	3.30 (1.74)	-	1.24 (1.30)	21.85 (2.59e-5)	-	-
ADOS Social	-	5.48 (3.45)	-	3.48 (3.06)	4.52 (0.03)	-	-

ADOS RRB	-	1.09 (1.12)	-	4.30 (1.61)	61.84 (6.32e-10)	-	-
ADOS Communication + Social Total	-	8.83 (4.87)	-	4.72 (4.09)	10.07 (0.002)	-	-
RMET	27.14 (3.59)	20.83 (6.87)	28.91(2.35)	22.84 (6.40)	3.93 (0.04)	42.30 (2.704e-9)	0.01 (0.89)
Mean FD	0.17 (0.05)	0.20 (0.07)	0.18(0.06)	0.04 (0.17)	0.51 (0.47)	1.77 (0.18)	1.10 (0.29)

*Table 3. Descriptive and inferential statistics for group comparisons of demographic and clinical variables. Values in the columns for each group represent the mean and standard deviation (in parentheses). Values in the columns labeled Sex, Diagnosis, and Sex*Diagnosis indicate the F-statistic and p-value (in parentheses). Abbreviations: TD, Typically Developing; VIQ, verbal IQ; PIQ, performance IQ; FIQ, full-scale IQ ADI-R, Autism Diagnostic Interview–Revised; ADOS, Autism Diagnostic Observation Schedule; RRB, Restricted Repetitive Behaviors; AQ, Autism Spectrum Quotient; RMET, Reading the Mind in the Eyes Test, FD: frame-wise displacement.*

A: Neuron model			
Parameter	Description	Excitatory cells	Inhibitory cells
V_{leak} (mV)	Leak membrane potential	-70	-70
$V_{threshold}$ (mV)	Spike threshold	-52	-52
V_{reset} (mV)	Reset potential	-59	-59
$\tau_{refractory}$ (ms)	Absolute refractory period	2	1
g_{leak} (nS)	Leak membrane conductance	25	20
C_m (pF)	Membrane capacitance	500	200
τ_m (ms)	Membrane time constant	20	10
B: Connection parameters			
Parameter	Description	Excitatory cells	Inhibitory cells
E_{AMPA} (mV)	AMPA reversal potential	0	0
E_{GABA} (mV)	GABA reversal potential	-80	-80
$\tau_{r(AMPA)}$ (ms)	Conductance rise time (AMPA)	0.4	0.2
$\tau_{d(AMPA)}$ (ms)	Conductance decay time (AMPA)	2	1
$\tau_{r(GABA)}$ (ms)	Conductance rise time (GABA)	0.25	0.25
$\tau_{d(GABA)}$ (ms)	Conductance decay time (GABA)	5	5
τ_l (ms)	Synapse latency	0	0
$g_{AMPA(rec.)}$ (nS)	AMPA conductance (recurrent)	0.178	0.233
$g_{AMPA(tha.)}$ (nS)	AMPA conductance (thalamic)	0.234	0.317
$g_{AMPA(cort.)}$ (nS)	AMPA conductance (intracortical)	0.187	0.254
g_{GABA} (nS)	GABA conductance	2.01	2.7

Table 4: Baseline reference parameters of the recurrent network model. Parameters used in Cavallari et al.,[40] with conductance-based synapses.